UiT The Arctic University of Norway

Faculty of Science and Technology
Department of Physics and Technology

Iceberg Detection for Arctic Operations

A Comparison of C- and L-band Wide-Swath SAR

Laust Færch

A dissertation for the degree of Philosophiae Doctor (PhD)

June 2024

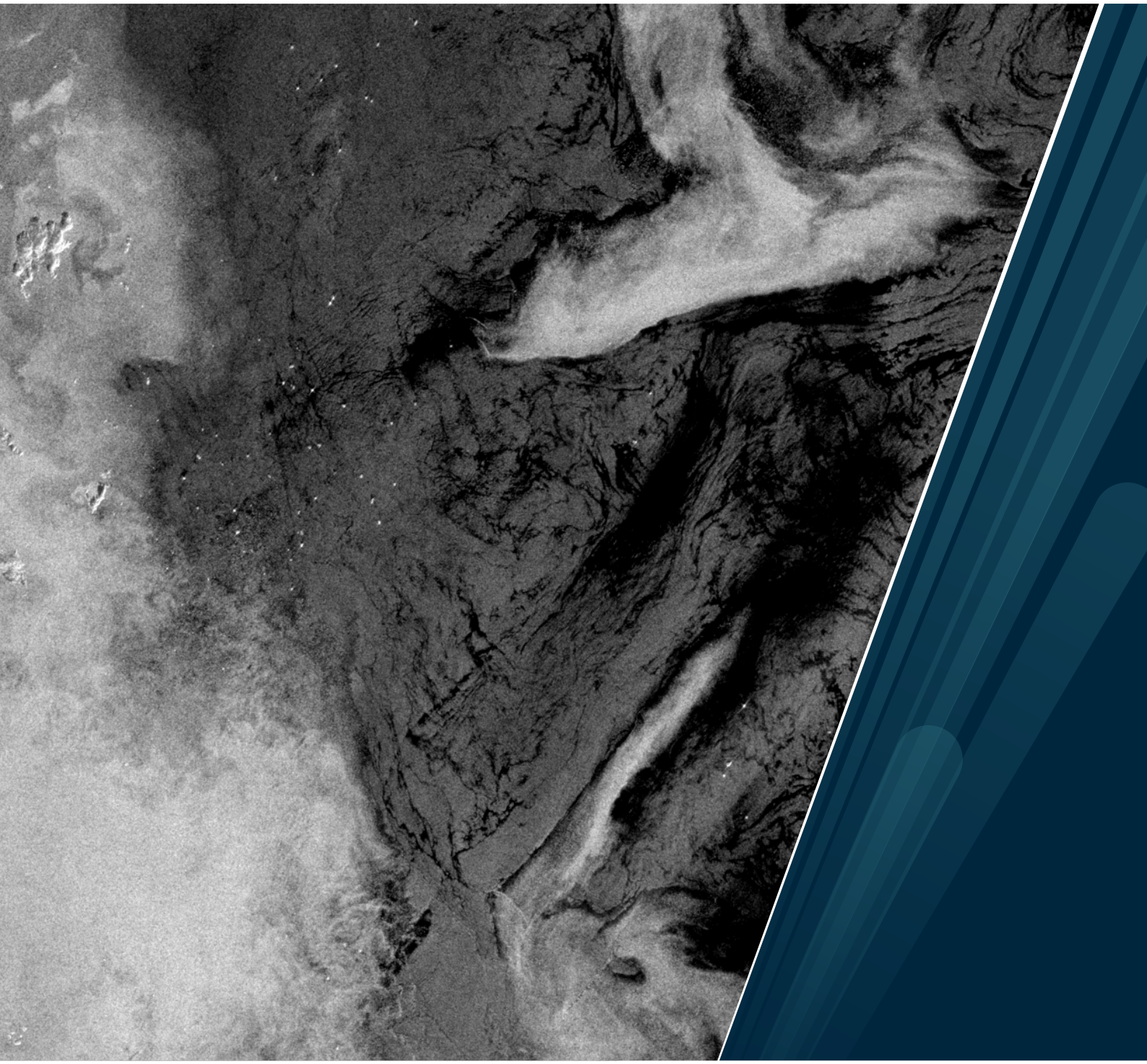

Title	**Iceberg Detection for Arctic Operations** A Comparison of C- and L-band Wide-Swath SAR
Author	**Laust Færch**
Type	A dissertation for the degree of Philosophiae Doctor (PhD)
Month and Year	June 2024
Supervisors	**Wolfgang Dierking**, Adjunct Professor at the Earth Observation Group, UiT **Anthony P. Doulgeris**, Group Leader at the Earth Observation Group, UiT **Nick Hughes**, Leader of the Norwegian Ice Service, MET Norway
University	UiT - The Arctic University of Norway Faculty of Science and Technology Department of Physics and Technology Earth Observation Group Centre for Integrated Remote Sensing and Forecasting for Arctic Operations (CIRFA)
Funding	The research is funded by CIRFA partners and the Research Council of Norway (RCN grant no. 237906)
Pages	119
ISBN:	000-00-0000-000-0
Cover Image	JAXA

Non scholae sed vitae

Abstract

The accurate detection and mapping of icebergs in the Arctic is important for the safety of maritime traffic and offshore infrastructure and for monitoring the health of marine-terminating glaciers.

Synthetic aperture radar (SAR) images from satellites have proven to be a useful tool for Arctic monitoring, and C-band SAR images are currently used for operational iceberg monitoring in selected areas. However, current C-band data have been shown to offer only limited discrimination between icebergs and sea ice, impeding regular detection of icebergs in sea ice. Moreover, the methods currently used for iceberg detection in open water are poorly validated, and additional knowledge about their performance is needed. Future L-band missions are expected to increase detection accuracies for icebergs in sea ice and may, in addition, offer some advantages over C-band for detecting icebergs in open water.

In this thesis, we are comparing the use of C- and L-band SAR images for the detection of icebergs in the Arctic. The first part of this thesis provides a background and introduction to Arctic icebergs, SAR, and the topic of iceberg detection using SAR. The second part of this thesis presents three research papers that have been produced as part of this Ph.D. project.

The results of the research show that although L-band SAR serves as an excellent complement to C-band SAR for the detection of icebergs in open water, the true advantage of L-band over C-band is for the detection of icebergs in sea ice. This opens up a whole new area for monitoring, allowing for a more complete mapping of icebergs, and greatly improving the possibilities of Arctic-wide iceberg surveillance.

Acknowledgements

First and foremost, I would like to thank my scientific supervisor, Wolfgang Dierking. Thank you for taking the time to help improve my drafts and manuscripts through many discussions, and thank you for helping me to keep a focus on the most important things. Our discussions helped to improve the published outcome of my Ph.D. project considerably. Secondly, I must extend my thanks to my two other supervisors, Anthony P. Doulgeris and Nick Hughes. Your comments and suggestions, especially at the beginning of the project, have greatly helped to shape the project and keep it on the right track. I would also like to extend my thanks to all my great colleagues at CIRFA and the EO Group. The EO group has been a wonderfully relaxed, yet productive, work environment, and I have learned a great deal from many of you during these years and shared many memorable moments.

A special thank you to Jelte van Oostveen. Your wisdom offered through countless conversations at NORCE, have helped me greatly in focusing on the right things at the right time, and not getting lost in needless and irrelevant tasks that are encountered during a typical Ph.D. project.

The work presented in this thesis has been funded by the Center for Integrated Remote Sensing and Forecasting for Arctic Operations (CIRFA). I would like to acknowledge the center leader, Torbjørn Eltoft, for the opportunity to carry out the research in this thesis. Also, thank you for the opportunity to participate in two fieldwork cruises going into the sea ice, which were some of the most memorable experiences during this Ph.D.

Finally, my heartleft gratitude goes out to my partner, Anna. In the summer of 2020, you supported me in the crazy idea of applying to a Ph.D. position in Northern Norway and later followed me to Tromsø while you were pregnant with our son, Nils. I am forever thankful for having spent my time in the Arctic with you.

Contents

List of Figures

List of Tables

List of Abbreviations

CCD Charge-coupled device

CFAR Constant false alarm rate

CNN Convolutional neural network

DMI Danish Meteorological Institute

EM Expectation-maximization

EW Extra wide-swath

FN False negative

FP False positive

FYI First-year ice

IA Incidence angle

IIP International Ice Patrol

IW Interferometric wide-swath

MYI Multi-year ice

NIR Near-infrared

NIS Normalized intensity sum

PDF Probability density function

PFA Probability of false alarm

PRF Pulse-repetition frequency

PUT Pixel under test

RFI Radio-frequency interference

SAR Synthetic aperture radar

SNR Signal-to-noise ratio

TP True positive

WMO World Meteorological Organization

1 Introduction

1.1 Background

Icebergs pose a considerable danger to ships, and although collisions between ships and icebergs are rare, the risk ought not to be completely disregarded. Small pieces of ice breaking off larger bergs, such as bergy bits extending less than one meter above the sea surface, can be very difficult to identify among sea ice and ocean waves and yet pose a significant risk to ships [1]. Furthermore, the consequences of a collision can be serious, as the vast and remote areas in the polar regions can make rescue efforts very time-consuming. In addition to the risk posed to ships, offshore structures such as oil platforms are also at risk of iceberg collision, and in shallow waters iceberg scouring can destroy subsea cables and pipelines. The risk of icebergs is especially significant in the Arctic which, with its four million inhabitants, is the only of the two poles with a substantial human presence [2].

Icebergs also greatly impact the oceanography and biology of their local environment. As icebergs melt, they release cold freshwater into the ocean, which impacts the local circulation [3]. This, in turn, influences the salinity and temperature of the ocean, which can lead to an increase in sea ice formation and alter ocean currents [4]. Changes in local ocean circulation can also trigger the mixing of different ocean layers and lead to the swirling of seabed sediments, providing nutrients and promoting phytoplankton growth [3]. Further, icebergs can also contain nutrients and minerals from land which are released into the ocean as they melt, altering local ecosystems.

In the Arctic, Greenland constitutes the main source of icebergs. From the Greenland ice sheet, it is estimated that up to 500 Gt of solid ice is discharged each year [5]. In addition, between 40-55 Gt of ice are lost yearly from marine-terminating glaciers elsewhere in the Arctic due to a combination of calving and melting [6]. This loss is mainly concentrated in the Russian Arctic and

Svalbard, along with sizeable contributions from glaciers in Alaska (see Figure 1.1). It is difficult to determine exactly how much of this ice drifts out into open water. Some observations suggest that up to half of the solid ice discharge will melt locally [7], however, this still leaves a significant number of icebergs floating in the open ocean in the Arctic.

The discharge of ice in the Arctic might increase in the future. Surface temperatures are increasing due to global warming, and in the Arctic the increase is more than double the global average [8]. Calving rates in both Greenland and Svalbard have been linked to water temperatures [8], and in recent years an acceleration of ice discharge across all of Greenland has been observed [9, 10], which could be caused by the intrusion of warmer Atlantic water [11].

The warming Arctic will also have a big impact on sea ice conditions. Arctic sea ice cover is declining rapidly [12, 13]. On average, the summer (minimum) sea ice extent has decreased by 12.8% per decade [8]. It is predicted that this rapid loss of Arctic sea ice cover will lead to an increase in maritime traffic, as pathways across the Arctic offer a shorter distance between Northern Europe, Asia, and Canada [14]. In recent years, the total tonnage of cargo transported along the Northeast passage has increased considerably, in part facilitated by declining sea ice cover [15]. Some studies have suggested that the Northwest and Transpolar passages will be navigable during the summer months by 2050 [16].

An increase in maritime traffic in the Arctic, along with the possibility of increased iceberg calving due to a warmer climate, will lead to denser ship traffic along maritime routes with high iceberg risk (see Figure 1.1). Furthermore, an increase in calving rates and a decrease in sea ice concentrations could lead to changes in iceberg occurrences, as a compact sea ice cover tends to limit iceberg drift [20].

The Arctic region is geographically huge. The main areas of iceberg risk the Kara Sea, Barents Sea, Greenland Sea, Baffin Bay, and the Labrador Sea cover a combined area of approximately five million square kilometers, making the accurate and timely monitoring of icebergs an extremely challenging task. Modeling of iceberg occurrences has been suggested as a tool for estimating iceberg frequencies in the Arctic. However, problems in accurately estimating the calving rates and seasonal variations in calving constitute a major uncertainty in modeling studies [21, 22]. In addition, the lack of wide-scale iceberg drift observations makes validation of these models difficult [20]. Historically, some attempts have been made to gather iceberg observations on a large scale. The Russian Arctic and Antarctic Research Institute (AARI) collected iceberg observations from reconnaissance flights from 1933 to 1990 over the Barents Sea [23], and the International Ice Patrol (IIP) has been conducting iceberg patrols

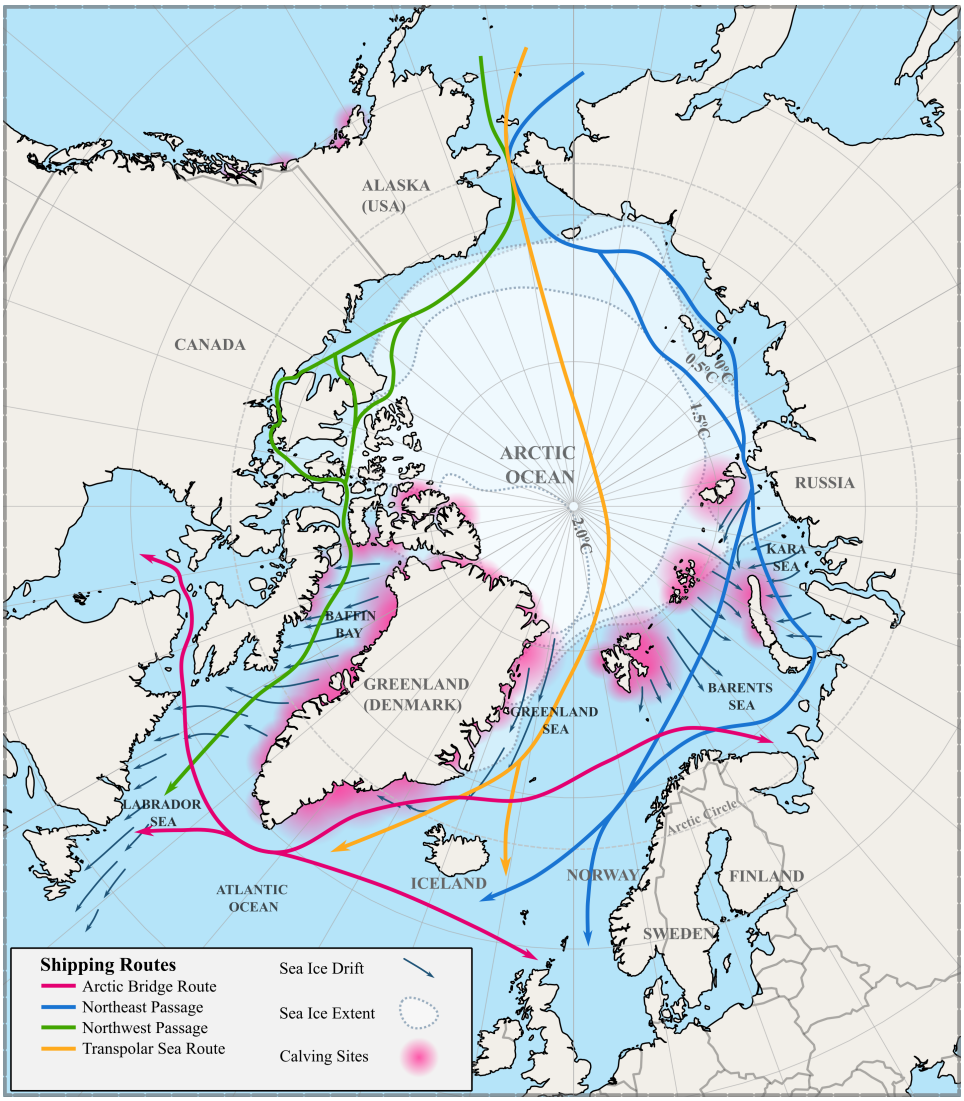

Figure 1.1: Overview of the Arctic, including possible future Arctic shipping lanes [17, 14, 16], iceberg calving sites [6], average sea ice drift directions [18], and predicted September sea ice extent under various climate scenarios [19].

on the Grand Banks of Newfoundland using ships since 1919 [24], and using airplanes since 1946. However, using ships and airplanes can be logistically challenging considering the size of the areas, and are also restricted by local weather conditions. Therefore, in 2011 IIP started using satellite images for operational iceberg monitoring.

Satellite images can offer regular and expansive coverage of the surface of the earth. However, when using satellite images for Arctic monitoring, one

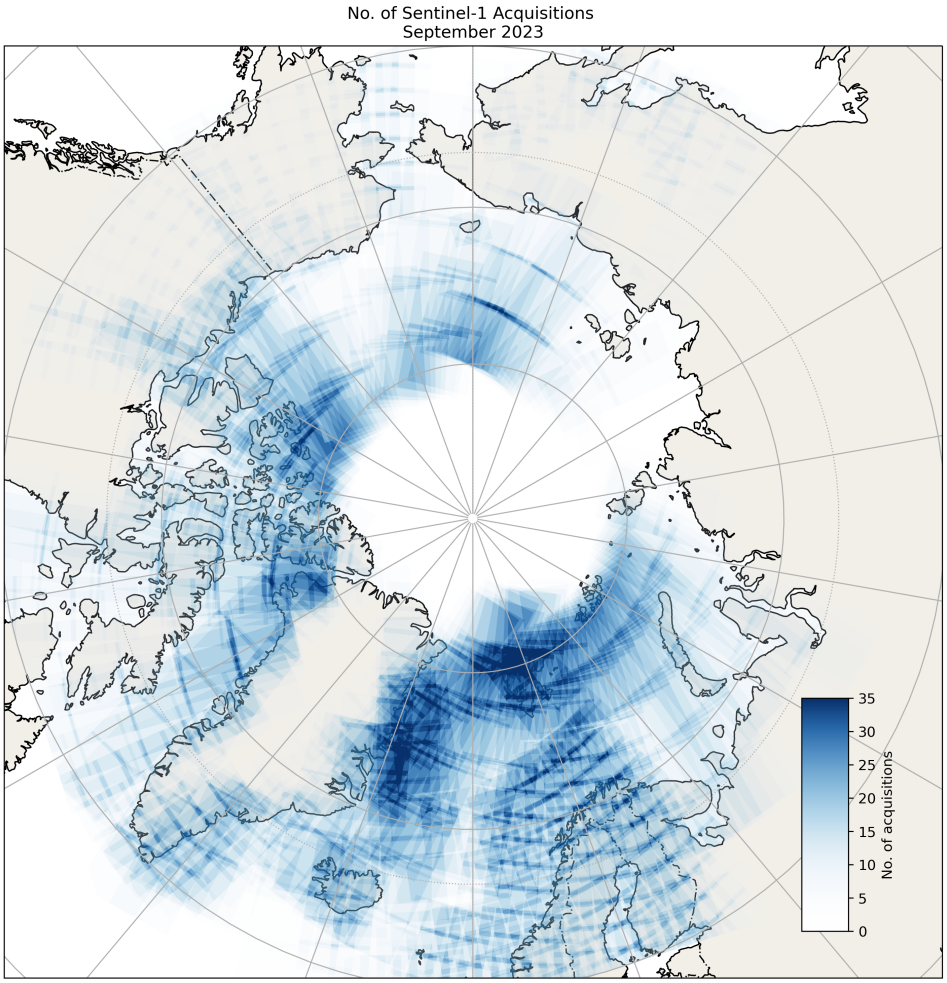

Figure 1.2: Number of acquisitions by Sentinel-1 over the Arctic during September 2023. All images acquired above 60° latitude are included.

needs to consider the fact that optical satellite images are severely restricted by cloud cover and sunlight conditions. However, radar sensors such as Synthetic aperture radar (SAR) can penetrate cloud cover and acquire images without the need for sunlight. C-band SAR sensors, such as the Canadian RADARSAT missions, or the European ERS, Envisat, and Sentinel-1 missions, have been gathering regular SAR scenes since the 1990s through monitoring programs that will likely continue in the coming decade [25, 26]. Earth observation satellites are often placed in a sun-synchronous, near-polar orbit to cover the entire globe, and therefore tend to have a high revisit frequency for the Arctic. Currently, the Sentinel-1 mission offers daily images for large parts of the Arctic, available for free through the Copernicus Program (see Figure 1.2). Combined with other satellite sensors, a very large dataset consisting of decades of SAR

images and covering the entire Arctic, is currently available. This dataset could offer valuable insights into iceberg occurrences and their distribution.

C-band SAR sensors are currently used operationally for iceberg monitoring in the Grand Banks by the IIP, and for Greenland by the Danish Meteorological Institute (DMI), and while these datasets offer a lot of value, specifically for marine traffic and offshore operations, several limitations with the iceberg detection process remain. Firstly, although both agencies use automatic iceberg detection algorithms to detect icebergs in satellite images initially, the final output relies on human quality control. Here, experts are responsible for evaluating detections, by removing likely false detections and adding likely missed detections based on complementary information. Secondly, due to the limited number of in-situ observations of icebergs, the methods are poorly validated and information about their quality is very limited [27, 28]. Lastly, both agencies only consider icebergs in open water and mask out areas covered by sea ice. This is because in SAR images, sea ice, like icebergs, exhibit strong backscatter returns, making it difficult to distinguish sea ice from icebergs.

1.2 Motivation

Large-scale iceberg monitoring using satellite images can help us understand several important elements associated with icebergs. Firstly, operational detection of icebergs would help reduce risks associated with maritime navigation in areas with icebergs. In addition, regular iceberg monitoring coupled with drift and deterioration models could help mitigate risks for companies operating in the Arctic, e.g., by predicting if an iceberg is headed toward important infrastructure. Secondly, long-term statistics of iceberg occurrences based on satellite observations could be used to determine areas in which the risk associated with icebergs is greatest, which would be valuable when planning infrastructure projects and shipping routes. Furthermore, a long time series of iceberg observations covering the entire Arctic could improve our understanding of the interaction between ice sheets and the ocean, e.g., by observing variations in calving rates. Long-term observations could also be used to calibrate numerical models of iceberg occurrences, which in turn could be used to fill gaps in satellite monitoring.

Current archives of C-band satellite SAR imagery offer a valuable dataset for Arctic-wide monitoring of icebergs in open water. However, since the current iceberg detection products from DMI and IIP rely on expert quality control, it is difficult to apply their methods to these archives directly due to the significant amount of work-hours needed. This severely limits historical iceberg detection for regions outside the domain of DMI and IIP, e.g., the Barents Sea. Operational

observations of icebergs in sea ice will also likely require new data sources, as previous studies have suggested that using C-band SAR for the detection of icebergs in sea ice is unreliable. Nevertheless, the mapping of icebergs in sea ice is important for navigators operating in sea ice [29], for ships navigating in or close to the sea ice, as an early warning for icebergs that could later drift into the open ocean, and to obtain a fuller picture of the number of icebergs calved from marine-terminating glaciers.

Luckily, a new generation of L-band SAR sensors might improve detection accuracies for icebergs in sea ice. L-band offers a longer wavelength than C-band and thus increases the penetration depth into snow and ice, which is expected to make the separation between sea ice and icebergs easier. In addition, L-band is less affected by small-scale surface roughness from ocean waves, which could be advantageous for detecting icebergs in wind-roughened open water. In particular, a new L-band ESA mission called ROSE-L, will through the Copernicus program, likely offer similar data coverage of the Arctic as Sentinel-1 (see Figure 1.2). However, at the onset of the work described in this thesis, only a few studies investigating L-band for iceberg detection in the Arctic existed, and there was a complete lack of studies comparing the performance of L- and C-band for detecting icebergs.

If large-scale monitoring of icebergs in the Arctic is to be carried out, the following are needed: 1) A comparison of iceberg detection algorithms against independent validation data. This would primarily be used to assess the performance of various methods which would in turn increase confidence in the results and help integrate the methods into fully automated workflows; 2) The development of methods for detecting icebergs in sea ice. Here, it could be especially valuable to determine whether new data sources (such as L-band) or methods are needed to obtain robust results. This, again, underlines the need for independently obtained validation data to evaluate the performance.

1.3 Scientific Objectives

The purpose of this thesis is to investigate and compare C- and L-band SAR for iceberg detection in the Arctic. Due to the lack of validation data utilized by previous studies (see Chapter 4.4), and the heterogeneous appearance of icebergs and their surroundings in SAR images (see Chapter 4), emphasis will be placed on obtaining and utilizing large datasets of independently obtained iceberg observations for validation. The thesis will focus on icebergs in both open water and sea ice. In addition, it will investigate whether the use of L-band data might improve detection when compared to the more widely used C-band data.

As such, the main objectives of this thesis can be summarized as:

- To explore how the use of L-band SAR data can complement current C-band data for the detection of icebergs in open water.
- To determine whether L-band SAR data can improve the detection of icebergs in sea ice compared to C-band data.
- To evaluate the performance of iceberg detection algorithms applied to SAR images using independent iceberg observations.

A comparison of C- and L-band SAR would help us determine how L-band could be integrated into existing monitoring workflows, i.e., what data to use for different areas or situations. In particular, investigations into the use of L-band SAR for detecting icebergs in sea ice could be a first step towards more complete monitoring in the Arctic. Evaluating detection performance using large datasets of independent iceberg observations will also help to build confidence in existing methods and, in addition, enable us to extract valuable information about their performance relative to various factors such as iceberg sizes or SAR incidence angles.

Since the overarching goal of the work presented in this thesis is to investigate methods that can be used in an operational setting, the thesis will be limited to data typically used for operational monitoring in the Arctic, i.e., dual-polarization HH and HV intensity data acquired in wide-swath mode.

1.4 Thesis Outline

The thesis is organized as follows. Chapter 2 presents some background information on icebergs and sea ice, with a focus on the aspects that are important for iceberg detection using SAR. In Chapter 3, major considerations for remote sensing will be introduced, with a focus on SAR, and specifically those aspects of SAR image acquisition that might influence the detection of icebergs. Chapter 4 then introduces important concepts regarding the detection of icebergs using SAR data, before outlining various approaches to the detection of icebergs suggested in the literature. The chapter then discusses the main approaches to validating iceberg detections, before finally outlining some of the most important challenges currently faced in the field of iceberg detection using SAR. Chapter 5 provides a summary of the three main publications produced as part of this Ph.D. project and briefly outlines additional contributions to the field. Chapters 6 - 8 compromise those three publications. Finally, Chapter 9 provides the conclusion of this thesis, and outlines future work.

2

Icebergs and the Arctic Environment

This chapter presents some important background information and scientific contributions on icebergs and the Arctic environment that will impact the work carried out in this thesis.

To detect and map icebergs, we must first understand what they are. That is to say, their composition, surface, and volume characteristics, their sizes, shapes, and how they are affected by the environment in which they are found. We will briefly introduce iceberg formation and calving processes, and outline some of the main types of icebergs encountered in the Arctic. Then, we will cover some important physical properties of icebergs, before ending the chapter with an introduction to the Arctic environment[1].

2.1 Iceberg Formation

"*The production of icebergs is fundamentally driven by gravity*" [3]. When snow accumulates on cold land regions over thousands of years, gravity will compress it into firn, then solid ice, forming a glacier. As the weight of the ice increases, the underlying topography of the landscape, unequal distribution of precipitation or ablation, and basal friction or lack thereof will force the ice to move. During movement, cracks and crevasses might occur due to the large mechanical forces

1. For more detailed descriptions of glacier dynamics the reader is referred to Houghton [30], and for a thorough introduction to calving modes to Benn et al. [31], and some illustrations hereof to Bendle [32]. We recommend Thomas [33, Chapter 1] for a thorough description of the physics of sea ice formation, and Bigg [3] for covering many topics important for iceberg science.

in play, and as the ice reaches the ocean, these weaknesses are amplified under the additional strains caused by the tides and ocean waves until, finally, the glacier terminus disintegrates, giving birth to icebergs.

Although marine-terminating glaciers are found in many different parts of the Arctic (Figure 1.1), not all glaciers calve the same quantity of icebergs. The number of icebergs calved from a specific glacier depends on many different factors, such as the specific mass balance of the glacier, i.e., speed, thickness, and width of the glacier, mechanical properties, crevassing, the rate of basal melting, and whether the glacier is floating or grounded [34].

2.1.1 Calving

The shapes and sizes of icebergs are mainly influenced by the calving processes, and although the exact physical processes driving calving are poorly understood [3], some specific modes of calving can be outlined [31].

Larger icebergs are typically the result of sizeable fractures in the ice shelf that occur due to variations in the propagation speeds, or due to the torque from buoyancy forces. When these fractures increase in size, e.g., due to mechanical forces, the intrusion of meltwater (from the top), or warm seawater (from below), fracture propagation can be triggered. Once these fractures grow large enough, sections of the glacier front can break off, giving birth to large icebergs. On the other hand, smaller icebergs are typically the result of force imbalances at the terminal cliff. These can occur if, for instance, the melt rates for the glacier front are greater below the water line than above, resulting in the ice above the waterline being undercut and breaking off into smaller pieces, or due to pressure differences acted upon the glacier above and below the water line. Smaller icebergs can also calve directly from large icebergs, or be the product of the rapid disintegration of large icebergs, which can be caused if the external mechanical forces from waves or gravity are greater than the internal strength of the ice.

2.2 Iceberg Types and Sizes

Icebergs are typically categorized by their shape and size. They are most commonly separated into the six main categories shown in Figure 2.1 [1, 35]. The four types on top, *tabular*, *wedge*, *blocky*, and *dome*, are sometimes merged into a single category called *tabular*, and the two types at the bottom, *pinnacled* and *drydock*, are sometimes merged into a category called *irregular* [34]. Still other categories, such as *ice island*, are used to describe very large tabular

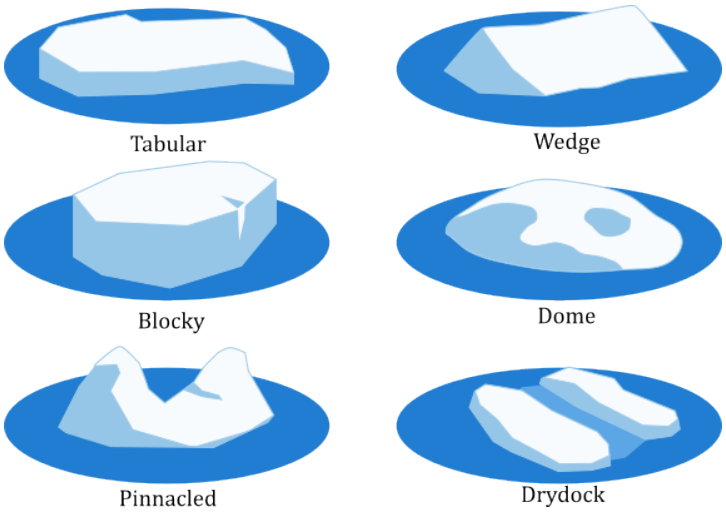

Figure 2.1: Typically used iceberg type categories[2]

Size Class	Height (m)	Length (m)
Growler	<1	<5
Bergy Bit	1-5	5-15
Small	5-15	15-60
Medium	15-45	60-120
Large	45-75	120-200
Very Large	>75	>200

Table 2.1: Iceberg size classes from WMO [1]

icebergs broken off of ice shelves, or *weathered* icebergs, which refers to old icebergs that have undergone several seasons of melting and snow accumulation [1, 36].

The definitions of iceberg size classes according to the World Meteorological Organization (WMO) nomenclature are listed in Table 2.1 [1]. The height, or freeboard, is given relative to the sea level, and the length is of the major axis as seen from a satellite (nadir). Objects from the two smaller classes, *growler* and *bergy bit*, are generally not referred to as *icebergs*, but are still important from an observational point of view as they can cause significant damage to ships and infrastructure.

The size distributions of calved icebergs are an important factor for simulating

2. Graphic inspired by:
`https://commons.wikimedia.org/wiki/File:Iceberg_Shape.svg`
`https://www.britannica.com/science/iceberg/Iceberg-size-and-shape`

ocean dynamics [37, 38]. They can be used to infer glacier calving dynamics, which is useful for mass balance calculations [39, 40]. From an observational point of view, iceberg size distributions are also valuable for determining the probability of encountering small icebergs in a given area, based on the observations of larger ones, as small icebergs often cannot be detected using wide-swath SAR images. In general, iceberg size distributions are described using power law distributions [40], e.g., for several Greenland fjords [38, 39], and for Antarctica [41], although the exact fit varies with the location.

2.3 Iceberg Composition and Physical Properties

Generally, it is assumed that icebergs have a density around 900 kg/m^3 [42, Table 2.1], and as such nine-tenths of an iceberg is below the water-line when floating in the ocean. But this density might vary somewhat depending on the region and the thickness of the glacier from which it has calved. For glaciers in colder regions, the density will slowly increase with depth, from around 400 kg/m^3 for compacted snow at the surface to the 900 kg/m^3 at 100 meters depth [30]. This means that when tabular icebergs calve from one of these regions, their surface will have a layer of snow and firn that is less dense than glacial ice. However, for glaciers in warmer regions, exposed to summer melt which will quickly compact the snow into solid ice, or for icebergs that have turned over after calving or due to unequal melting, their surface will be made up of high-density glacial ice, and in some cases refrozen seawater.

After being compressed into glacial ice, some air inclusions might be present in the ice. The sizes and shapes of air inclusions were measured for a series of East Greenland icebergs [43] and it was observed that the inclusions were mainly of tubular shapes, with a diameter between $0.02 - 0.18$ mm and up to 4 mm in length. Another study sampled icebergs from Labrador and Greenland [44] and found that the diameters of the inclusions were generally around $0.30 - 0.55$ mm, with some inclusions having diameters above 1 mm. It was also observed that the inclusions were evenly spatially distributed.

In addition to air inclusions, some icebergs may also contain debris and sediments. These can be picked up either from the bottom of the glacier when sliding over bedrock [30], or in some cases be the consequence of wind-blown dust, ash from volcanoes, pollution, or even from meteorites being deposited in layers on the glacier [3]. Such layers can create weaknesses in the iceberg structures and are responsible for releasing nutrients and organic carbon as the iceberg melts [8]. An example of a sediment layer can be seen in Figure 2.2.

Figure 2.2: An iceberg observed at the CIRFA Cruise 2022. It is surrounded by fast ice and likely grounded. Notice the sediment stripes running across the iceberg (photo by Wenkai Guo).

Besides the composition of icebergs, another important physical parameter is their temperature. Measurements of the temperature of Labrador icebergs suggest bulk temperatures of around −17 °C, and that the bulk temperature remains relatively stable for icebergs for quite some time after calving (perhaps years) due to the low thermal conductivity of the ice [45], while the temperature of the surface of the icebergs will mirror the temperature of the surrounding air and water.

2.4 Iceberg Drift and Deterioration

The conditions determining whether an iceberg floats to sea are many, from the depth of the water, sea ice conditions, or the thickness of the ice mélange [3]. A large fraction (some studies suggest more than half [7]) of iceberg mass will melt in the fjords where they calved and never reach the open ocean. But some of the icebergs do break free of the ice mélange and drift into the open ocean.

Once out to sea, iceberg movement is affected by many different factors, from atmospheric forces and wind, ocean currents, the Coriolis force, the slope of the sea surface, and the interaction with sea ice on the ocean surface [20, 3]. The speed and heading of the iceberg are determined by the interaction of all

these forces with the complex geometry of the iceberg. Here, smaller icebergs are more sensitive to wind forcing, while larger icebergs are more sensitive to ocean currents [46]. For our work, it is important to note that iceberg speeds can vary considerably, and have been observed to be in the order of a few kilometers per day [46, 47], with some observations of sustained speeds of up to $1.13 m/s$ (around 100 kilometers per day) [48].

Icebergs in the open ocean are also affected by melting, most importantly due to wave erosion at the water/air interface [20], which can be responsible for up to one meter of ice loss per day in slight wave conditions, and high water temperatures, which can be responsible for up to $20cm$ of ice loss per day [3]. The drift and deterioration of icebergs means that, from an observational point of view, they are highly dynamic, with both the position and appearance of an iceberg in the open ocean subject to drastic change in the span of a few days. Therefore, identifying the same iceberg in two different observations can be challenging.

2.5 Sea Ice and Meteorological Conditions

One of the most distinct features of the Arctic Ocean is its sea ice. As temperatures decrease to the north, the ocean starts to freeze over and sea ice forms. When exposed to the dynamic environment of ocean currents, wind, and waves, sea ice will form into pancakes, and then floes of varying sizes, which will collide and deform, creating rafting and ridging when converging, or cracks and leads when diverging. On the other hand, sea ice formed in leads or under calm conditions may form into flat and homogeneous ice. This causes considerable variations in the appearance of sea ice.

As the seawater contains salt, so too will the ice. When ice forms, ice crystals will grow from the water molecules. As salt lowers the freezing temperature, water with a high salt concentration, called brine, collects between the ice crystals, and over time these pockets might merge into brine channels. As the ice gets older, the sea ice undergoes a desalination process, where the brine is expelled, resulting in higher concentrations of salt near the surface and bottom of the ice, and decreasing the overall salt content with age [33]. Brine channels that extend to the surface cause a highly saline surface skim from which frost flowers may form under certain temperature and wind conditions.

Although the winter temperatures in the central Arctic fall below $-30°C$, summer temperatures can be as high as $+10°C$ degrees [49]. Together with the intrusion of warmer waters from the South Atlantic, some ice formed during the winter will melt the following summer, while other floes will survive. Ice

floes observed during the same year as their formation are referred to as First-year ice (FYI). Ice floes that have survived multiple summer seasons are called Multi-year ice (MYI) and typically grow thicker than two meters. In areas with a high degree of convergence, pressure ridges from colliding ice floes can grow thicker than six meters [33] and reach lengths of up to hundreds of kilometers.

Snowfall and precipitation in the Arctic Ocean are sparse, as the main precipitation falls near landmasses and in the North Atlantic. However, some precipitation does fall on the sea ice, with up to 10 cm of snowfall over the central Arctic during the summer season [49]. In some cases, snow depths can accumulate up to a meter in the Arctic, but most snow depths are generally below 40 cm [33]. In the open ocean, wind forcing and currents give rise to waves. In the Barents and Greenland Seas, significant wave heights of three meters are not uncommon [50]. This makes the Arctic a dynamic and complicated environment in which to observe icebergs.

3

Remote Sensing

Using satellite remote sensing, we can monitor the vast Arctic region, with a high repetition frequency. In this chapter, we will cover some of the basics of remote sensing, with a focus on SAR, as this is the main data source for the scientific work carried out for this thesis. However, optical data have also been used in some scientific work, specifically for validation purposes, so this chapter will start with a brief introduction to optical remote sensing.

3.1 Optical Remote Sensing

Optical remote sensing systems measure the natural radiation emitted or reflected from the Earth's surface, with systems mainly designed to measure the light reflected from the sun. The sensor is typically downward-looking, and the images are formed by projecting what is seen in the field of view, through a lens, and onto a Charge-coupled device (CCD) chip. The lens and the number of cells in the CCD chip thus limit the image resolution. As mentioned in Chapter 1, the use of optical systems is severely limited for Arctic monitoring due to cloud cover and lack of sunlight during the winter months.

Nevertheless, optical images from the Sentinel-2 satellite have been used for validation purposes in the scientific work carried out in this thesis: both the visible blue, green, and red bands, at 490 – 665 nm (Band 2-4) and a Near-infrared (NIR) band at 842 nm (Band 8). All of these bands have a spatial resolution of 10 meters, which is typically higher than what is offered by the wide-swath SAR systems. Therefore, optical images offer a good source of independent validation when conditions allow for it.

3.2 SAR Remote Sensing

SAR systems operate by transmitting an electromagnetic signal (a pulse) in the microwave range and measuring the intensity of the signals that are scattered back by targets on the ground. This is referred to as backscatter. By timing the duration between transmission and reception, the distance and hence the location, of the target can be determined. The backscatter intensity of a given target is determined by the geometry of the target and its dielectric properties, determining how much of the incoming signal is penetrating, being absorbed, or scattered by the target [51]. Hence, different targets will return different backscatter signatures, enabling target classification based on the backscatter intensities.

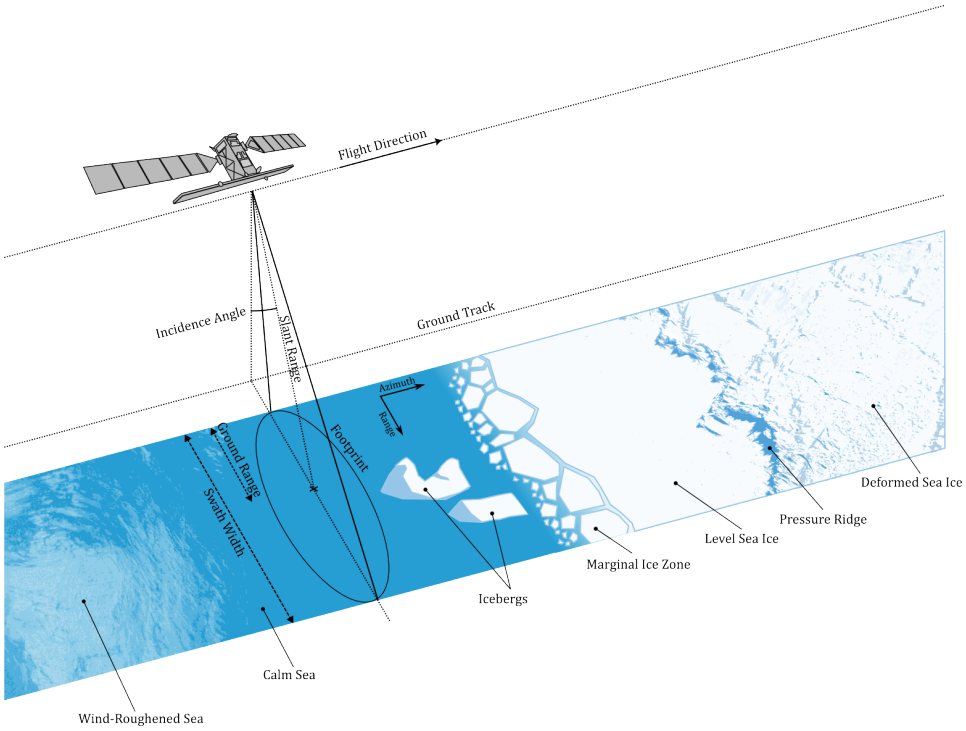

Figure 3.1: SAR stripmap acquisition geometry.

3.2.1 Image Geometry

If a SAR system were to be faced downward, the transmitted signal would arrive at several targets simultaneously, which would result in a mixing of signals from several targets at the receiver. To avoid this ambiguity SAR systems are operated in a side-looking geometry as seen in Figure 3.1. This has the important consequence that the angle at which the transmitted signal is received at the target called the Incidence angle (IA) varies throughout the image, with an

increasing incidence angle for increasing range. Since the backscatter for most targets varies with the incidence angle, similar targets may appear differently in different areas of the image, which has some important implications for target classification [52].

3.2.2 Image Formation

A SAR sensor transmits pulses continuously as it flies along its track, with each pulse illuminating a footprint on the ground. As the sensor flies with a fixed velocity, targets within the same range, but different azimuths, i.e., in front of or behind the sensor, can be separated using the Doppler shifts of the backscattered signals. If the targets are stationary, these Doppler shifts can be used to keep track of where in azimuth a target is located and thus increase the azimuth resolution of the image[1].

There are a lot of trade-offs in the design considerations of SAR systems. If the Pulse-repetition frequency (PRF) is too high, reflections from successive pulses may overlap and cause ambiguities, e.g., a strong target far away is interpreted as a weak target close to the SAR [54]. The PRF also determines the SAR system's ability to separate targets with different Doppler shifts, meaning that if the PRF is too low, there is a risk of azimuth aliasing (or Doppler aliasing), where a target is misplaced relative to its Doppler frequency. These azimuth ambiguities can cause ghost targets to occur in the image [53, Ch. 23 and 25].

Due to the image formation, the resolution of SAR images depends on different factors in the range and azimuth dimensions. The range resolution depends on the bandwidth of the transmitted pulses and can be controlled by modulating the transmitted pulse using pulse compression. The azimuth resolution depends on the length of the synthetic aperture, with a larger antenna beamwidth permitting longer observation times and thus a longer synthetic aperture [53, Ch. 31]. A resolution cell of a SAR image is therefore typically not square, but rather rectangular, normally with a high range resolution and a slightly lower azimuth resolution.

Another important factor is the impulse response of the SAR system. Due to the limitations of the sensor, a target cannot be perfectly resolved but extends over several pixels in both the range and azimuth direction, albeit with limited signal intensity. For distributed targets, e.g., open water or sea ice, the impulse

1. SAR image formation is a complex topic that is covered in detail in Chapter 2 of the SAR handbook [51] and in Moreira et al. [25]. More in-depth explanations are presented in Chapters 30-33 of Stimson [53].

response is typically not visible, as the unwanted signals extending to the neighboring pixels are much weaker than the main signal from the neighboring pixels. However, if a very strong target exists in an environment where the surroundings exhibit very low backscatter, the impulse response might become visible, causing the target to be larger than its physical size.

After image formation, SAR images are normalized to σ^0, i.e., the normalized radar cross-section, describing the percentage of the incoming energy that is reflected by an object on the ground and measured by the sensor [51]. SAR images are typically spatially averaged (multilooked) in order to limit the speckle noise (see Section 3.3.3); this is normally done in a way so the resulting pixels are close to square.

3.2.3 Acquisition Modes

Figure 3.1 shows an illustration of a SAR sensor moving along a track and continuously mapping the area. This type of acquisition mode is called *stripmap* mode. In *stripmap* mode, the antenna orientation is set to a fixed side-looking geometry, and pulses are transmitted continuously. However, more advanced imaging modes also exist, e.g., by using a phased array antenna that can be pointed in specific directions. Besides *stripmap*, other typical modes are *scanSAR* and *spotlight*.

In *scanSAR* mode, the antenna elevation is changed periodically, such that multiple ground tracks (sub-swaths) are created simultaneously. This enhances the swath width but comes at the cost of reduced observation times for each sub-swath, reducing the azimuth resolution. For operational monitoring, Sentinel-1 Interferometric wide-swath (IW) and Extra wide-swath (EW) modes use a special form of *scanSAR* called *TOPSAR* (Terrain Observation by Progressive Scans) [55]. Here, in addition to changes in the antenna elevation, the antenna is also steered sideways to enhance image quality.

Spotlight mode is used to obtain images at a higher resolution than is possible with *stripmap* or *scanSAR* modes. This is done by steering the antenna beam toward a fixed spot on the ground as the satellite passes by. This increases the observation time, and hence azimuth resolution, but prevents continuous monitoring along the flight track.

Band Designation	Frequency Range	Wavelength
VHF	30–300 MHz	10–1 m
UHF	300–1000 MHz	1–0.3 m
L	1–2 GHz	30–15 cm
S	2–4 GHz	15–7.5 cm
C	4–8 GHz	7.5–3.75 cm
X	8–12 GHz	3.75–2.5 cm
Ku	12–18 GHz	2.5–1.67 cm

Table 3.1: Standard radar-frequency bands [56]

3.3 SAR Features

SAR systems possess some important features that affect the analysis of target properties. Some of the most important are the center frequency at which the SAR operates, and the polarization of the transmitted and received signals.

3.3.1 Frequency and Wavelength

The transmitted signal from a SAR sensor is centered around a specific center frequency and is named according to the corresponding band [56]. Typically used frequencies for SAR systems range from 10 GHz for X-band systems, over 5 GHz for C-band systems, to 1 GHz for L-band systems, as shown in Table 3.1. The type of bands used has some important implications for target classification, as high radar backscatter generally occurs when the target roughness is comparable to the radar wavelength [57].

As mentioned earlier, the dielectric properties of a target determine how much of the incoming signal is scattered and absorbed. An important concept here is that the penetration depth of a microwave signal typically increases when the wavelength is increased (decreased frequency) [57, Ch. 5]. This means that using, for instance, an L-band sensor results in higher signal penetration than C- or X-band, and hence an L-band SAR can *see* deeper into a material than C-band SAR.

3.3.2 Polarization

Another important concept for SAR is the polarization of the microwave signal. Here, polarization denotes the orientation of the propagating electric field [51]. For most SAR systems, the signals are transmitted and received at different

polarizations. The reason for doing this is that various media interact and reflect polarizations differently. For example, some targets will be able to change the polarization of an incoming signal, so that the reflected signal is oriented differently. That is, the polarization of a reflected signal depends not only on the polarization of the transmitted wave, but also on the target structure. Consequently, the characteristics of the polarization of transmitted and received signals can be used to describe targets [53, Ch. 4].

Typically, a linearly polarized signal is transmitted, i.e., polarized, in horizontal (H) or vertical (V) orientation and, similarly, horizontal or vertical polarizations are received. Each channel can then be denoted with two letters describing the transmitted and received polarization, e.g., HH denotes a signal that has been transmitted and received horizontally, while HV denotes a signal that has been transmitted horizontally and received vertically. By using only four polarizations, i.e., transmit and receive in both H and V, the full polarimetric characteristics of a target can be obtained. This is referred to as quad-pol or fully polarimetric[2] [25]. The scattering mechanisms (and hence polarization characteristics) of sea ice and icebergs will be covered in Chapter 4.

3.3.3 SAR Disturbances

The image formation techniques used to generate SAR images are also responsible for some distinct types of noise and artifacts that can impede target identification.

The most well-known type of noise in SAR images is speckle. Speckle arises from the fact that to keep track of the Doppler shift for received signals, SAR measures both amplitude and phase. For distributed targets, a given resolution cell may contain many different scatterers, from which a signal is backscattered to the sensor. Due to variations in the scatterers, these signals differ in amplitude and phase and interfere with one another. If the number of individual scatterers is large the resulting total signal from a resolution cell can be described as a stochastic process. As a result, distributed targets exhibit a considerable intensity variation, called speckle. On the other hand, if any single scatterer dominates within a resolution cell, this randomness is not present[3].

Another type of disturbance in SAR images arises from thermal noise. Thermal noise is a type of constant additive noise present in all electronics, and should

2. SAR polarization (PolSAR in short) is an extensive topic that will not be covered in detail here due to our work being limited to dual polarization data.
3. For an introduction to speckle, and specifically speckle filtering, the reader is referred to Argenti [58].

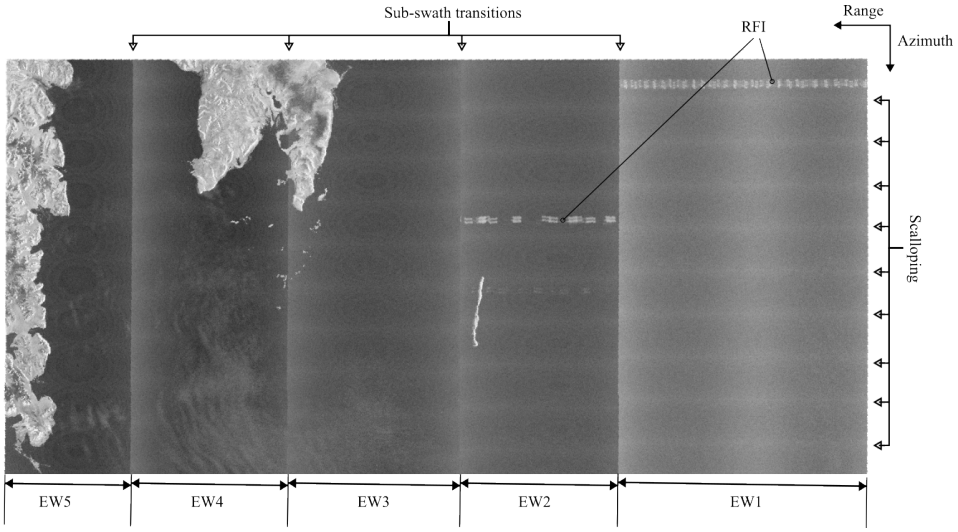

Figure 3.2: Sentinel-1 Extra Wide Swath (EW) mode from southern Svalbard. Disturbances are seen in the transitions between the sub-swaths. EW1 is particularly affected by scalloping. This image also highlights several instances of RFI, possibly from ship radar.

intuitively be constant throughout an image. However, due to unequal antenna gain the Signal-to-noise ratio (SNR) within a swath can vary. These variations, occurring in both the azimuth and range direction, are referred to as scalloping. *TOPSAR* acquisition mode tries to avoid some of these issues by steering the antenna side-ways (in azimuth) [55]. However, *TOPSAR* can still show scalloping [59], such as in sharp intensity variations in the sub-swath transitions along the range direction, or varying noise intensity in the azimuth direction as seen in Figure 3.2. This is especially visible in the cross-polarization (HV or VH) channels over open water and ice, where the backscatter intensity (the signal component) is quite low.

In addition to speckle and scalloping, SAR images sometimes show signs of Radio-frequency interference (RFI). RFI occurs when sources on the ground emit microwave radiation in the frequency band at which the SAR operates. For instance, this could be ship-mounted radars or communication systems. Figure 3.2 shows examples of RFI in the first two sub-swaths.

4

SAR Remote Sensing of Icebergs

In this chapter, we will combine the concepts presented in Chapters 2 and 3 about icebergs, the Arctic environment, and remote sensing, to introduce the most important aspects of SAR remote sensing of icebergs. The chapter will briefly introduce the common backscatter characteristics of icebergs and their surroundings and discuss the most important iceberg detection approaches and their inherent challenges. Then, we will discuss the importance of validation data and why these data are hard to obtain. Finally, we will cover some of the main challenges we currently face in detecting icebergs using SAR remote sensing.

Figure 4.1 shows a small section of an ALOS-2 image, highlighting the highly variable environment in which icebergs can be found. Although clusters of icebergs are visible as small, bright outliers, several elements in the image impede their detection. The image contains land and islands, broken sea ice, and various sea states. One can also see the noise from a subswath transition.

To detect icebergs in SAR images, an algorithm is needed that can separate iceberg backscatter signals from the background, which will consist of either open water, sea ice, or a mix of the two. For accurate detection, the iceberg backscatter signals must be distinguishable from the background backscatter signals [60]. In reality, and as we will show below, there is often an overlap in backscatter signals from icebergs and their background environment. Therefore, an iceberg detection algorithm should try to achieve a good trade-off between maximizing the number of detected icebergs, while minimizing the number of missed and false detections.

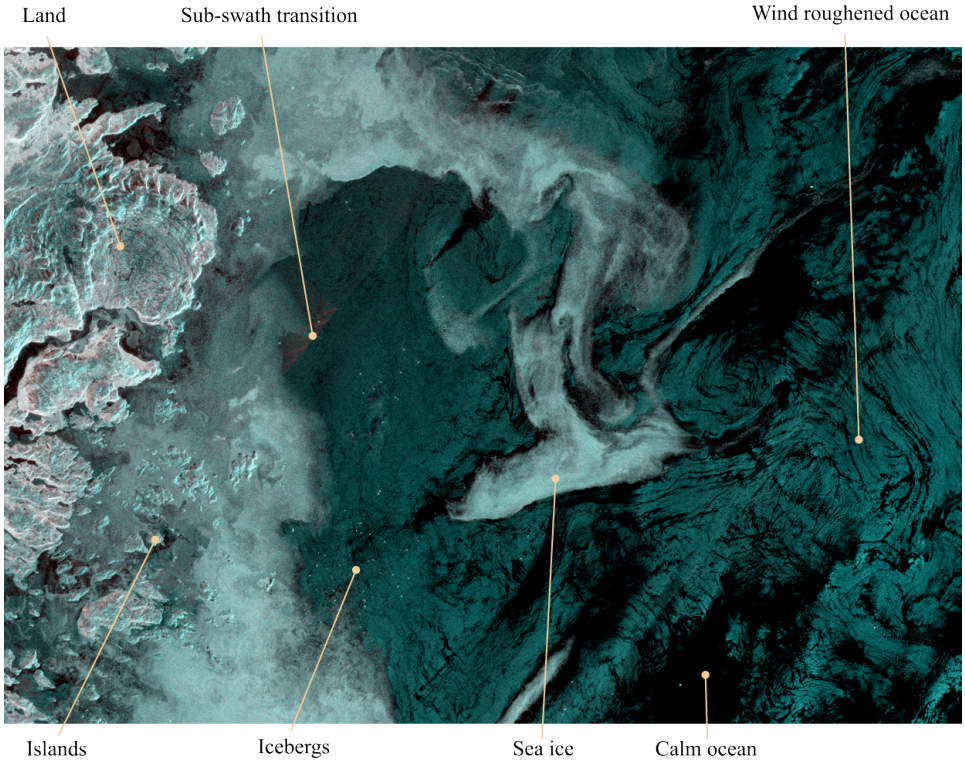

Figure 4.1: Examples of icebergs in an ALOS-2 image acquired over the Labrador Sea. Legends have been added that identify features of the complex environment in which icebergs need to be detected. The image covers an area of approximately 140 × 100 km.

4.1 Iceberg Backscatter

SAR scattering can be separated into three distinct scattering types: surface scattering, volume scattering, and double bounce, as seen in Figure 4.2. Natural targets, such as icebergs, are generally assumed to exhibit some combination of these three distinct scattering mechanisms [51].

So far, only a few studies have investigated the scattering mechanisms of icebergs. Kim et al. [61] showed that icebergs in West Antarctica from C-band were characterized mainly by volume scattering, with some double bounce and minor surface scattering contributions. Dierking and Wesche [62] also investigated Antarctic icebergs using C-band SAR and found substantial volume scattering and a high variation in iceberg backscatter signatures. In addition, they noted that the exact scattering mechanisms were rather variable, with indications of multiple scatterings within the firn of some icebergs. A more recent, 2020 study by Himi et al. [63] investigated the C-band backscatter signatures of a large number of icebergs in sea ice and open water at varying

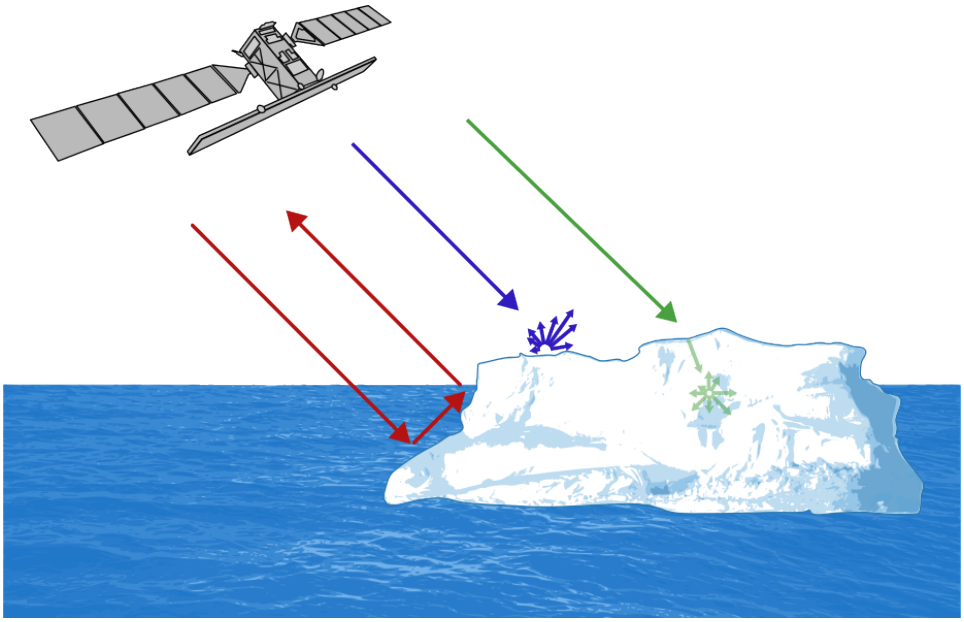

Figure 4.2: Typical iceberg scattering mechanisms. Volume scattering (green), surface scattering (blue), and double bounce (red).

wind speeds. Their results showed that the dominant scattering mechanism was surface scattering. The differing scattering mechanisms most likely are due to the different environmental conditions in which data were collected, with Dierking and Wesche [62] investigating icebergs under freezing conditions, while the study from Himi et al. collected data under melting conditions. Radar signals tend to penetrate less deeply under melting conditions due to the presence of liquid water on the surface of the iceberg. Himi et al. also showed that scattering mechanisms for icebergs surrounded by sea ice differ from those of icebergs in open water.

In a study by Ferdous [64], simulated data from an electromagnetic simulation tool were used instead of real SAR data. Their results showed that the surroundings of an iceberg influenced the total scattering signatures from the icebergs, likely due to variations in double bounce contributions for different sea states, suggesting that different wind speeds and directions might influence the total backscatter intensity received from an iceberg. This study also observed that both the iceberg geometry and iceberg orientation affected the resulting iceberg backscatter intensity. For L-band, a study by Bailey [65] showed that icebergs mainly exhibited surface scattering and that icebergs at different locations exhibit different polarimetric characteristics. However, this latter observation could be related to variations in temperature, as only the minimum temperature of each site was reported in the study. Ultimately, the results suggest that colder conditions may produce more volume scattering.

All of the studies referred to above suggest that icebergs exhibit a variety of scattering mechanisms. Temperature appears to be a key factor influencing the scattering mechanisms, with icebergs exhibiting a high fraction of volume scattering in freezing conditions, while melting conditions lead to more surface scattering. In addition, the total scattering intensity appears to be influenced by many different parameters and may change based on wind speed, wind direction, iceberg orientation, iceberg geometry, calving location, and signal frequency.

4.2 Backscatter of the Iceberg Surroundings

4.2.1 Sea Ice Backscatter

The characteristics of sea ice backscatter depend on sea ice properties, meteorological conditions, and radar parameters. Sea ice properties include the sea ice type, level of deformation, or snow cover on the ice. Sea ice backscattering changes are most noticeable when temperatures change between freezing and melting conditions. Additionally, radar parameters such as incidence angle, polarization, and wavelength of the sensor also influence the backscattering characteristics[1].

Older ice generally shows higher backscatter intensity due to lower salinity and an increased number of air bubbles [66, Table 8.1]. Areas with deformation zones, such as ridges and rubble fields, will also show higher backscatter intensity than surfaces with level sea ice. For temperature, the onset of the melt season is characterized by an increase in backscatter intensity of FYI and a decrease for MYI [67]. This holds true for both C- and L-band SAR images [68]. The use of different polarizations offers an additional distinction between sea ice types and deformation processes from SAR. As for the incidence angle, sea ice, in general, has been shown to exhibit a linear decrease in backscatter in the decibel domain with increasing incidence angle [52], with variations between 0.1-0.4 dB/degree, depending on the sea ice type for C-band [69]. Consequently, young and level sea ice, and high incidence angles, offer the lowest backscatter intensity and thus the highest contrast between icebergs and sea ice.

1. For an overview of sea ice mapping with SAR the reader is referred to Dierking [66].

4.2.2 Open Water Backscatter

Whereas sea ice backscatter is characterized by a combination of surface and volume scattering, the backscattering of open oceans predominantly arises from surface scattering due to the large dielectric loss factor, and hence small penetration depth, of radar signals into the water. A perfectly smooth ocean thus behaves like a specular reflector and will exhibit very low backscatter intensity when the incidence angle is above zero [57]. However, wind and currents lead to a roughening of the ocean surface, giving rise to backscatter returns for incidence angles above 0.

Wind forcing generates two different types of waves on the ocean surface, gravity waves and capillary waves. Gravity waves tend to have wavelengths longer than a few centimeters. Capillary waves have wavelengths shorter than a few centimeters [57]. A high SAR backscatter intensity from open water occurs when the ocean waves are similar in length to the radar wavelength [70, Chapter 2]. Because of this, the presence of capillary waves can result in high backscatter intensity when imaged with high-frequency SAR sensors, such as X-band. Lower frequencies, such as C- and L-band, are less sensitive to these waves but more sensitive to longer wavelengths.

Higher winds will generally lead to higher surface roughness and result in a higher backscatter intensity, depending on the wind direction, with wind directions 0 or 180 degrees relative to the SAR look direction resulting in the largest backscatter intensity [71]. Similar to what has been observed for sea ice, there is a linear relationship (in the decibel domain) between backscatter intensity and incidence angle for open water using typical SAR incidence angles, with decreasing backscatter intensity for higher incidence angles. Consequently, low winds and high incidence angles offer the lowest backscatter intensity and thus the highest contrast between icebergs and open water.

4.3 Iceberg Detection Algorithms

Backscattering signatures of icebergs, sea ice, and open water depend on a wide range of parameters. As such, no fixed scattering signature for either icebergs or their background exists, as both depend on local conditions. Therefore, iceberg detection algorithms must consider the highly variable nature of the scattering characteristics or be tailored to local conditions.

A scatterplot of Sentinel-1 samples (C-band) from icebergs and open water is shown in Figure 4.3. The figure shows that the iceberg backscatter is highly variable, with values ranging from −35 to −5 dB for the HV band, and −25

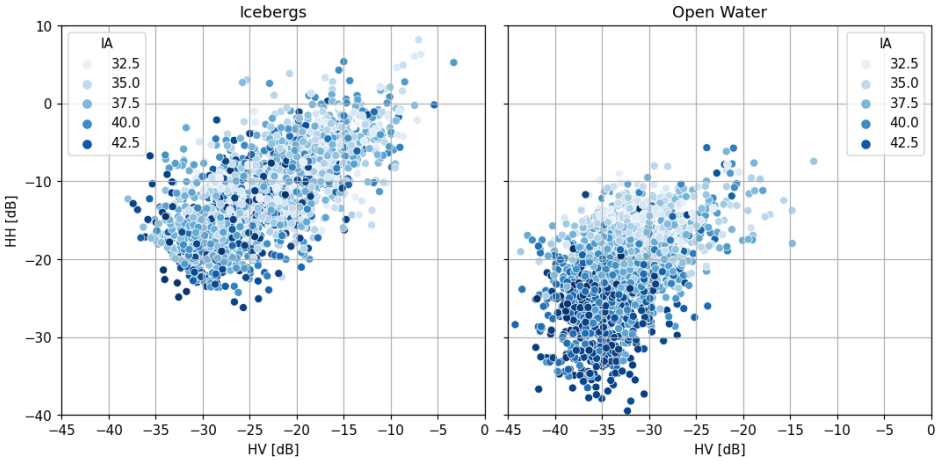

Figure 4.3: Scatterplot of iceberg and open water backscatter intensity. These data consist of C-band SAR samples and were extracted from the Labrador Sea dataset used in Paper 1 (Chapter 6).

to 5 dB in the HH band. This variation does not appear to have any strong correlations with the IA. Since the data were collected under melting conditions, which suggests a dominance of surface scattering, the variations are likely caused by changes in the iceberg's surface roughness and geometry. Looking at the open water samples on the right, a much stronger correlation with the incidence angle is seen, with generally lower backscatter for higher incidence angles. Comparing the two classes reveals a considerable overlap. Consequently, a robust separation between the two based on overall backscatter characteristics will not achieve satisfactory results. The task is further complicated if icebergs are surrounded by sea ice, which often exhibits even larger variations of backscatter intensity depending on the sea ice type, snow cover characteristics, and deformation. Better techniques are needed to separate icebergs from their surroundings. Currently, this separation is solved in two ways: 1) by using classification and segmentation methods in which additional parameters besides the backscatter are utilized, or 2) by using local outlier detection methods.

4.3.1 Segmentation and Classification Methods

Segmentation and classification describe two different machine-learning approaches. In segmentation methods, the pixels in the SAR image are separated into groups, often without any prior knowledge of the target distribution (i.e., an unsupervised method). Classification methods, on the other hand, rely on giving labels to pixels in the image, typically based on previously collected data

(i.e., a supervised method). Both methods have been employed for detecting icebergs. Often, studies have relied on some combination of segmentation and classification to obtain the most robust results.

Akbari and Brekke [72] used an Expectation-maximization (EM) segmentation algorithm based on backscatter and polarimetric features to group pixels in C-band SAR images. A set of pre-defined rules was then used to discriminate between groups consisting of open water, sea ice, and icebergs. This was done mainly by taking into account the brightness and shape of individual objects, the assumption being that icebergs tend to be small, round, and bright. Similarly, Barbat et al. [73] suggested a combination of segmentation and classification: the authors used a super-pixel segmentation method to group neighboring pixels of high similarity, before classifying the segments based on a supervised random forest classification algorithm utilizing texture features to improve the accuracy. The approach was later employed to derive the distribution of near-coastal Antarctic icebergs for three years [41]. Wesche and Dierking used an approach based entirely on backscatter intensity to map the near-coastal distributions of icebergs in the Antarctic [37]. In their study, the investigation of 281 icebergs and 23 sea ice areas was used to derive a suitable backscatter intensity threshold for the separation of sea ice and icebergs. To improve its robustness, the method only considered objects larger than 30 pixels. A recent study by Evans et al. [74] used a recursive segmentation algorithm to map large icebergs in the Antarctic across different seasons. This method performed very robustly but remains to be tested on a larger scale.

Braakman-Folgman et al. employed a special type of classification method based on Convolutional neural networks (CNNs) for the detection of very large Antarctic icebergs [75]. In CNNs, convolutional kernels of various sizes adapt to the training data to detect simple features such as edges and corners. These features are then combined to consider more details of the shape and texture of the objects, which can then be applied to detect similar features in new data. The advantage of this is that the feature detection algorithms do not need to be engineered manually. However, the downside is the need for accurate training data, which are hard to obtain (see Section 4.4).

Common to studies using classification and segmentation methods for iceberg detection is that they have mainly been employed for Antarctic icebergs, except for the study conducted by Akbari and Brekke [72]. In Antarctic iceberg research, the environmental impact of huge (kilometer-scale) icebergs is the main driver. Here, it is straightforward to extract texture and shape features at the SAR resolution scale. Arctic icebergs, which are generally shorter than 200 meters, are too small for the extraction of texture features, and their shape is often distorted by SAR artifacts such as the impulse response from point targets.

Furthermore, even for areas with a high iceberg density in the Arctic, the total fraction of pixels covered by icebergs is very small, and it is not unusual for a SAR image to contain 1% or less iceberg pixels. This imbalance means that Arctic icebergs are ill-suited for classification and segmentation approaches. Consequently, Arctic icebergs are hard to characterize and likely to be lost in the noise when analyzing an entire scene.

4.3.2 Constant False Alarm Rate Methods

Due to the challenges inherent to both classification and segmentation methods, iceberg detection in the Arctic typically uses local adaptive outlier methods, such as the Constant false alarm rate (CFAR) approach. The CFAR approach assumes that icebergs generally appear as small, bright objects in the SAR image. However, instead of attempting to characterize the iceberg backscatter intensity globally in the SAR scene, which would typically not be successful due to the overlap in backscatter between icebergs and the surrounding classes (see Figure 4.3), the method is based on finding local outliers. Instead of attempting to identify whether a pixel belongs to an iceberg class, it attempts to determine whether a pixel is unlikely to belong to the background. This is also referred to in the literature as anomaly detection [76].

In the CFAR approach, each pixel is compared against a small local neighborhood, typically in a square or circular window centered around the Pixel under test (PUT), referred to as the clutter estimation window. If the backscatter intensity of the PUT exceeds a certain threshold, it is marked as an outlier. Here, the threshold is determined based on the backscatter intensity in the clutter estimation window. A suitable Probability density function (PDF) of the backscatter intensity, $P(I)$, is used to model the background clutter, and then, the threshold, t, is determined based on an acceptable Probability of false alarm (PFA) rate as [77],

$$P_{fa} = \int_t^\infty P(I)dI = 1 - \int_0^t P(I)dI \tag{4.1}$$

I.e., the threshold is set such that the clutter only exceeds the threshold at a constant PFA rate, giving rise to what is called the constant false alarm rate. The CFAR detector thus adapts its threshold to local variations in the background clutter by looking for small targets that have a high contrast relative to the background.

CFAR detectors have been widely used for iceberg detection in the Arctic, using C-band [60, 77], X-band [78], and L-band SAR [79, 80]. Primarily, CFAR has

been adopted for detecting icebergs in open water, although some attempts to detect icebergs in sea ice have been carried out [81, 82, 83, 84].

There are a few design considerations that need to be taken into account when using a CFAR detector. These are 1) the choice of the PDF used to model the background clutter, 2) the design of the clutter estimation window, and 3) what to do if multiple polarizations are available.

Choice of PDF

Modeling the clutter distribution for various targets is an important topic in SAR, and many different models have been suggested for various target types [85]. For distributed targets, i.e., when a high number of scatterers exist within a single resolution cell, as is the case for natural terrain, the speckle model gives rise to gamma distributed clutter for multi-looked backscatter intensity data [58], and gamma distributions have been widely used for CFAR detection [77, 86, 87]. However, when the targets exhibit a high degree of texture, the clutter distribution is often described using the product model [76]. Here, the distribution is understood as arising from two unrelated processes, namely the texture of the target and the speckle, giving rise to a K-distribution for multi-looked backscatter intensity data. The K-distribution has also been widely used for CFAR detectors [60, 88, 89, 90]. However, simpler models have also been suggested, such as the log-normal distribution [86, 91].

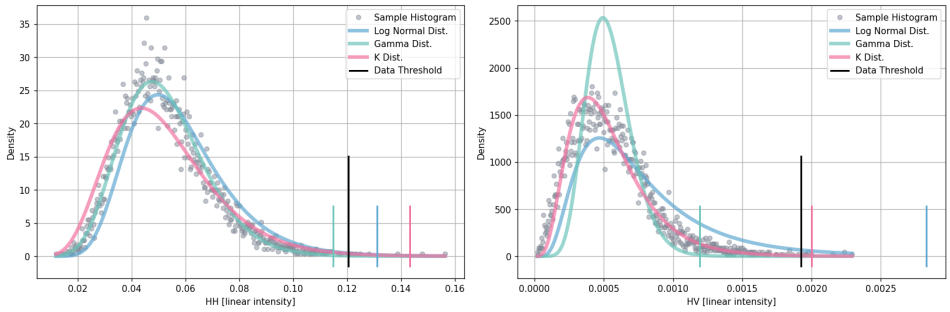

Figure 4.4: Modelling of open water backscatter using Sentinel-1 C-band data showing the HH band (left) and HV band (right). All samples were extracted at an incidence angle of 30°. The vertical lines mark the threshold for each of the models at a PFA level of 10^{-3}, with the black line marking the true threshold, as based on the samples.

In Figure 4.4, three well-known PDFs have been used to model open water clutter of a homogeneous section in a C-band Sentinel-1 image. In total, 10.000 samples were extracted at an incidence angle of 30°. For each of the three PDFs, the derived threshold based on a PFA rate of 1×10^{-3} is marked by

the colored lines. In addition, a threshold based on the data is shown as a black bar. As seen in the figure, none of the three models is a perfect match for the example data, with large discrepancies in the theoretical and desired thresholds.

Window sizes

Under ideal conditions, the backscatter in the clutter estimation window is homogeneous and can be modeled using one of the aforementioned distributions. A large clutter estimation window is then preferred for increasing the number of samples and avoiding bias when estimating the PDF parameters. However, icebergs are found in dynamic environments where the background clutter distribution can change rapidly due to factors such as changes in sea ice concentration, sea surface roughness, or sub-swath transitions. As such, using a large clutter estimation window increases the risk of including samples that belong to different background types, which increases the risk of biasing the PDF estimation.

In addition to the clutter estimation window, a guard area is normally defined around the PUT to avoid including samples from an iceberg in the center of the window and biasing the clutter estimation. The size of this guard window is typically defined according to the maximum size of icebergs expected in the area to which the CFAR detector is applied [91].

Multiple polarizations

As mentioned in Chapter 3, SAR data often contains several polarizations, which gives rise to the question of how these should be used for CFAR detection. Three possible solutions exist [86]. First, CFAR detectors are applied to the individual polarizations and the results are combined based on some pre-defined rules (e.g., Boolean algebra). Second, several polarizations can be combined into a single channel in which outliers can be detected using a single channel CFAR detector. Third, a multidimensional PDF can be used to detect outliers in all polarizations simultaneously.

In Figure 4.5 the data used in Figure 4.4 are shown in a two-dimensional scatterplot. Here, a gamma distribution is used to calculate the thresholds for a PFA rate of 1×10^{-3} for both the HH and HV bands, which are then marked with the shaded green areas. Additionally, the threshold from a Normalized intensity sum (NIS) detector, again with a PFA rate of 1×10^{-3}, has been added as the black line [92]. In the NIS detector, a new channel is formed by the normalized intensity sum of the individual SAR channels, which is then fed to

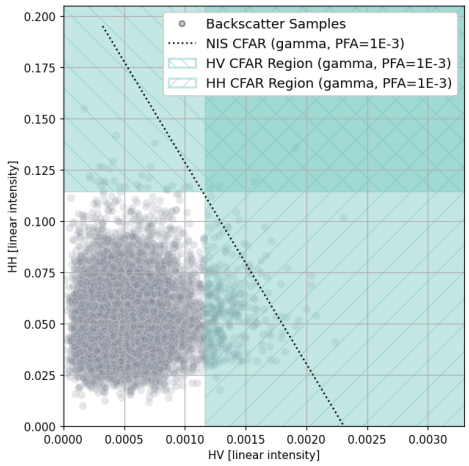

Figure 4.5: Two-dimensional CFAR thresholding using a gamma detector (green) or a NIS detector (black line). This figure was created using the same data as used in Figure 4.4.

a gamma PDF CFAR detector. If detections are made on this dataset based on a combination of the individual channels, a boolean OR operator would mark every sample in the shaded green area as an outlier, while a Boolean AND operator would only mark the samples in the combined top-right area. The NIS detector would mark every sample to the right of the dotted line as an outlier. From Figure 4.5 it is obvious that the way in which the bands are combined has major implications for the results obtained by the CFAR algorithm.

4.4 Validation of Iceberg Detections

Any iceberg detection algorithm must necessarily be validated to characterize its performance. This is especially critical if the algorithm is to be used in an operational system, or if the algorithm is to be applied to a large time series of images, e.g., historical archives of satellite data.

Validation of iceberg detection algorithms has generally been done in three ways: 1) by comparing the algorithm output with manually derived iceberg locations from the SAR image, i.e., using expert interpretation, 2) by comparing the algorithm output with in-situ observations, e.g., observations from airplanes or ships, or 3) by comparing the algorithm output with independent remote sensing images.

Using expert interpretation is generally the simplest validation method, as

no additional data need to be acquired. Instead, pixels that likely represent icebergs can be marked directly in the SAR image, and the performance can be evaluated accordingly. This approach was used by Marino et al. [81], Akbari and Brekke [72], and Bailey et al. [65], among others. The main downside of this approach is the lack of confidence in knowing whether the objects used for validation are real icebergs or whether small ice floes, boats, or noisy patches are being falsely interpreted as icebergs. There is also a lack of knowledge regarding icebergs that cannot be identified in the SAR image, such as when they are masked by the background clutter. For this reason, this method cannot be used to infer knowledge about the number of missed detections, especially when considering icebergs that are smaller than the SAR resolution level.

Using in-situ validation data typically allows researchers to gather higher-quality data. Under ideal conditions, the iceberg's location, shape, and size, as well as general environmental conditions such as temperature, sea state, and sea ice observations, are marked down at the time of the satellite overpass. However, this can be logistically challenging, especially considering that many iceberg observations are needed due to the highly variable backscatter characteristics (see Section 4.1). As an example, Denbina and Collins [93, 94] obtained the location of 25 icebergs distributed over 12 SAR scenes using ship observations, and Power et al. [60] used 22 iceberg observations obtained from airplanes distributed over two SAR scenes for validation. Attempts have been made to use ground-based radar systems as an alternative [72, 95]. However, ambiguities in these data can make it difficult to distinguish small icebergs from the background, thus making the approach less useful.

Using optical satellite images for validation can be an alternative to in-situ observations. Many optical systems tend to provide a higher resolution than wide-swath SAR missions (see Section 3.1) and, as such, using optical satellite images can help to determine the location of icebergs that cannot be visually identified in the SAR images and thus increase confidence in the true number of missed detections. In addition, optical satellite images can cover a large area, providing many observed icebergs, and can be used to accurately determine which areas do not contain any icebergs. However, the use of optical remote sensing introduces some of its own complications. Firstly, optical remote sensing satellites are often placed in a sun-synchronous, noon-midnight orbit to minimize shadows cast by targets on the ground. SAR satellites, however, are often placed in a dawn-dusk orbit to maximize the power received by the solar panels. This generally leads to a time difference of several hours between acquisitions, making validation of icebergs in open water difficult due to the drift of icebergs occurring within this time frame (see Section 2.5). As such, optical satellite images have mainly been used for the validation of icebergs that are either grounded [96] or located in land-fast ice [82, 83].

Once validation data are available, questions then arise about the specific validation method. Detections can be separated into three categories, True positives (TPs) (correct detections), False positives (FPs) (incorrect detections), and False negatives (FNs) (missed detections). Performance scores such as recall, precision, and F1-score can then be calculated from these values [97]. In some cases, a pixel-wise validation method is adopted, where each pixel from the detection algorithm is compared against the validation data [95, 82, 93]. The main weakness of this approach is that small ambiguities between the location and shape in the validation data, and the location and shape of the detected objects, can impair the performance.

As such, object-based validation is sometimes adopted [83, 72]. In object-based validation, groups of connected pixels are treated as a single object. These objects can then be compared to the validated iceberg locations. As a result, if there is an overlap between an object from the detection algorithm and a validated iceberg location, the object is treated as a true positive.

4.5 Current Challenges

So far, this chapter has outlined the background theory, as well as the current approaches to iceberg detection in SAR imagery. But we have also alluded to several challenges, which we will cover in more detail below.

4.5.1 Challenges with the CFAR approach

CFAR is a robust and pragmatic approach that has been widely adopted for iceberg detection. However, despite solving some of the major challenges encountered by the classification and segmentation models, several challenges have yet to be overcome if the CFAR approach is to be used for robust iceberg detection.

Figure 4.4 illustrates that even under ideal conditions (a very large number of samples and homogeneous clutter), the threshold found by the CFAR detectors, intended to delineate outliers from the background clutter, shows discrepancies compared to the threshold derived from the data. It is also obvious that different models are better suited to the different polarizations of this example. This discrepancy arises because the theoretical PDF does not match the actual conditions in the image. It is to be expected that under poorer conditions the models will likely perform less well, e.g., if using a small number of samples, attempting to perform detections in highly varying clutter, or if noise from RFI or subswath transitions is present. Furthermore, for some PDFs it is not

possible to invert Equation 4.1 to obtain a threshold analytically and, as such, numerical estimations are needed, which introduces a new set of problems related to precision and computation time [98]. This leads to an important consideration, namely that the theoretical PFA rate defined in the CFAR detector does not necessarily correspond to the actual number of false alarms found by the detector. So, to say something about the actual performance of a CFAR detector on real SAR images, the output of the detector needs to be compared against independent validation data, as suggested in Section 4.4.

As for the choice of window sizes, it was mentioned in Section 4.3 that the design of the clutter estimation window and guard area relies on the trade-off between obtaining a high number of samples while seeking to avoid including samples from different clutter distributions and masking icebergs at the center of the window. Consequently, the guard area should be designed according to the maximum iceberg size, meaning that the dimensions of the guard area must be twice the maximum iceberg length if the full extent of the iceberg is to be detected. Typically, when icebergs are detected in open water using scanSAR images with a moderate resolution, the largest expected icebergs in the Arctic will be in the order of a few pixels in length, meaning that the dimensions of the guard area will only be moderately sized. However, when the SAR resolution is increased, or when detections are performed closer to calving sites, where the icebergs are larger, the guard area dimensions required increase, and so to obtain enough samples the clutter estimation window must also be enlarged. However, enlarging the clutter estimation window risks weakening performance as it is more likely to include samples from heterogeneous clutter. This problem is likely to become more critical when considering icebergs in sea ice, as sea ice exhibits much greater backscatter variation than open water.

4.5.2 Icebergs in sea ice

A review of the literature shows that most attempts to conduct iceberg detection in the Arctic have been made for open-water environments using outlier detection methods such as CFAR (see Chapter 4.3). While CFAR is well-suited for the detection of icebergs in open water due to the relatively high backscatter contrast between open water and icebergs, only a few attempts have been made at developing methods for detecting icebergs in sea ice, and these attempts have either used fully polarimetric data [80, 82], or shown difficulties in making detections [83], especially for MYI [84]. As a consequence, icebergs in sea ice are not included in the operational iceberg detection products (see Chapter 1).

4.5.3 L-band or C-band for iceberg detection

As outlined in Chapter 1, operational iceberg monitoring of the Arctic is currently carried out using mainly C-band systems, and although C-band SAR will continue to provide valuable data in the coming years, these systems will be supplemented by a series of recent and new L-band missions.

Using L-band SAR for iceberg detection might offer some interesting advantages compared to C-band. Due to its longer wavelength (see Table 3.1), L-band penetrates more deeply into snow and ice and is less sensitive to small-scale surface roughness. The former could help separate sea ice and iceberg backscatter signals, and the latter could improve iceberg detection in wind-roughened open water. Nevertheless, studies using L-band SAR for iceberg detection are sparse due to the limited data currently available, and at the beginning of this project no direct comparisons of L- and C-band SAR for iceberg detection could be found.

4.5.4 Internal reflections at L-band

Even though L-band might offer some advantages over C-band, it may also introduce some new challenges owing to its deeper penetration. Ketchum and Farmer [99] reported that icebergs were sometimes located at different locations in L-band when compared to X-band in airborne SAR data. This was attributed to internal reflections in the icebergs at L-band, resulting in a time delay in the received radar signal, thus producing a false image down-range of the true iceberg location. These data were later used by Gray and Arsenault [100] to argue that the cause for the time delay was penetration into the icebergs and reflections from the bottom or sidewalls of the icebergs (the ice-water interface). They argue that for greater penetration depths, low absorption, and low scattering losses within the iceberg, reflections from the bottom or the side walls of the iceberg could be dominant, leading to high backscatter returns down-range of the true iceberg locations. This was supported by calculations showing the theoretical attenuation into freshwater ice, and scattering losses due to air bubbles.

4.5.5 Validation

As outlined in Chapter 4.4, validation data are of great importance for testing algorithms that are to be applied in an operational setting, or to historical archive data. In the literature, validation of iceberg detection algorithms has primarily been limited to using incomplete data (such as expert interpretations from SAR images), or a small number of in-situ observations, which risks

introducing bias due to the large variations in backscatter that can be expected from icebergs and their surroundings (see Chapters 4.1 and 4.2).

Studies using a large number of validated iceberg detections have been limited to investigations of icebergs in sea ice to avoid the issues with iceberg drift in open water. However, none of these studies have incorporated seasonal changes in iceberg backscatter such as the influence of temperature on snow and ice.

4.5.6 Detection performance and iceberg sizes

It is to be expected that the visibility of icebergs will decrease with decreasing iceberg size. However, determining the detection performance for different iceberg sizes (see Table 2.1) has only been subject to limited investigations in the past. A study published in 2016 indicated that very few icebergs close to the SAR resolution in size could be detected [96], and although a study published in 2004 showed a high probability of detecting small icebergs embedded in sea ice, this study did not consider the corresponding number of false detections [84]. Determining detection performances for different iceberg sizes would be of great help for the national ice services, but this can only be achieved with high-quality validation data, as determining iceberg sizes from SAR is difficult due to noise and sensor distortions (see Chapter 3).

4.6 Summary

Robust detection of icebergs can only be achieved if there is a sufficient difference in backscatter characteristics between the icebergs and their background. However, iceberg backscatter is highly variable and dependent on many parameters owing to an iceberg's geometry, composition, and temperature, as well as sensor parameters, such as wavelength and incidence angle.

In addition, backscatter characteristics of typical iceberg backgrounds (sea ice and open water), are also highly variable. While for larger icebergs, such as those in the Antarctic, using classification and segmentation methods have proven fruitful, similar approaches to the smaller icebergs in the Arctic are inadequate. Instead, outlier detection algorithms such, as the CFAR approach, are generally adopted.

Although CFAR algorithms are widely used for object detection, they require some manual adjustments depending on the environment, especially for the choice of the PDF used for estimating the backscatter distribution. In addition,

4.6 / SUMMARY

CFAR algorithms have mainly been used for detecting icebergs in open water, while few studies have focused on detecting icebergs in sea ice. One challenge with detecting icebergs in sea ice is the highly variable nature of sea ice backscatter due to different sea ice types and seasonal melting and freezing conditions.

Future L-band SAR missions might offer advantages over C-band, but systematic investigations comparing different sensor types for iceberg detection are lacking. Furthermore, previous studies have suggested that the penetration depth for icebergs at L-band results in internal reflections, causing time delays in the SAR signals. Investigations comparing L- and C-band SAR could help to determine under which conditions L-band is most beneficial.

To perform these investigations, and solve some of the other challenges currently being faced, large datasets of independent validation data would be highly valuable, as they would offer insights into the expected performance and could aid in selecting the optimal detection methods.

5

Overview of Publications

The following chapters summarize journal articles, presentations, and other relevant scientific contributions that have been published as part of this dissertation. The three journal articles presented below are provided in their entirety in Chapters 6-8.

5.1 Paper Summaries

5.1.1 Paper I

Færch, L., Dierking, W., Hughes, N., Doulgeris, A.P., (2023). **A Comparison of CFAR Object Detection Algorithms for Iceberg Identification in L-and C-band SAR Imagery of the Labrador Sea**. The Cryosphere, 17, 5335–5355.

Paper I has two major objectives, 1) a comparison of various CFAR algorithms, and 2) a comparison of C- and L-band SAR for detecting icebergs in open water. The study uses two SAR scenes, one C-band (Sentinel-1) and one L-band (ALOS-2), both acquired over the same region. An optical image (Sentinel-2), also acquired over the same region, is used as a source of independent validation data. The locations of a large number of icebergs (492) were identified in the optical image; however, due to a time difference of several hours between acquisitions, the icebergs were not located at the same positions in the SAR images. To solve this challenge, the location of a large number of the icebergs in the optical image was matched with objects identified in the SAR images, and hence an estimate of drift speed and direction was derived. Then, based on the drift direction and speed, the positions of the remaining icebergs which could not be manually identified in the SAR images were estimated using a linear interpolation. As a result, a large dataset consisting of independently obtained iceberg positions in the SAR images was created. Six different CFAR

detectors were then implemented and applied to the SAR images. Since the SAR images contained both HH and HV polarizations, the CFAR methods took different approaches to combining the polarizations, as described in Chapter 4.3.2. By comparing the outputs of the various CFAR detectors against the validation data at various PFA levels, we could test the performance relative to the PFA level. In addition, using size estimations from the optical image enabled us to characterize the performance at certain PFA levels relative to the iceberg sizes.

The results revealed that most of the detectors can achieve similarly good performance, but that the optimum performance was obtained at different PFA levels (see Figure 5.1). For the C-band image, CFAR methods based on the gamma distribution performed slightly better than the alternative methods, while for the L-band the log-normal CFAR detector performed better than the alternatives. Unsurprisingly, performance improved with increasing iceberg sizes. However, it was found that up to 30% of the medium icebergs were missed despite their being larger than the pixel spacing of the SAR images. This is due to the fact that the radar backscattering is not only influenced by the size of an iceberg, but also by its geometry, composition, and environmental properties, as described in Chapter 2. L-band slightly outperformed C-band; however, some uncertainties in the validation process might have influenced these results.

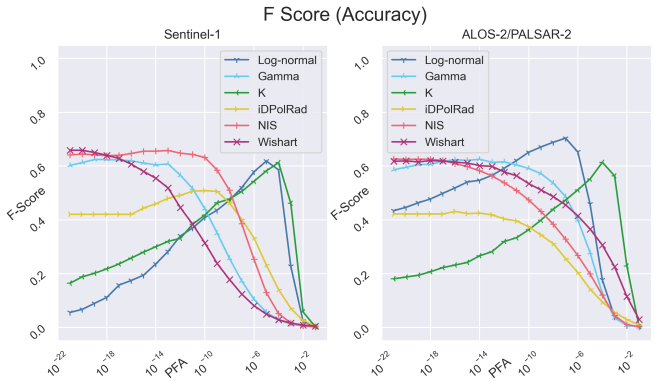

Figure 5.1: Performance of the CFAR algorithms (F1- core) relative to the PFA level. Even though most of the detectors performed similarly, the optimum F1-score is found at different PFA levels, depending on the detector.

Overall, the study offers some novel results and addresses several of the challenges previously described in this thesis, such as the validation of CFAR algorithms outlined in Chapter 4.5.1, and the determination of performance relative to iceberg size as outlined in Chapter 4.5.6. The study also offers the first direct comparison between C- and L-band SAR for iceberg detection (see Chapter 4.5.3), and indicates that time-delayed reflections (see Chapter 4.5.4)

might be an issue for L-band SAR even under melting conditions.

5.1.2 Paper II

Færch, L., Dierking, W., Hughes, N., Doulgeris, A.P., (2024). **Mapping icebergs in sea ice: An analysis of seasonal SAR backscatter at C- and L-band**. Remote Sensing of Environment, 304, 114074.

In paper II, the objective was again to compare C- and L-band SAR for iceberg detection. However, this time the main focus was on regions containing sea ice. The study aims to take a step back and perform a deeper investigation into the contrast between icebergs and their background (sea ice), to obtain new knowledge about the methods most suitable for detecting icebergs in sea ice. To achieve this goal, a dataset consisting of 22 L-band (ALOS-2) and 19 C-band (Sentinel-1) images was acquired over a study area in North-Eastern Greenland covering approximately 23.000 km^2. The images covered two different years, 2019 and 2020, and were all collected between April and July, when the temperatures in the region changed from freezing conditions to the early stages of melting. Both HH and HV polarization were used. Independently obtained iceberg positions and outlines derived using optical satellite images served as validation. Since the region was covered by fast ice during the study period, the sea ice distribution and iceberg locations did not change within the study period. As such, the validation data could be used to extract the backscatter intensity of the single icebergs and adjacent sea ice throughout the entire time series, and the contrast between iceberg and sea ice backscatter could be investigated. A total of 657 icebergs were used for the investigation.

The results revealed that although C-band can offer an appropriate contrast between icebergs and level sea ice under freezing conditions, it fails to offer a contrast between icebergs and deformed sea ice, which means that it is unsuitable for detecting icebergs in areas with ridged and rugged sea ice. This also means that floes of deformed sea ice embedded in level sea ice may be falsely interpreted as icebergs. Additionally, the C-band data cannot be used to separate sea ice and iceberg backscatter under melting conditions. L-band SAR, on the other hand, offered a much higher contrast between sea ice and iceberg backscatter, and although the best contrast was achieved for level sea ice, a practical contrast was still measured for deformed sea ice. In addition, L-band was shown to offer a contrast above 2.5 dB in the summer months for the HV band, proving that L-band is less influenced by melting conditions. The contrast time series for C- and L-band SAR is shown in Figure 5.2. These findings were further confirmed by detecting icebergs using a CFAR detector on two C- and two L-band images, and comparing the output with the validation data. These results also confirmed that L-band is superior to C-band for detecting icebergs

in sea ice, with much higher recall and precision.

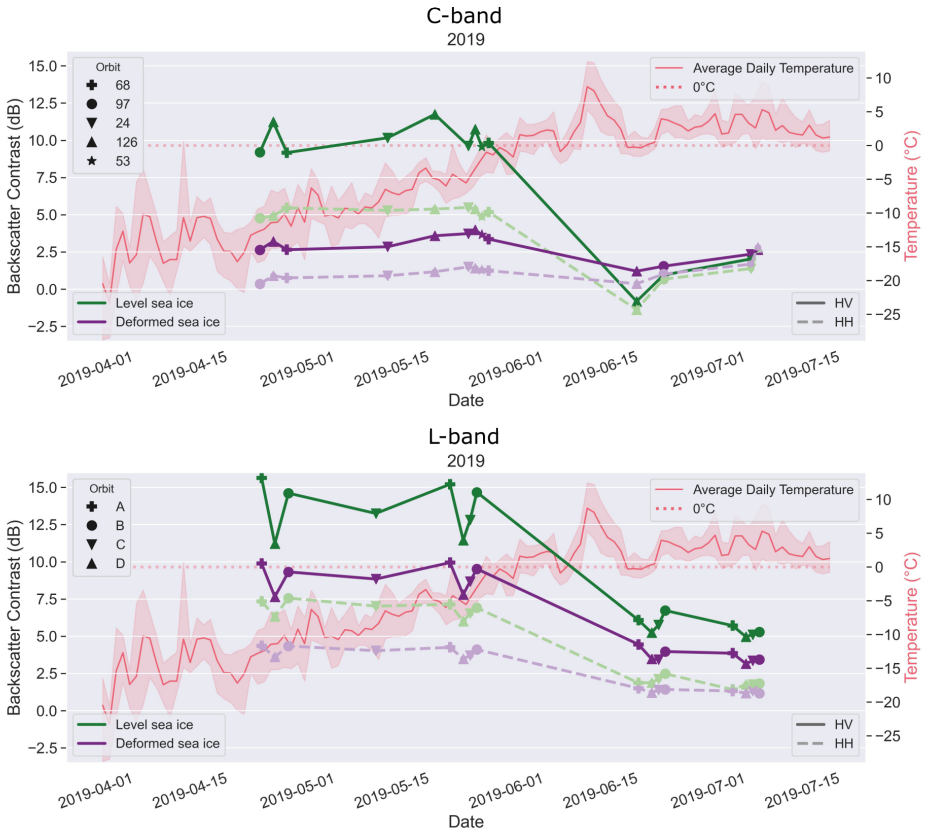

Figure 5.2: Backscatter contrast time-series for C-band (top) and L-band (bottom). The contrast between level sea ice and icebergs (green) and deformed sea ice and icebergs (purple) are plotted for HV (full line) and HH (dashed line). The markers indicate the orbit numbers (see Figure 1 in Paper II). The daily temperature is plotted in the background (red).

The study is the first to compare L- and C-band SAR for detecting icebergs in sea ice, and, is the first to use independently obtained validation data for the investigation of L-band SAR for iceberg detection. The study is also novel in its long time series, presenting new insights into the detectability of icebergs in sea ice under various seasonal conditions (see Chapter 4.5.2). Finally, the study demonstrated how consistent time delays were present in the L-band data of icebergs, which caused a shift in the position of the maximum backscatter intensity that suggested internal reflections (see Chapter 4.5.4), and offered a novel correction to the validation data by explicitly considering these delays. In conclusion, the study provides a major advance in detecting icebergs in sea ice using SAR.

5.1.3 Paper III

Færch, L., Dierking, W., Hughes, N., Doulgeris, A.P., (2024). **Detecting Arctic Icebergs in Sea Ice in L-band SAR Images Using a Multiscale CFAR Algorithm**. IEEE Journal of Selected Topics in Applied Earth Observations and Remote Sensing (submitted).

The objective of this study was to improve the detection of icebergs in sea ice using L-band SAR, specifically in areas with a large variation in iceberg sizes and clusters of icebergs, where conventional, single-scale CFAR approaches might miss icebergs due to fixed window sizes not accommodating the entire range of iceberg sizes. To solve this challenge, the study suggests a simple, multiscale approach to CFAR detection. Here, the multiscale detection performs several CFAR detections on down-sampled versions of the original image. To test the performance, a study area of approximately 3.500 km^2, covering more than 600 icebergs of varying sizes, was selected. We selected eight L-band SAR images (ALOS-2) from over two years, where all the images had a 25-meter pixel spacing, and HH and HV polarization, and varying incidence angles. A CFAR detector based on the K-distribution was used, with detections performed in both polarizations and combined using a Boolean OR operation. The single-scale CFAR detector used a window size accommodating most of the iceberg sizes, while the multiscale CFAR detector used a smaller window size, accommodating small icebergs on the original high-resolution images, and larger icebergs on the down-sampled low-resolution images. To validate the outputs of the CFAR algorithms, time-delay corrections were made to the validation data.

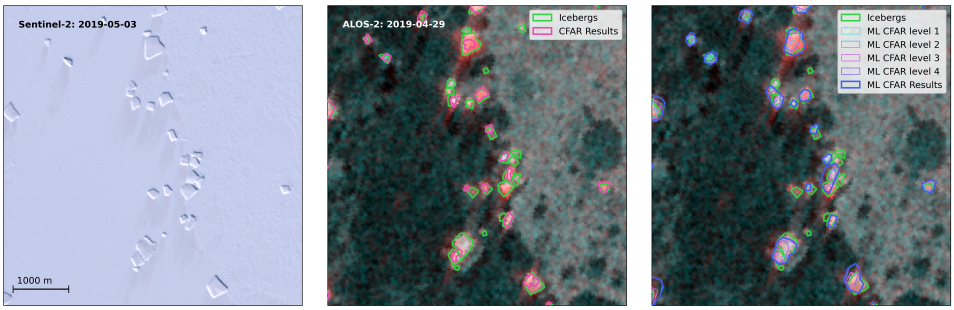

Figure 5.3: Performance of the single-scale CFAR (middle) and multiscale CFAR (right) detector on a subset containing a few very large icebergs, as well as several large and medium icebergs. The Sentinel-2 image is shown as a reference (left). The true iceberg locations after time-delay correction (green) are plotted together with the single-scale CFAR (red) and multiscale CFAR (blue) detections.

The results showed improvements for the multiscale detector relative to the

single-scale detector on all eight images and across all performance scores, with the multiscale approach detecting a higher number of TPs and a lower number of FPs and FNs compared to the single-scale CFAR. The study also investigated the performance relative to iceberg sizes and showed that a large number of medium-sized icebergs were missed, which is significant considering that the pixel spacing of the SAR data was 25 meters. An investigation of the time delay of the iceberg relative to the iceberg size also showed that the average time delay increased with increasing iceberg sizes.

The investigation offers a step forward toward large-scale detection of icebergs in sea ice using L-band SAR. A multiscale approach to CFAR detection could potentially solve some of the challenges related to the fixed window sizes of the CFAR approach (see Chapter 4.5.1). Furthermore, the study demonstrated a relationship between iceberg sizes and the magnitude of the time delays that are noticeable as position shifts of the radar response to an iceberg (see Chapter 4.5.4).

5.2 Additional Scientific Contributions

Code contributions:

- Færch, L., Hietanen, P., (2024). **CFAR Object Detection**, Version 3, GitHub repository, DOI:10.5281/zenodo.11504039, `https://github.com/LaustFaerch/cfar-object-detection`,

Posters and Presentations:

- Færch, L., Kræmer, T., Dierking, W., Doulgeris, A.P., Hughes, N., (2021). **Evaluation of iceberg detection limits from remote sensing data - An investigation around Negribreen**. Online conference on remote sensing in Svalbard, Online, 2021-06-08 - 2021-06-10. (Presentation)

- Færch, L., Dierking, W., Doulgeris, A.P., Hicks, M.R., (2021). **Iceberg Detections at C- and L-band**. International Ice Charting Working Group IICWG-XXII, Online, 2021-09-19 - 2021-09-24. (Presentation)

- Færch, L., Dierking, W., Doulgeris, A.P., (2021). **Iceberg Detections with SAR at C- and L-band**. CIRFA Annual Conference, Sommarøy, Norway, 2021-10-19 - 2021-10-21. (Presentation)

- Færch, L., Dierking, W., Doulgeris, A.P., Hughes, N., (2022). **A Comparison of Backscatter Intensity of Icebergs in C- and L-band SAR Imagery**.

EGU General Assembly, Online, 2022-05-23 - 2022-05-27. (Poster)

- Færch, L., Dierking, W., (2022). **Comparison of CFAR Algorithms for Detection of Icebergs in SAR Imagery**. DRAGON 5 Midterm Results Symposium, Online, 2022-10-17 - 2023-10-21. (Poster)

- Færch, L., Bokhari, R., Zhang, Xi., Dierking, W., (2023). **Dependence of Signature Contrast between Icebergs and Sea Ice on Ice Conditions and Radar Parameters**. DRAGON 5 Symposium, Hohhot, P.R. China, 2023-09-11 - 2023-09-15. (Poster)

- Færch, L., Dierking, W., Hughes, N., Doulgeris, A.P., (2023). **Time-Series Analysis of SAR Backscatter from Icebergs at L- and C-band**. International Symposium on Sea Ice 2023. Bremerhaven, Germany, 2023-07-05 - 2023-07-09. (Poster)

- Færch, L., (2023). **Remote Sensing of Icebergs**. CIRFA Annual Conference, Sommarøy, Norway, 2023-11-28 - 2023-11-30. (Presentation)

- Færch, L., Dierking, W., Hughes, N., Doulgeris, A.P., (2023). **Classification of Icebergs in Land-Fast Ice from L-band SAR using Logistic Regression**. CIRFA Annual Conference, Sommarøy, Norway, 2023-11-28 - 2023-11-30. (Poster)

- Færch, L., Dierking, W., Zhang, Xi., (2024). **Detecting Icebergs in Sea Ice Using L-band SAR**. DRAGON 5 Final Results and DRAGON 6 Kick-off Symposium, Lisbon, Portugal, 2024-06-24 - 2024-06-28. (Poster)

Other Publications:

- Færch, L., Dierking, W., (2022). **Icebergs**. In Dierking, W., Schneider, A., Eltoft, T., Gerland, S., (Eds.), CIRFA Cruise 2022. Cruise report.

/6

Paper I: A Comparison of CFAR Object Detection Algorithms for Iceberg Identification in L-and C-band SAR Imagery of the Labrador Sea

Færch, L., Dierking, W., Hughes, N., and Doulgeris, A. P. The Cryosphere, 17, 5335–5355, https://doi.org/10.5194/tc-17-5335-2023, 2023.

The Cryosphere, 17, 5335–5355, 2023
https://doi.org/10.5194/tc-17-5335-2023

The Cryosphere Open Access EGU

A comparison of constant false alarm rate object detection algorithms for iceberg identification in L- and C-band SAR imagery of the Labrador Sea

Laust Færch[1], **Wolfgang Dierking**[1,2], **Nick Hughes**[3], **and Anthony P. Doulgeris**[1]

[1]Center for Integrated Remote Sensing and Forecasting for Arctic Operations, Department of Physics and Technology, UiT – The Arctic University of Norway, 9019 Tromsø, Norway
[2]Alfred Wegener Institute, Helmholtz Center for Polar and Marine Research, Bussestr. 24, 27570 Bremerhaven, Germany
[3]Norwegian Meteorological Institute, Kirkegårdsvejen, 60, 9293 Tromsø, Norway

Correspondence: Laust Færch (laust.farch@uit.no)

Received: 3 February 2023 – Discussion started: 14 February 2023
Revised: 9 October 2023 – Accepted: 23 October 2023 – Published: 15 December 2023

Abstract. In this study, we pursue two objectives: first, we compare six different "constant false alarm rate" (CFAR) algorithms for iceberg detection in SAR images, and second, we investigate the effect of radar frequency by comparing the detection performance at C- and L-band. The SAR images were acquired over the Labrador Sea under melting conditions. In an overlapping optical Sentinel-2 image, 492 icebergs were identified in the area. They were used for an assessment of the algorithms' capabilities to accurately detect them in the SAR images and for the determination of the number of false alarms and missed detections. By testing the detectors at varying probability of false alarm (PFA) levels, the optimum PFA for each detector was found. Additionally, we considered the effect of iceberg sizes in relation to image resolution. The results showed that the overall highest accuracy was achieved by applying a log-normal CFAR detector to the L-band image (F score of 70.4 %), however, only for a narrow range of PFA values. Three of the tested detectors provided high F scores above 60 % over a wider range of PFA values both at L- and C-band. Low F scores were mainly caused by missed detections of small-sized (<60 m) and medium-sized (60–120 m) icebergs, with approximately 20 %–40 % of the medium icebergs and 85 %–90 % of small icebergs being missed by all detectors. The iDPolRAD detector, which is sensitive to volume scattering, is less suitable under melting conditions.

1 Introduction

Icebergs pose a serious threat to maritime traffic and offshore installations in the Arctic and surrounding regions. As human presence in these areas increases, it becomes more important to develop improved methods for detecting, mapping, tracking, and predicting iceberg occurrences in real time and over large areas.

Traditionally, iceberg detection in the Northwest Atlantic has been conducted visually by observers on aircraft of the International Ice Patrol. However, the increased availability of data from satellite synthetic aperture radar (SAR) sensors in the past decades has promoted a move towards automated detection.

SAR is an active instrument that acquires images independent of sunlight and cloud cover conditions. This makes it the preferred sensor for high-latitude regions, where cloud cover and a lack of daylight can hinder the use of optical images. In a SAR image, the brightness of each pixel depends on the intensity of the signal that is scattered back from the surface – called the backscattering coefficient. Since different objects exhibit different backscatter characteristics, it is possible to identify targets in the SAR image by looking at the backscatter variations. This identification is further aided by the fact that the SAR sensor can transmit and receive radar pulses at different polarizations, giving rise to additional information about the objects.

However, SAR images can be more challenging to analyze compared to optical images for several reasons. Speckle

noise, which occurs due to constructive and destructive interference in the radar signal, can make it difficult to identify small features in SAR images. The side-looking geometry of SAR sensors leads to a decrease of the backscattering coefficients with increasing incidence angle, which is most obvious over homogenous targets. A problem that often arises is how to exactly make a distinction between the backscatter intensity of icebergs and the scattering response of open water or sea ice around them.

Despite these issues, SAR images have been widely used for manual iceberg detection. The identification of icebergs in SAR images typically relies on the fact that icebergs tend to have a higher backscatter intensity than open water and certain types of sea ice (Gill, 2001; Sandven et al., 2007; Wesche and Dierking, 2012). In recent years, the development of automated detection schemes has become more and more important. Icebergs can be automatically detected by using either segmentation (Kim et al., 2011; Tao et al., 2016a; Akbari and Brekke, 2018; Karvonen et al., 2022) or global thresholding approaches (Dierking and Wesche, 2014; Barbat et al., 2019). The most common approach is the application of adaptive thresholding techniques such as the constant false alarm rate (CFAR) detector (Oliver and Quegan, 2004). CFAR detectors are especially valuable for wide-swath SAR images, where large variations in incidence angles make global thresholding techniques difficult to design. Automatic iceberg detection with CFAR has been demonstrated in the past for single-polarization (Power et al., 2001; Gill, 2001) and for dual- and quad-polarization SAR (Howell et al., 2004; Marino et al., 2016, Zakharov et al., 2017). Regional distributions of icebergs have been mapped using this method, e.g., for Greenland (Buus-Hinkler et al., 2014).

SAR images acquired at C-band (4–8 GHz) are typically employed in operational mapping, e.g. from the European Sentinel-1 mission. Sentinel-1 offers a high revisit interval with daily dual-polarization images over most of the Arctic in its extra-wide swath (EW) mode. Through the Copernicus program, Sentinel-1 images are available through a free and open-data policy. The Sentinel-1 mission and its Canadian equivalent, the RADARSAT Constellation Mission (RCM), will continue for at least another decade and will likely be followed by similar missions. C-band SAR is currently being used for iceberg monitoring by, e.g., the International Ice Patrol (IIP) and the Danish Meteorological Institute (DMI).

In 2028, a new L-band (1–2 GHz) SAR mission from ESA, called ROSE-L, is planned to be launched to supplement the C-band Sentinel-1 mission. ROSE-L will also offer regular dual-pol images of the Arctic (Davidson et al., 2021). Already in 2024, NASA and ISRO (Indian Space Research Organization) plan to launch the NISAR (NASA-ISRO synthetic aperture radar) mission with an L-band and an S-band sensor as payload (Das et al., 2021). Although the inclination and left-looking image acquisition of NISAR limits its coverage at 78.5° N, it could still be used for detecting icebergs around Greenland and along the coast of Labrador and Newfoundland. It is anticipated that the L-band data will be a useful complement as the longer wavelengths penetrate deeper into snow and ice, revealing the structures underneath (Dierking and Davidson, 2020), and additionally it is expected that L-band will be less sensitive to sea surface roughness and therefore will offer a higher contrast between icebergs and sea ice, making detection easier.

Only a few studies on using L-band SAR for iceberg observations have been carried out in the past. Gray and Arsenault (1991) showed that icebergs cause time-delayed reflections due to internal scattering in airborne L-band SAR images. Marino (2018) tested an iceberg detection algorithm developed for C-band on L-band images with encouraging results. Recently, a study on scattering mechanisms for icebergs in quad-pol L-band SAR images was conducted by Bailey and Marino (2020), and Bailey et al. (2021) later compared various detectors applied on quad-, dual-, and single-pol L-band SAR images. The studies mentioned above give some indication of the dominant scattering mechanisms and detection capabilities of icebergs at L-band. However, studies comparing C- and L-band for iceberg detection have not been carried out to date, and there is still a need to better understand the benefits and limits of both C- and L-band data and how different detectors perform on the two data types.

A significant challenge in using SAR for iceberg detection is validating the accuracy of detection algorithms. Many studies rely on the information on observed icebergs collected during field campaigns (Willis et al., 1996; Power et al., 2001; Denbina and Collins, 2012) or on visual identification of icebergs in SAR images by experts (Bailey et al., 2021; Marino et al., 2016; Akbari and Brekke, 2018). Both approaches have limitations. Using field observations of icebergs results in a spatially limited validation dataset, while expert interpretation of SAR images does not account for icebergs that may be present but not visible in the SAR image due to resolution or noise issues. Images from optical remote sensing satellites offer an independent source of validation data but are limited to days with reduced cloud cover. Another requirement is that optical and SAR images must be acquired within a small time gap between them to avoid icebergs having drifted over long distances between acquisitions.

In this study, we compare six different CFAR detection algorithms and apply them on an overlapping C- and L-band image pair to study the effect of the frequency and tuning of the algorithms on the detection accuracy. To ensure an accurate comparison, we created a validation dataset using an optical Sentinel-2 image, in which we manually accounted for the iceberg drift occurring between the image acquisitions. The detectors were then assessed not only on their ability to accurately detect the verified icebergs but also on the number of false detections they produced. The novelty of this work is the consistent comparison between L- and C-band SAR for iceberg detection. Additionally, by using Sentinel-2 data as validation, it was possible to test the detection accuracy

as a function of iceberg size. Finally, one of the tested detection algorithms was based on the Wishart likelihood ratio test, which has not been applied before for iceberg detection.

The structure of the paper is as follows. In Sect. 2, a short introduction to CFAR algorithms for iceberg detection is provided, followed by Sect. 3, which presents the data used, explains the method used for creating validation data, and outlines the implementation details of the iceberg detection algorithms that we have tested. The paper proceeds with our results in Sect. 4 and a discussion in Sect. 5. The paper ends with a conclusion in Sect. 6.

2 Theory

The SAR backscatter intensity from an iceberg mainly arises from surface- and volume-scattering (Power et al, 2001; Bailey and Marino, 2020). These two scattering mechanisms are influenced by several different parameters; some are target-dependent such as iceberg geometry, temperature, surface roughness, and structure (e.g., the presence of snow, firn, or saline layers). Others are sensor-dependent such as incidence angle, frequency, and polarization. Additionally, sensor limitations such as resolution and the presence of speckle noise further complicate image interpretations, as backscattering returns from icebergs, which mostly cover only a few pixels, might be indistinguishable from intensity variations of speckle. For operational applications, single- or dual-pol are commonly used, but if quad-pol data are available, polarimetric decomposition can be applied to aid image interpretation (Dierking and Wesche, 2014; Zakharov et al., 2017; Bailey et al., 2021).

It has been observed that icebergs covered by liquid water or wet snow stand out as dark objects against a lighter background of open water. However, in most cases, icebergs exhibit higher backscatter intensities than open water (Power et al., 2001; Wesche and Dierking, 2012). Icebergs are hence typically visible in SAR images as bright spots compared to the relatively darker ocean. Since the backscatter of open water can be highly variable due to its dependence on local wind conditions and incidence angle, global thresholding techniques are insufficient to detect icebergs. Instead, adaptive methods utilizing the local contrast in backscatter between neighboring pixels are normally employed to distinguish between icebergs and open water.

2.1 CFAR iceberg detection

A CFAR detector is a type of adaptive thresholding algorithm used to identify objects such as ships or icebergs in SAR images. The algorithm compares the intensity of each pixel under test (PuT) to the local background clutter, and if the pixel value exceeds a certain threshold, it is marked as an outlier. Clusters of these outliers are assumed to represent objects of interest. The threshold is determined based on the probability density function (PDF) of the local clutter, allowing the CFAR detector to adapt to variations in the background noise (Crisp, 2004).

Accurate CFAR detection thus relies on accurate modeling of the background clutter PDF in SAR images, which is not an easy task. In practice, a handful of models are widely used to estimate sea surface clutter, but their performance depends on the actual clutter properties, which depend on radar parameters such as frequency. A model that works very well on C-band might prove inferior on L-band.

The K distribution is a PDF that has been widely used to model sea surface clutter (Oliver and Quegan, 2004), and CFAR algorithms based on the K distribution have been used for ship and iceberg detection (Power et al., 2001; Brekke and Anfinsen, 2011; Wesche and Dierking, 2012; Liu, 2018). But due to the complexity of the K distribution, models based on simpler PDFs are also commonly used, e.g., the log-normal distribution (Crisp, 2004; El-Darymli et al., 2013) and gamma distribution (Gill, 2001; Crisp, 2004; Buus-Hinkler et al., 2014; Tao et al., 2016b).

If the background clutter is accurately modeled, a threshold can be set in such a way that the probability of falsely triggering the detector – the probability of false alarm (PFA) – is maintained at a constant level. However, in practice, there can be discrepancies between the theoretical PFA and the actual false alarm rate due to various implementation details. If the window over which the clutter parameters are estimated is too small, it will likely cause the calculated PDF parameters to be biased. If the window is too large, it is more likely to cover nonhomogeneous clutter regions or capture neighboring icebergs, which will contaminate the parameter estimation (Tao et al, 2016b). Additionally, CFAR algorithms used for operational detections are often optimized to minimize the computational complexity, which can further degrade the performance. When testing CFAR algorithms for operational monitoring, it is therefore of high importance to inform about the true number of false alarms, e.g., by testing the detector for an area without icebergs.

2.1.1 Merging of multiple bands

Most models used for estimating the clutter are based on single-channel statistics. For multi-channel data, i.e., the case where several polarizations are available, three distinct detection strategies can be used (Crisp, 2004). (1) The individual channels can be combined into a new single channel, which is then fed to a single-channel detector. This could be achieved by calculating the SPAN (or total power) or by making a new channel consisting of a sum of normalized intensities (Liu, 2015). But channel combinations can also be developed to enhance the contrast between background and target before applying the detector, e.g., by utilizing the polarimetric properties of the target which one wants to detect. One such example is the intensity dual-pol ratio anomaly detector (iDPolRAD) suggested for iceberg detection (Marino et al., 2016).

(2) Multi-dimensional detectors based on multivariate PDFs can be applied directly to find outliers based on all channels simultaneously. (3) The far most common approach is simply to apply a single-channel detector to each channel and then combine the outputs of the resulting detections using Boolean operations.

When merging the output from multiple single-band CFAR detectors into a new channel, it needs to be considered that the PFA of the combined channel will not be the same as the PFA used on the individual bands. If we combine the output from two CFAR filters using a Boolean AND operation, the final product will contain fewer outliers than the number of outliers found by the individual detectors. Similarly, a Boolean OR operation will result in more outliers.

For determination of the combined PFA, the multiplication and addition rules for probabilities can be used.

If we have two detectors, e.g., one applied to the HH polarization and another to the HV polarization, and assuming that the noise in the HH and HV channel is independent, then the PFA after a Boolean AND operation becomes

$$\mathrm{PFA\,(HH\ and\ HV)} = \mathrm{PFA\,(HH)\,PFA\,(HV)}\,.$$

If the PFA for the HH and HV channels are equal, we can calculate the PFA needed on the individual channels based on the desired combined PFA as

$$\mathrm{PFA\,(HH)} = \mathrm{PFA\,(HV)} = \sqrt{\mathrm{PFA(HH\ and\ HV)}}.$$

Similarly, we can calculate the corrected PFA if we are using a Boolean OR operation as

$$\begin{aligned}\mathrm{PFA\,(HH\ or\ HV)} &= \mathrm{PFA\,(HH)} + \mathrm{PFA\,(HV)} - \mathrm{PFA\,(HH)\,PFA(HV)} \\ \Rightarrow \mathrm{PFA\,(HH)} &= \mathrm{PFA\,(HV)} = 1 \pm \sqrt{1 - \mathrm{PFA(HH\ or\ HV)}}\end{aligned}\quad,$$

choosing the smallest positive solution, which is also known as the Šidák correction (Salkind, 2007).

This means that if we want a PFA of 10^{-6} after combining two detectors using an AND operation, the CFAR detectors applied to the individual channels need to be adapted by applying a PFA of $\sqrt{10^{-6}} = 10^{-3}$. Similarly, if combining using a OR operation, we need an individual PFA of $1 - \sqrt{1 - 10^{-6}} \approx 0.5 \times 10^{-6}$.

3 Data and method

3.1 Data description

For this study, we selected a test area covering part of the Labrador Sea because of the high density of icebergs in open water and along the coast. This area is also of great interest for operational iceberg charting and is regularly monitored by the International Ice Patrol (Dierking, 2020). An L-band SAR image was acquired by the PALSAR-2 sensor on board the ALOS-2 satellite. Overlapping Sentinel-1 C-band SAR, and Sentinel-2 optical images were found and downloaded through the CREOtech Data and Information Access Service (CREODIAS). All three images partially overlapped and were acquired on the same day within a few hours (Fig. 1). The ALOS-2 image was delivered in a pre-processed wide beam mode and consisted of dual-polarization HH and HV intensity channels. The Sentinel-1 image was acquired in extra-wide swath mode (EW) and contained dual-polarization HH and HV intensity channels. The Sentinel-1 image was pre-processed using the Sentinel Applications Platform (SNAP)[1]. Both SAR images were acquired from similar look geometries, both at a descending orbit and right looking. The optical Sentinel-2 image was downloaded in level-1C format.

Visual inspection of the Sentinel-2 image revealed hundreds of white objects floating in the open water and along the coast. Although sea ice was spotted in the area 2 weeks prior to the acquisition of the data used in this study, we expect that most of the objects in the area are icebergs, since single sea ice floes generally tend to disintegrate faster in open water than icebergs due to their smaller thickness

An overview of the data is shown in Table 1. Originally, the ALOS-2 image was acquired at a 25 m pixel spacing, but for the comparison between C- and L-band both SAR images were resampled to a local polar stereographic coordinate system with a 40 m pixel spacing. The resampling was carried out using a nearest-neighbor interpolation to avoid averaging pixel intensities. However, the SAR images did still have a different equivalent number of looks (ENL), which should be considered in the comparison.

Meteorological data from two nearby weather stations were downloaded from the Meteorological Service of Canada (Government of Canada, 2023). At both weather stations the data showed temperatures between 6–15 °C, and wind levels between 1–5 $\mathrm{m\,s^{-1}}$ during the day the images were acquired. The weather stations are also shown in Fig. 1.

A land mask was created from OpenStreetMap land polygons (OpenStreetMap contributors, 2015). A buffer of 500 m was added to the mask to avoid any issues with SAR layover or bad geocoding.

3.2 CFAR detectors

Six different CFAR detectors were implemented and tested for this study. Since we are working on dual-pol data, the final detection needs to include the combination of the HH and HV channels. The selected detectors cover all three detection strategies outlined in Sect. 2. Three detectors were based on combining results from single channels using Boolean logic (method 3), namely the log-normal, gamma, and K detectors. Another two detectors were based on transforming the dual-pol data into a single channel which is better suited for object detection (method 1). These were the normalized in-

[1]The processing steps were orbit file application, grd-border-noise removal, thermal noise removal, calibration, and ellipsoid correction to 40 m pixel spacing.

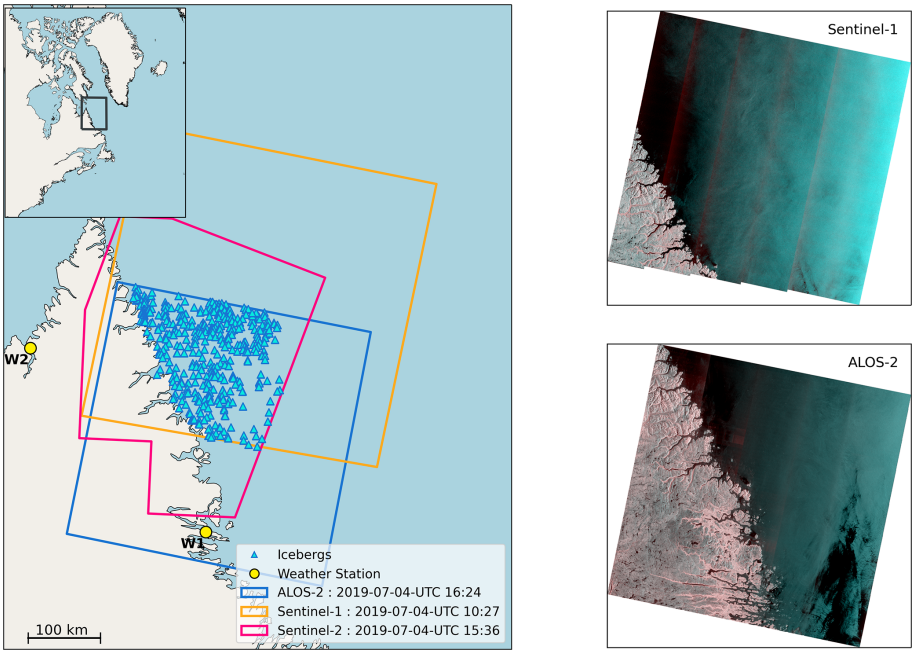

Figure 1. Overview of the area of interest and data used for the study. The outlines of the optical (red) and SAR (blue and orange) are shown together with the location of the icebergs in the optical image (blue triangles). Meteorological data were downloaded from the weather stations at Nain Airport (W1) and Kangiqsualujjuaq Airport (W2). The Sentinel-1 and ALOS-2 images are shown to the right. The SAR images are color-coded: red – HV, green – HH, and blue – HH.

Table 1. Overview of the data used in the study. n/a – not applicable.

Sensor	Format	Acquisition date/time	Tile(s)/orbit identifier	Pixel spacing	Bands	ENL
Sentinel-2	L1C	4 July 2019 15:36:39	T20VNJ/R068 T20VNL/R068 T20VPJ/R068 T20VPK/R068 T20VPL/R068	10 m	B2, B3, B4, B8	n/a
Sentinel-1	EW GRDH	4 July 2019 10:27:30	–/028068	40 m	HH, HV	10.7[a]
ALOS-2	WBDR	4 July 2019 16:24:43	–/–	25 m	HH, HV	15[b]

[a] Sentinel-1 Product Definition (Bourbigot et al., 2016). [b] ALOS-2 Product Format Description (JAXA, 2012).

tensity sum (NIS) and the iDPolRAD. Finally, a multidimensional detector (method 2) based on the likelihood ratio test statistic in the Wishart distribution was tested as well.

3.2.1 Log-normal CFAR

The first and most simple detector used was the log-normal detector (Crisp, 2004; El-Darymli et al., 2013). In the log-normal CFAR detector, it is assumed that the logarithmic transformation from intensity to decibel, normally used for visualizing SAR images, leads to near-Gaussian background clutter. If this is valid, outliers can be detected by employing simple Gaussian statistics, i.e., by comparing the PuT against the average plus some multitude, k, of the standard deviation of the background backscatter.

3.2.2 Gamma CFAR

The gamma detector is based on the fact that, under fully developed speckle, the multi-looked background clutter intensity follows a gamma distribution (Oliver and Quegan, 2004; Argenti et al., 2013). Here, the threshold for determining outliers can then be found from the average clutter intensity and the number of looks, L, which is known.

3.2.3 *K* CFAR

The gamma model only accounts for variation due to speckle, but in real SAR images, it has been observed that the clutter often exhibits variations in the backscatter in addition to the speckle. These variations, called texture, are attributed to spatial variation of intensity within the area of interest (Oliver and Quegan, 2004; Anfinsen et al., 2009; Doulgeris et al., 2011) and can in some cases falsely trigger a CFAR detector, thus leading to a higher false alarm rate. To account for this total speckle variation, clutter models incorporating both speckle and texture have been suggested in the past. The most well-known of these models is the K distribution. Here, the PDF of the single-band L-looked intensity signal, I, can be modeled using the mean intensity, μ, the shape parameter (number of looks), L, and the order parameter, ν. The disadvantage of this PDF, which is a combination of the gamma function, $\Gamma(z)$, and the Bessel function of the second kind, $K_n(x)$, is that it does not have any closed-form solution. Therefore, a complex numerical integration must be executed to calculate the appropriate threshold.

3.2.4 NIS CFAR

The theory behind the normalized intensity sum (NIS) detector is closely related to the principle of the polarimetric whitening filter (PWF) (Novak and Hesse, 1993; Lee and Pottier, 2009). In its original application, the PWF creates a new channel such that the standard deviation to mean ratio is minimized. In the case of dual-polarization intensity data, this new channel can be calculated as a sum of normalized intensities (Liu, 2015) and is therefore referred to as NIS. If we assume that the individual channels, HH, and HV, follow a gamma distribution, the new channel, w, should also follow a gamma distribution. As such, the CFAR detection for the NIS can be carried out by feeding it into a gamma detector. The method was initially developed for ship detection but has also been tested for iceberg detection (Denbina and Collins, 2014; Bailey et al., 2021).

3.2.5 iDPolRAD CFAR

The iDPolRAD was suggested by Marino et al. (2016) specifically for detecting icebergs in sea ice. The detector is based on the observation that icebergs often exhibit a higher cross-polarization and depolarization ratio (cross- over co-polarization) than thin sea ice and open water. This observation is attributed to the fact that radar signals have a larger penetration depth into icebergs than into sea ice and open water, which leads to volume scattering and multiple reflections from within the iceberg volume. This was utilized by designing a detector that is sensitive to pixels with higher cross-polarization and depolarization ratio than their background. Specifically, the algorithm merges the co- and cross-pol channels into a new quantity that enhances the contrast of pixels with a high volume scattering relative to their background. Icebergs can then be detected in this new quantity, by either employing a global threshold or applying a CFAR detector that is tuned to the PDF of the new quantity.

3.2.6 Wishart CFAR

The idea behind the Wishart detector is that, under fully developed speckle (Anfinsen et al., 2009; Argenti et al., 2013), the complex amplitude signal of the backscatter follows a circular zero-mean Gaussian distribution, which leads to the complex polarimetric covariance matrix being Wishart distributed (Goodman, 1963; Conradsen et al., 2003). A test of equality of two complex distributed covariance matrices was suggested by Conradsen et al. (2003) for change detection applications. A CFAR-like detector for edge detection using this test statistic was used in Schou et al. (2003). There, two blocks of equal size, separated by a spatial gap, were used to detect edges in different orientations. This was done by calculating the average covariance matrix for each rectangle and then combining these two covariance matrices into a new channel Q, which denotes the likelihood ratio test statistic. An approximate distribution for Q is known, which can be used to calculate a threshold that corresponds to a specific false alarm rate. The advantages are that this threshold only depends on the block size and the dimensionality of the covariance matrix (number of polarizations). Hence, the threshold only needs to be calculated once per image, which is equivalent to applying a global threshold to the entire Q image. This theory can easily be extended to object detection applications, where a single multi-looked PuT is tested against a larger background. The method is developed for complex data where knowledge on the full covariance matrix is required. But with minor changes the method also works for intensity data (the block diagonal case in Conradsen et al., 2003, and Schou et al., 2003), which will be used for this study.

The main strength of the Wishart detector is that it is multidimensional and can be extended to quad-pol data, without changing the mathematics behind the implementation. Although a contrast enhancement technique based on the test statistic was recently used for highlighting targets with reflection symmetry, suggesting that the method could be used for ship detection (Connetable et al., 2022), this detector has not been used for iceberg detection until now.

3.3 CFAR implementation details

All CFAR detectors were implemented using Python 3.8 with the NumPy and Numba libraries (Harris et al., 2020; Lam et al., 2015). Additionally, the SciPy library was used for calculating the statistical parameters needed for the probability density functions (Virtanen et al., 2020). Input and output operations were implemented using the Rasterio library (Gillies et al., 2013).

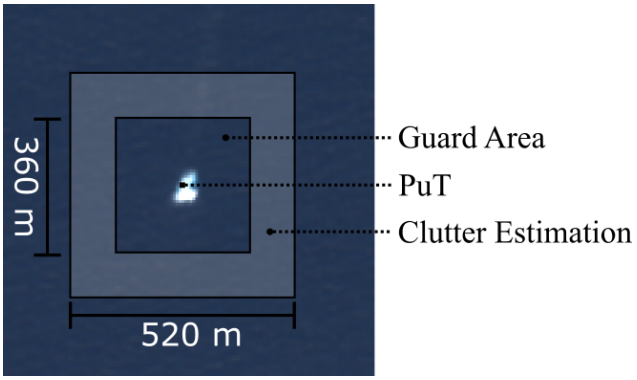

Figure 2. CFAR sliding window configuration overlaid on the Sentinel-2 image.

For the log-normal, gamma, and K detector, the detectors were applied to the HH and HV channels individually. The final outliers are then found by combining the outliers from the two channels using a Boolean AND operation. The AND operation was selected to minimize false detections due to single-channel noise, e.g., in the form of speckle. Except for the iDPolRAD detector, the other detectors were implemented using the window design shown in Fig. 2. Here, a guard area of 360 m ensures that icebergs shorter than 180 m will always be excluded from the clutter estimation window regardless of orientation. The window sizes were based on the inspection of the Sentinel-2 image, in which 97 % of the icebergs are shorter than 180 m. Icebergs that are longer than 180 m but shorter than 360 m will only partly contaminate the clutter estimation, e.g., when the center of the window is located at the iceberg edges. For sizes $\geq$ 360 m we found only one iceberg in the Sentinel-2 image. The size of the outer window of 520 m was selected as a trade-off between having a high number of samples for parameter estimation while avoiding capturing neighboring icebergs in the background estimation.

The iDPolRAD detector was implemented using a test and a training window of 3×3 and 57×57 pixels respectively. These window sizes were chosen based on the suggestions by Marino et al. (2016) and Soldal et al. (2019). In the original paper (Marino et al., 2016), icebergs are detected using a Gaussian-based CFAR detector with an empirically set threshold, since no analytical expression of the PDF exists for the iDPolRAD transformation. However, this approach is unsatisfactory for the comparison of different detectors in this study. Instead, we have opted on using a method similar to Soldal et al. (2020). Here, a generalized gamma function proved to be a good fit for the distribution. But since it is computationally very expensive to estimate the parameters for this distribution locally, we decided to fit the generalized gamma distribution to the iDPolRAD image globally. To avoid skewing the distribution, land was masked, and pixels where the iDPolRAD was smaller than 0 and larger than 50 times the mean were excluded for the parameter estimation. Our approach enables us to test the performance of the iDPolRAD detector at varying global thresholds, avoiding computation times that are too long.

Also, the K detector is computationally expensive when estimating the threshold locally. This is normally solved by using approximations of the original PDF (Oliver and Quegan, 2004; Tunaley, 2010) or by estimating the order parameters regionally on larger image tiles (Liu, 2018). To shorten the computation time for the K detector, we used precomputed look-up tables for the threshold (Brekke, 2009). Threshold values corresponding to the desired PFA level and the ENL of the image were calculated for 40 different values of the order parameter ν on a linear interval between 1 and 20, corresponding to the observed range of ν for our data. For values of ν larger than 20, the threshold does not change significantly, since large ν values correspond with low texture. The order parameter ν could be calculated locally for each pixel using the clutter estimation window above, using the method of moments (MoM) as suggested by Wesche and Dierking (2012). Based on this order parameter a suitable threshold was selected from the look-up table for each PuT.

The NIS transformation was calculated by using the window in Fig. 2. Here the PuT intensities of the two channels were normalized using the average of the clutter window and then added yielding the normalized intensity sum. A gamma CFAR detector was then applied to detect outliers in the NIS channel. The gamma CFAR requires an estimate of the ENL, which has changed after the transformation. The new ENL was estimated from the mean-squared-over-variance ratio. To avoid skewing the estimation of the ENL due to the presence of outliers, pixels with a NIS above 2 times the median NIS were excluded.

The Wishart detector was implemented according to Schou et al. (2003) using the window configuration shown in Fig. 2. Here, the covariance matrix of the PuT was compared with the average covariance matrix of the background clutter. Since the Wishart detector is based on a two-sided test statistic, the CFAR filter will highlight both bright and dark features. However, for this study we are only interested in bright outliers, since we only found icebergs with bright radar returns, so outliers that are darker than the mean of the clutter window were removed.

Each of the 6 detectors was applied to the images 21 times, corresponding to 21 different PFA levels varying from 1×10^{-21} to 1×10^{-1} on both the Sentinel-1 and ALOS-2 image. Due to issues with numerical stability of the detectors, it was not possible to test the filters at PFA levels smaller than 1×10^{-21}. The land mask mentioned earlier was applied to the SAR images before CFAR detection to avoid false detections due to land. To limit the noise in the detections, identified objects covering only a single pixel were removed from the results. Similarly, objects covering more than 500 pixels were also removed from the dataset, since no objects near that size were observed in the Sentinel-2 image, and hence it

Table 2. Classification of icebergs in the area of interest.

Iceberg type	Number of icebergs
Small (<60 m)	181
Medium (60–120 m)	175
Large (>120 m)	136

was assumed that outliers of that size were likely caused by errors in the processing.

The code for the CFAR detectors has been made available on GitHub to allow testing on other SAR images by fellow researchers (Færch, 2023).

3.4 Validation data

In the Sentinel-2 image icebergs were identified by applying an N-Sigma CFAR detector to the sum of the high-resolution bands: B2, B3, B4, and B8. Pixels brighter than the mean background plus 4 times the standard deviations were marked as possible icebergs. The results were then manually checked to remove artifacts from clouds and land, and a few icebergs missed by the automatic detection were added. A total of 492 icebergs were detected in the area of interest (AOI) in the optical image. The sizes of the icebergs were then extracted from the Sentinel-2 image, and the icebergs were classified according to length (Table 2) using the WMO nomenclature (Dierking, 2020), with the length being the major axis of the icebergs. The average iceberg length was 84 m, and 97 % of the icebergs were shorter than 180 m.

Since the optical and the SAR images were acquired at different times, the locations of the icebergs change between the images because ocean currents and wind cause the icebergs to drift between acquisitions. To correct for this drift, icebergs observed in the Sentinel-2 image were manually matched to objects in the SAR images. This matching was carried out in the geographic information system (GIS) application QGIS 3.10.13, and the process was aided by the fact that, on a large scale, icebergs arranged in clusters often drift in similar directions and over a similar distance. Hence, looking at the overall patterns of iceberg clusters across the different images helps determine the drift of individual icebergs. Using this approach, it was possible to create verified drift paths for 336 of the icebergs in the ALOS-2 image and 270 of the icebergs in the Sentinel-1 image. The reason why fewer icebergs could be manually matched between the Sentinel-1 and Sentinel-2 image was the larger time difference of approximately 5 h between their acquisitions, compared to only around 1 h difference between the ALOS-2 and Sentinel-2 image. Additionally, a higher noise level of the Sentinel-1 image made matching more difficult, especially for smaller icebergs. The average drift distance was 489 m between the ALOS-2 and Sentinel-2 acquisitions and 3953 m between the Sentinel-2 and Sentinel-1 acquisitions. Most of the icebergs that could not be matched with high confidence between the SAR images and the optical image, were very small and hence very difficult to visually identify in the SAR images because of their lower resolution and the presence of speckle noise. A linear interpolation method was used to predict the expected drift paths of these icebergs (Fig. 3). This linear interpolation method was tested on a subset of the dataset (10 %) and shown to give an average distance error of 335 m for ALOS-2 and 1789 m for Sentinel-1.

A few bright objects in the SAR images that were covered by clouds in the optical data were masked out from the SAR images to avoid counting these as false detections. Similarly, icebergs drifting into the AOI from outside were removed manually from the analysis. Additionally, a single bright object visible in both the ALOS-2 and Sentinel-1 image was interpreted as a ship and removed from the analysis. The object resembling a ship was also recognized in the Sentinel-2 image, but an independent automatic identification system confirming this observation could not be found.

Both the verified and expected drift paths were used to validate automatic detections in the SAR images. Objects detected by the CFAR algorithms within a search radius of the expected or verified locations of icebergs were marked as true positives (TPs). This search radius was set to 250 m for the verified drift paths. For the interpolated expected drift paths, the search radius was set equal to the average distance error in the interpolation method: 335 m in the ALOS-2 image and 1789 m in the Sentinel-1 image. If several objects were detected within the search radius, only the nearest object is counted as a true positive, and the rest is interpreted as false positives. If no objects are detected in the search area, it was marked as a false negative (FN). Objects that were not within the search radius of any icebergs were marked as false positives (FPs).

3.5 Post-processing

Three different performance measures were used to check the performance of the different detectors. These were recall, precision, and F score defined as

$$\text{Recall} = \frac{\text{TP}}{\text{TP} + \text{FN}}$$

$$\text{Precision} = \frac{\text{TP}}{\text{TP} + \text{FP}}$$

$$F\ \text{score} = 2\frac{\text{precision} \cdot \text{recall}}{\text{precision} + \text{recall}}.$$

As such, recall accounts for the probability of detecting the validated icebergs, i.e., how many of the icebergs have been detected. Precision is used to assess the probability of a detected object being an iceberg. As the PFA level is increasing, each detector is more likely to detect the verified icebergs but also more likely to make false detections. The overall performance of the detectors is thus a trade-off between these two scores. For marine safety, for example, a missed detection is

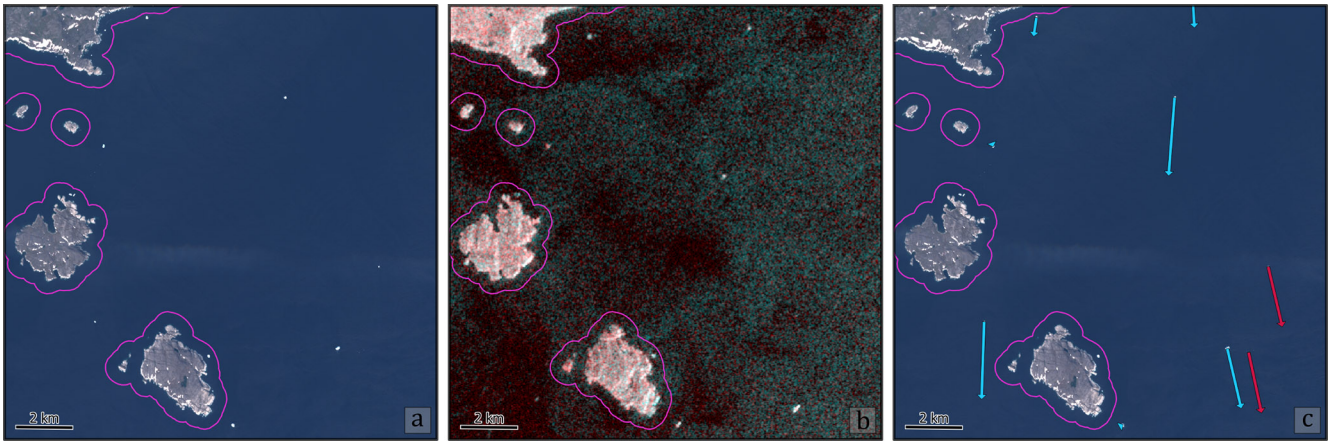

Figure 3. Subset of the AOI showing the matching between the optical and SAR data. Purple outline indicates areas removed by the land mask. Several icebergs are visible in the Sentinel-2 RGB image **(a)**. These icebergs have drifted since the Sentinel-1 image was acquired **(b)**. Verified drift paths (light blue) were manually created for icebergs that could be confidently identified in the SAR imagery. Expected drift paths (dark red) were then created using linear interpolation the remaining icebergs **(c)**.

more critical than a false detection. For evaluating the overall performance of the detectors, we decided to evaluate missed and false detections equally by using the F score.

4 Results

Recall and precision as a function of increasing PFA levels are plotted in Figs. 4 and 5. For most of the detectors, the shape of the recall function can be divided into two phases. For small and intermediate PFA levels, the recall is either constant or increasing steadily with increasing PFA. For larger PFA levels, the recall increases more rapidly. The first phase can be explained by the detection of a few new icebergs for each lower threshold level, while in the second phase, the rapid increase is likely triggered by speckle or noise within our search radius. We will discuss this issue more in detail in Sect. 5.2.

Comparing the recall for the two sensors, we found that all six detectors behave very similarly when applied to the L- and C-band images for low PFA levels, with the exception being the log-normal detector, which show a higher recall for the L-band image. At higher PFA levels the recall for Sentinel-1 increases earlier and more strongly compared to ALOS-2. For a PFA level of 0.1, all detectors in the Sentinel-1 image detect 97 %–99 % of the icebergs, compared to only 79 %–97 % for ALOS-2 (but note that the probability of false detections is very high; see Fig. 5). The NIS, Wishart, and gamma detectors give the highest recall for both L- and C-band, whereas K and log-normal detectors generally show a poor recall for low to medium PFA levels.

Our results for the precision shown in Fig. 5 reveal that most of the detectors have a constant or slightly decreasing precision for small PFA levels. This trend is caused by a small increase in the number of false positives for each lower threshold level. With increasing PFA levels, the precision reaches a point where it starts to rapidly decrease towards zero, corresponding with a large increase in the number of false positives coupled with only a small increase in true positives. When the threshold becomes very low, intensity variations due to speckle will start triggering the detector, causing an increased number of false positives, which leads to a rapid decrease of precision. When comparing the two sensors we found a very similar performance for the gamma, log-normal, and K detectors for C- and L-band. Especially the log-normal and K detectors show a very high precision over a wide range of smaller PFA values. This high precision at low PFA levels is mainly driven by the fact that these detectors only detect a small number of large and bright icebergs, with almost zero false positives. However, this also means that these detectors have a high number of false negatives, which is also evident when comparing the precision (Fig. 4) with the recall (Fig. 5). The Wishart, NIS, and iDPolRAD all show lower precision at L-band compared to C-band, suggesting noise in the L-band image is triggering these detectors. Especially the iDPolRAD detector shows a very large decrease in precision. This indicates that in our dataset, more spots of strong backscattering in HV not caused by icebergs occur at L-band than at C-band.

In general, high recall comes with low precision. This makes sense, as there is an overlap between the intensity backscatter distributions for open water and icebergs, and a detector that captures more icebergs will therefore likewise capture more spots of strong backscattering from the water surface as well. The exception here is the iDPolRAD filter, which for ALOS-2 shows very low precision, which suggests that this detector is triggered more often by noise than the other detectors.

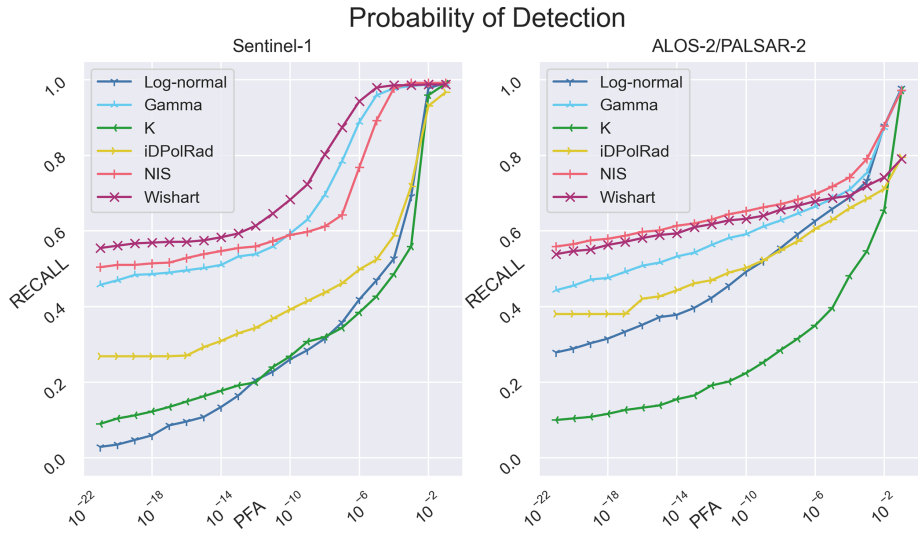

Figure 4. Recall – the probability of detecting the icebergs.

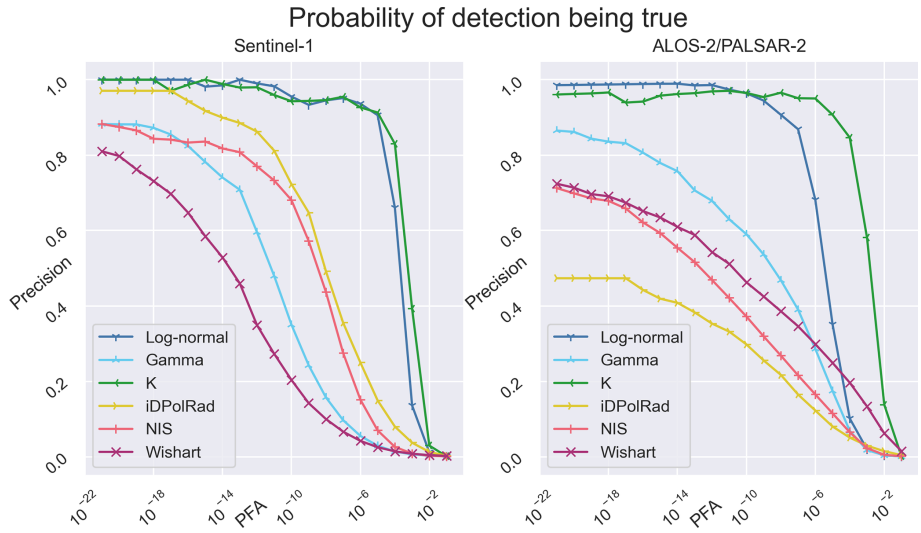

Figure 5. Precision – the probability of a detection being an iceberg.

The F score shown in Fig. 6 combines recall and precision, which makes an overall assessment of the different detectors much easier. In general, most of the detectors show poor F scores for very small PFA levels due to low recall and for high PFA levels due to low precision. Between those extremes the F score is at maximum, corresponding to a region where we obtain the optimum balance between missed and false detections. However, the exact point of this optimum PFA level is very different for the different detectors and varies also between C- and L-band. The large differences in the optimal PFA level for a given detector highlight the importance of determining recall and precision at different PFA levels.

Overall, the performance of iceberg detection accuracy of Sentinel-1 and ALOS-2 is comparable, with each sensor obtaining maximum F scores of around 60 %–70 % for all detectors except for the iDPolRAD, which generally scores lower. This issue is discussed in Sect. 5.

The K detector and the log-normal detector achieve their maximum accuracy at a very narrow interval of PFA levels, whereas the gamma, iDPolRAD, NIS, and Wishart generally exhibit higher F score across a wide range of PFA levels. The comparisons between the shapes of the F score as a function of PFA reveal that there is no single detector achieving best performance over the whole range of PFAs. Results obtained at C- and L-band show that one detector may be optimal at one frequency but another detector for the other frequency. For some filters it is better to select a lower value of PFA; for others a higher value leads to higher F scores. Nevertheless, Figs. 4, 5, and 6 are helpful in deciding which detector

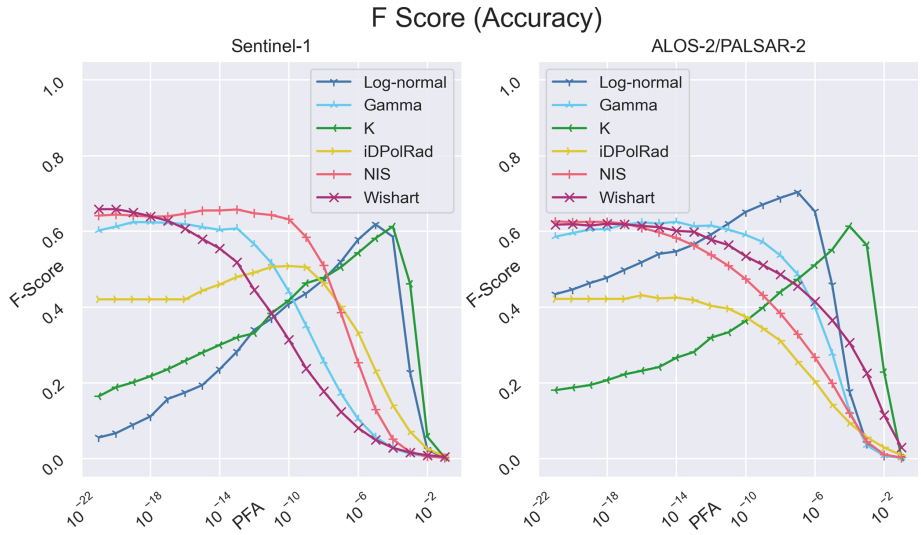

Figure 6. F score – the overall accuracy of the different detectors as a function of the PFA.

to use for a given PFA and radar band. Below, we include additional criteria that should be considered in the selection of a specific filter. It must be admitted, however, that the accuracy of detection is still too low for an unsupervised mapping of iceberg positions to be used for navigation. Further experiments with different modes of SAR images and combinations of images acquired simultaneously at different radar frequencies are required.

For each of the detectors, results from the optimal configuration, i.e., the PFA level that resulted in the highest F score, were extracted. The total numbers of false negatives, false positives, and true positives are shown in Table 3 for Sentinel-1 and in Table 4 for ALOS-2. For Sentinel-1, the Wishart detector obtained the highest number of true positives and the smallest number of false negatives, and for ALOS-2 this was obtained by the log-normal detector. For C-band, the smallest number of false positives was achieved by the log-normal detector and for L-band by the K detector, but with the log-normal detector showing only a single additional false positive. It is worth noting that the number of false negatives is almost as large as of the true positives for all detectors, which means that almost half of the icebergs are missed by all the detection algorithms. To investigate why so many icebergs are missed, we have added the detection accuracy for various iceberg sizes below.

Of the 492 icebergs used in the study, 181 are classified as small, 175 as medium, and 136 as large (Table 2). For each of the detectors, the optimum PFA value was chosen to determine the absolute number of detected icebergs as a function of iceberg size for Sentinel-1 (Table 5) and ALOS-2 (Table 6). The results clearly demonstrate the considerable increase of detection rates for larger icebergs and hence the influence of the effective spatial resolution of the SAR images. For small icebergs, detection rates are extremely low, emphasizing the need for employing SAR systems which acquire images with high spatial resolutions on the order of 10 m (while at the same time keeping a large swath width). As icebergs become smaller than the resolution limit of the sensors, most icebergs are no longer separable from the background clutter. A few small icebergs are still detected, which might be due to their orientation or geometry giving rise to a strong backscattering into the direction of the SAR antenna.

The execution time for object detection is an important issue in operational iceberg mapping. Therefore, we determined it for the six detectors. Each detector was run at a PFA level of 1×10^{-12}, and the execution time was tested both on a small subset of 1000×1000 pixels and on the whole Sentinel-1 EW scene. The small subset covered an area containing only water and icebergs, but for the whole Sentinel-1 EW scene, about 10 % of the image was masked as being land before applying the detectors – leaving approximately 110×10^6 pixels to be analyzed. The test was carried out on a 64 bit PC, equipped with an i7 processor at 2.60 GHz and 32.0 GB RAM. Four detectors could be run on a full Sentinel-1 EW scene in less than a minute, making them well suited for operational applications. For the K detector, the execution time was 76 s, but around 20 s is attributed to the look-up table calculation, which can be carried out once and afterwards be re-used in operational systems.

The performance of the different detectors was further assessed by visualizing the results on subsets of the SAR images, which are shown in Figs. 7 and 8 for Sentinel-1 and ALOS-2, respectively.

The subset covers an area containing several icebergs grounded along the coast of Labrador, as well as several icebergs floating in the open water. Objects identified with the various detectors are marked on the figures, with green triangles denoting true positives (TPs), yellow squares false neg-

Table 3. Sentinel-1. Number of false negatives (FNs), false positives (FPs), and true positives (TPs) for each of the detectors at the PFA level resulting in the highest F score. Bold type indicates the best score.

	Gamma (1×10^{-19})	iDPolRAD (1×10^{-10})	K (1×10^{-4})	Log-normal (1×10^{-5})	NIS (1×10^{-13})	Wishart (1×10^{-20})
FN	254	299	253	261	219	**216**
FP	32	74	49	**24**	65	70
TP	238	193	239	231	273	**276**

Table 4. ALOS-2. Number of false negatives (FNs), false positives (FPs), and true positives (TPs) for each of the detectors at the PFA level resulting in the highest F score. Bold type indicates the best score.

	Gamma (1×10^{-14})	iDPolRAD (1×10^{-16})	K (1×10^{-4})	Log-normal (1×10^{-7})	NIS (1×10^{-21})	Wishart (1×10^{-18})
FN	230	285	255	**201**	217	215
FP	84	261	**43**	44	111	124
TP	262	207	237	**291**	275	277

atives (FNs), and red circles false positives (FPs). The same subset is shown for Sentinel-1 and ALOS-2 images, but due to the different acquisition times, the position of some icebergs has changed between the two images. Both images were acquired in ScanSAR mode, and the subsets cover the border between two subswaths, which gives rise to a diagonal line with a different signal-to-noise ratio (SNR) on each side. This is seen in the top left corner of the Sentinel-1 image and through the center of the ALOS-2 image. In the Sentinel-1 image, variations of the sea clutter are visible as brightness differences in the open water. In the ALOS-2 image bright artifacts occur in the water, likely caused by range and azimuth ambiguities from the processing. The high density of icebergs, various clutter states, and image artifacts make this subset well suited to illustrate the advantages and disadvantages of the various detectors.

Figure 7 reveals that the gamma, log-normal, and K detectors all behave similarly, with a limited number of false positives, and an approximately equal number of true positives and false negatives. The NIS and Wishart detectors both show a lower number of false negatives along the coast in the top left of the image but also show a higher number of false positives in the top center of the image. These false detections appear to be caused by linear features in the open water, possibly some sort of ocean waves, which triggers false detections. With the iDPolRAD we obtained many false positives along the boundary between the subswaths. This area is also characterized by increased levels of noise in the HV-band (red color), which may falsely trigger the detector. Additionally, the iDPolRAD detector also shows many missed detections compared with the other detectors, especially along the coast in the top left corner of the subset.

For the ALOS-2 image in Fig. 8, we found a very similar performance for the log-normal and K detectors. Both show a low number of false positives, whereas more false positives are obtained with the gamma, NIS, and Wishart detectors along the diagonal subswath boundary through the center of the image. These three detectors also identified an increased number of false positives in the bottom of the image, which appear to be caused by azimuth ambiguities. As in the Sentinel-1 image, the iDPolRAD shows the highest number of false positives.

4.1 Summary

The highest F score (70.4 %) was achieved by the log-normal detector on the ALOS-2 image. Besides this detector, the performance of the different methods for iceberg detection is similar on C- and L-band SAR images, with maximum f scores around 60 %–65 %. However, we note that we had data available only for a case study of icebergs in open water under low wind speeds and melting conditions. Hence, further comparisons between L- and C-band may show that SAR images acquired at a particular frequency should be used for conditions not investigated here.

When comparing the results for the F score as a function of PFA obtained for the investigated detectors, we found that all are suitable for use considering individual limits, with the exception of the iDPolRAD detector, which can be related to the melting conditions (see Sect. 5). The advantage of the gamma, NIS, and Wishart detectors provides high F scores over a larger range of small PFA values. In wider range of low PFA levels we found an almost constant F score also for the iDPolRAD. The log-normal and K detectors showed a narrow maximum of the F score at larger levels of the PFA, which means that the thresholds for the optimal PFA are more difficult to fix beforehand. Moreover, according to our results, they differ between C- and L-band. We expect that the position of the maximum F score on the PFA axis

Table 5. Sentinel-1. Percentage of detected icebergs for each of the detectors at the PFA level resulting in the highest F score. Bold type indicates the highest detection rate.

Icebergs	N	Gamma (1×10^{-9})	iDPolRAD (1×10^{-10})	K (1×10^{-2})	Log-normal (1×10^{-2})	NIS (1×10^{-13})	Wishart (1×10^{-20})
Small	181	6.6 %	5.0 %	6.6 %	6.6 %	11.6 %	**13.3 %**
Medium	175	57.7 %	40.6 %	58.9 %	56.0 %	**70.3 %**	69.7 %
Large	136	91.9 %	83.1 %	91.2 %	89.0 %	94.9 %	**95.6 %**

Table 6. ALOS-2. Percentage of detected icebergs for each of the detectors at the PFA level resulting in the highest F score. Bold type indicates the highest detection rate.

Icebergs	N	Gamma (1×10^{-7})	iDPolRAD (1×10^{-16})	K (1×10^{-2})	Log-normal (1×10^{-4})	NIS (1×10^{-21})	Wishart (1×10^{-18})
Small	181	10.5 %	5.5 %	7.7 %	**15.5 %**	9.9 %	11.0 %
Medium	175	65.1 %	48.6 %	57.1 %	**80.6 %**	73.1 %	72.0 %
Large	136	94.9 %	82.4 %	90.4 %	89.7 %	94.9 %	**96.3 %**

may also depend on the specific conditions (freezing, melting, rough or smooth water, and ice surface).

Our results of the detectability as a function of iceberg size shows that as many as 20 %–40 % of the medium icebergs (60–120 m) are not found using the detection methods tested here, even though the pixel spacing of the images used is of 40 m. This indicates that many medium-sized icebergs might be missed in operational charting.

5 Discussion

5.1 Factors influencing the accuracy of detection rates

For verifying the iceberg detections in the SAR images based on matches with icebergs identified in the Sentinel-2 image, we had to consider the drift of the icebergs between the times of acquisitions of the different images as explained above. Larger icebergs could be identified more easily in all images. For those icebergs, we used the direct displacement between the respective SAR image and the Sentinel-2 image as drift vectors. For icebergs shorter than 50 m, which were more difficult to match between the optical and the radar images, we estimated a drift path based on an interpolation between adjacent drift vectors from larger icebergs. The interpolation builds on the assumption that the smaller icebergs maintain the same heading and speed as the neighboring larger icebergs. This assumption might not always hold considering that the forces from wind and currents on icebergs depend on the cross-sections of their sails and keels (Wesche and Dierking, 2016), which causes larger uncertainties of the drift vectors, especially over large distances. Considering that the drift field between the Sentinel-1 and the Sentinel-2 image contains more interpolated drift paths and that the drift distance is larger, we may underestimate the performance of iceberg detection at C-band. In the future, more advanced drift predictions could be used to limit this type of uncertainty. Alternatively, having optical data acquired at the same time as the SAR overpasses would avoid the need for advanced drift correction. In our case, we also must take into account that the ALOS-2 images were down-sampled, which means that the identification of icebergs is made more difficult in the L-band images.

Other factors that influence the results which we obtained for missed and false detections are iceberg disintegration (icebergs breaking into smaller fragments) and the occurrence of ghost reflections at L-band (Gray and Arsenault, 1991). As illustrated in Fig. 9, ghost reflections were visible in the ALOS-2 imagery as small secondary reflections downrange of the main radar returns for some icebergs.

The study was carried out using only a single image pair, due to the limited availability of overlapping C- and L-band SAR and optical images. As such, the effect of different wind conditions and sea states on the detection performance could not be systematically investigated. However, based on the optical image we identified a large number of icebergs, which support the validity of the results under the conditions tested here.

The ocean wind field derived from the Sentinel-1 image used in the study shows that the wind speed at acquisition time was low, between 2–8 m s^{-1}. The time difference between the Sentinel-1 and ALOS-2 acquisitions is around 6 h. Therefore, we examined ECMWF Reanalysis v5 (ERA5) data, which revealed that the average daily wind speed for our AOI was at around 6 m s^{-1}. Since areas with low wind also exhibit low ocean backscatter, there is a risk that the signal for some areas becomes dominated by system noise rather than the true backscatter. This, in turn, increases the risk of false positives from the system noise. In our results this is

Table 7. Execution times of the different detection algorithms. The speed test was done for a 1000×1000-pixel subset of the Sentinel-1 EW scene (left) and for the full Sentinel-1 EW image (right) of approximately 110×10^6 pixels.

Algorithm	Run time (1000×1000 px)	Run time (entire S1E W scene)
Log-normal	292 [ms]	41.3 [s]
Gamma	144 [ms]	20.1 [s]
K distribution*	2157 [ms]	76.0 [s]
iDPolRAD	1319 [ms]	181.4 [s]
NIS	185 [ms]	27.6 [s]
Wishart	174 [ms]	27.8 [s]

* For the K detector, calculation of the look-up table takes approximately 20 s.

recognized as a high number of false positives along subswath transitions for both Sentinel-1 and ALOS-2 (Figs. 7–8). For these cases, a higher wind speed, and thus higher background backscatter from the ocean, might improve the performance due to an increase in signal-to-noise ratio. In an operational system, the number of false positives could also be reduced by applying improved filtering and noise reduction techniques in the pre-processing of images. This could, for example, be achieved using the methods suggested by Park et al. (2019) or Yang et al. (2021), which have shown promising results. However, these methods need to be investigated in detail to ensure that the noise removal algorithms do not affect point targets and as such degrade iceberg detection.

For future work, it is of great interest to investigate how various detectors perform under varying wind and temperature conditions and to consider different radar frequencies and polarizations. It is expected that L-band SAR is less sensitive to sea surface roughness than C-band, and hence L-band should in theory be better suited for iceberg detection under rough wind conditions (Dierking and Davidson, 2020). Increasing wind also may increase the variation of backscattering (affecting the image texture), which could have the positive effect of increasing the accuracy for the K detector. Similarly, increasing wind conditions might lead to worse performance for the detectors based on the gamma distribution, i.e., the gamma, NIS, and Wishart detectors. Colder temperatures are also expected to affect the results, with freezing conditions likely giving rise to more volume scattering from the icebergs, which might lead to a higher detection rate by, for example, the iDPolRAD detector.

Our results showed that the detection rate decreased rapidly as the iceberg size decreased, and it seems unlikely that the current ScanSAR image modes from Sentinel-1 and ALOS-2 will be useful for the detection and mapping of small icebergs unless better models for clutter estimation are developed. As mentioned in Sect. 3.3, outliers covering only a single pixel were removed as these were often caused by speckle noise, which would not have been necessary had the detectors been able to accurately model the clutter noise. However, we did not investigate the effects of the multi-looking applied to the images, and it is worth considering in future studies whether using single-look images might improve the detection accuracy for small icebergs considering the trade-off between noise and resolution. Regardless of these considerations, SAR data with a higher spatial resolution will likely improve the detection accuracy for smaller icebergs in the future.

5.2 Interpretation of results for the recall

As mentioned earlier, the rapid increase in recall with increasing PFA may be caused by the way we match icebergs between the optical and the radar image. To account for uncertainties, we define a search radius in the radar image around the expected position of an iceberg identified in the optical image, based on its estimated drift path. Especially for the interpolated drift vectors, this search radius is large (Sect. 3.4). So as the PFA level increases, the detectors will be more and more triggered by speckle or other radar intensity variations (e.g., due to strong reflections from a rough water surface) within the search radius. Since the search radius is larger for Sentinel-1, and Sentinel-1 also has a lower ENL, and hence higher variance of the speckle, we expect that this issue will be more obvious for Sentinel-1 compared to ALOS-2, which may explain the sudden large increase in recall for Sentinel-1. As the number of false detections increases inside the search circle, it will also increase outside, which in turn will lead to a sharp decrease in precision. Both effects determine the shape of the F score curves shown in Fig. 6.

5.3 Interpreting the results of different detectors

The different detectors show a maximum of the F score at different PFA levels: the NIS, gamma, and Wishart detectors at very low PFA levels and the K and log-normal detectors at higher PFA levels. Looking at the recall (Fig. 4) and precision (Fig. 5), we see that the K and log-normal detectors are generally less sensitive to both icebergs and noise (late increase in recall and late decrease in precision). We found that the different detectors performed similarly for the two SAR sensors, except for the log-normal detector, which showed a

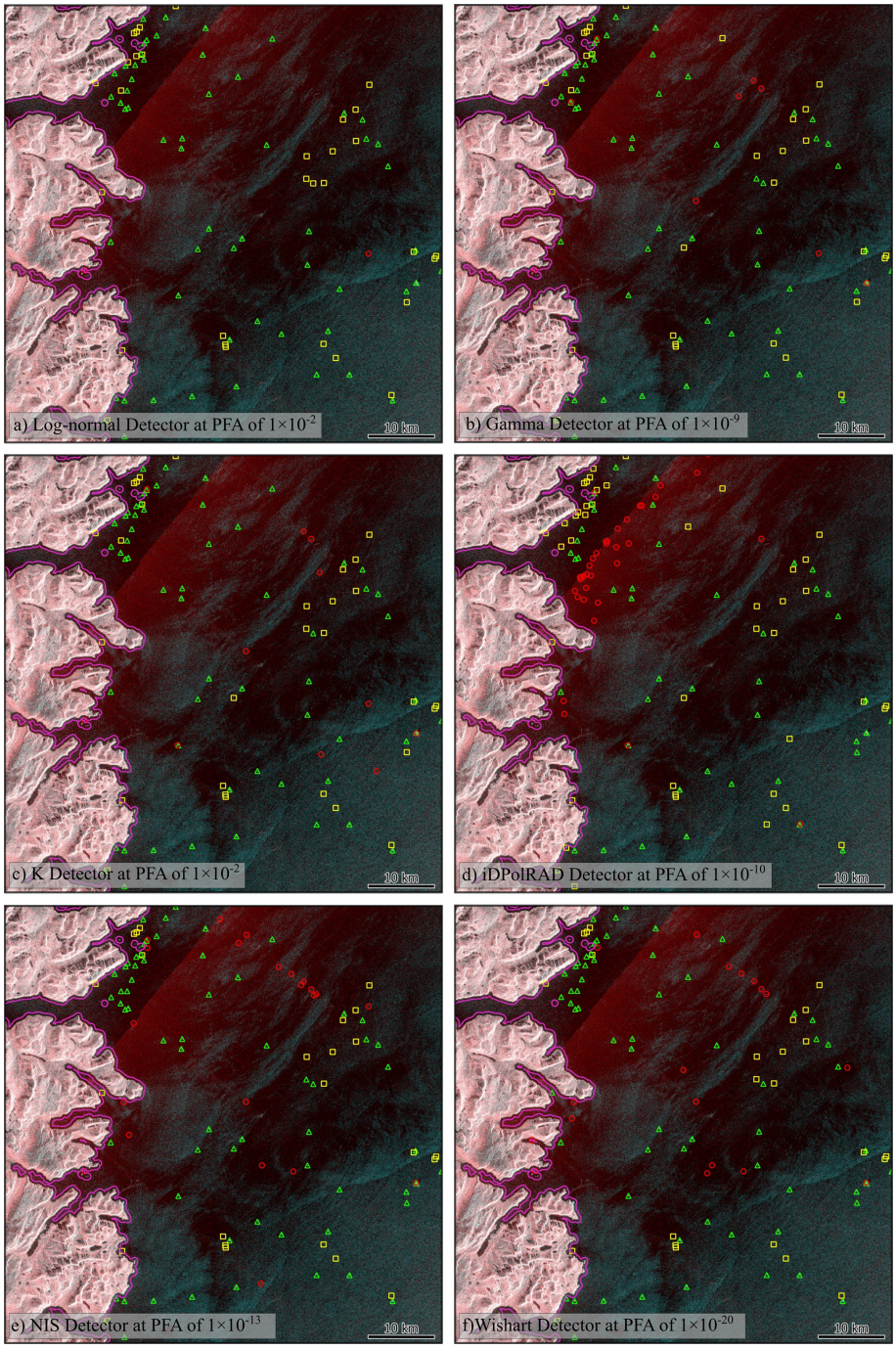

Figure 7. Detections for the six detectors for a subset of the C-band Sentinel-1 image. Green circles: true positives. Yellow squares: false negatives. Red triangles: false positives. HV in red channel, HH in green and blue channel. The background SAR composite is color-coded: red – HV, green – HH, blue – HH.

higher F score for L-band than for C-band. This could indicate that the model of radar intensity variations due to sea clutter used in the log-normal detector is more accurate at L-band than at C-band at least for the sea states that were represented in our dataset.

The similar overall performance of the gamma, NIS, and Wishart detectors is a consequence of the design of these detectors. All three assume that the noise in the HH and HV channels follows a gamma distribution. The NIS detector finds outliers in the linear combination of the normalized intensities at HH and HV polarization. The Wishart detec-

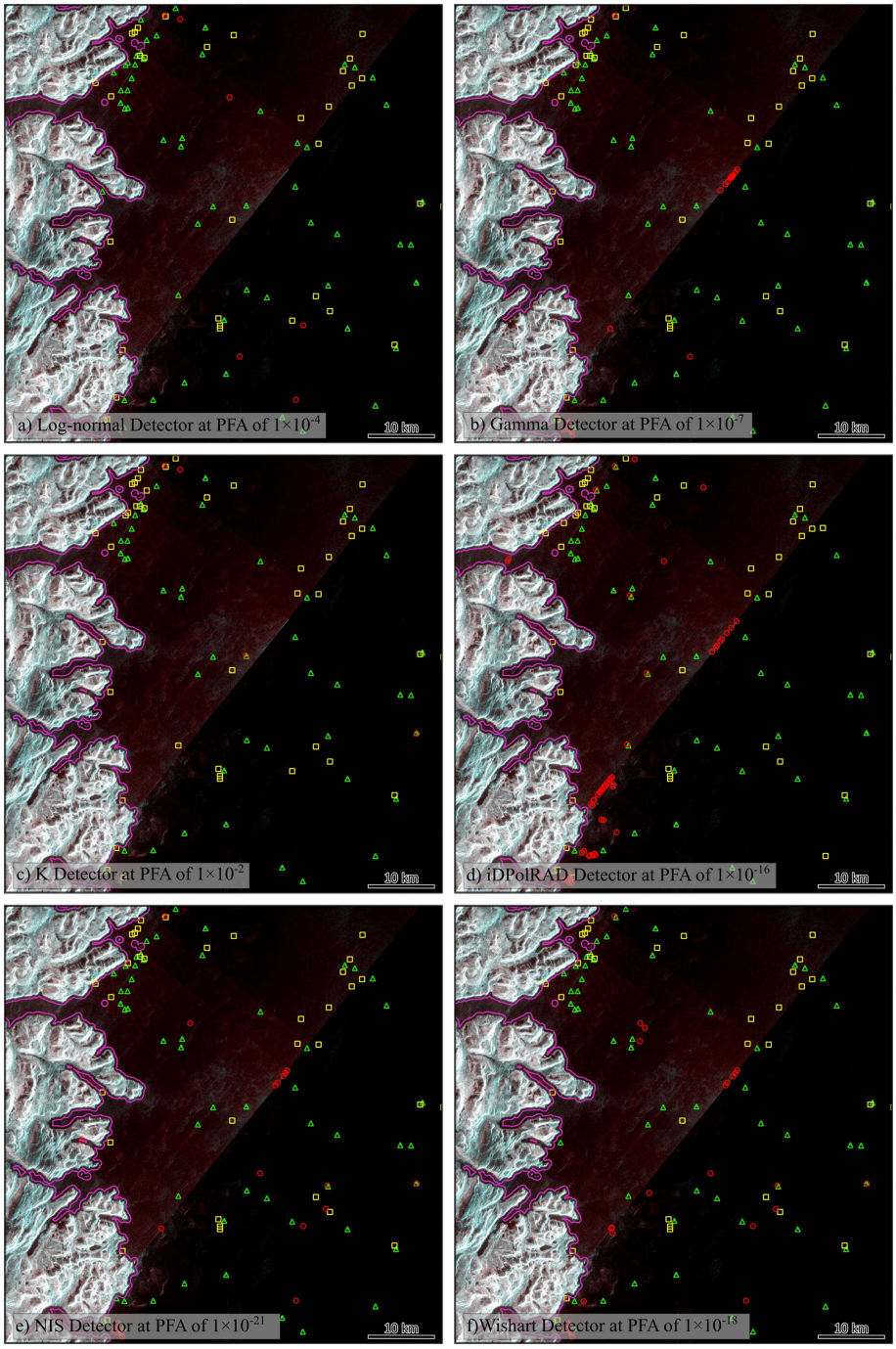

Figure 8. Detections for the six detectors for a subset the L-band ALOS-2 image. Green circles: true positives. Yellow squares: false negatives. Red triangles: false positives. HV in red channel, HH in green and blue channel. The background SAR composite is color-coded: red – HV, green – HH, blue – HH.

tor is based on the multi-dimensional Wishart distribution in which the contributions of the different polarizations are considered. And the gamma detector find outliers in the HH and HV bands independently and highlights outliers visible in both bands. Hence, all three detectors should be sensitive to the same outliers, with some minor variations for targets that show higher backscatter for only one of the polarizations.

In general, the iDPolRAD detector shows only moderate performance across all performance measures and for both C- and L-band. The main weakness of the detector appears to be its tendency to be triggered by the noise occurring

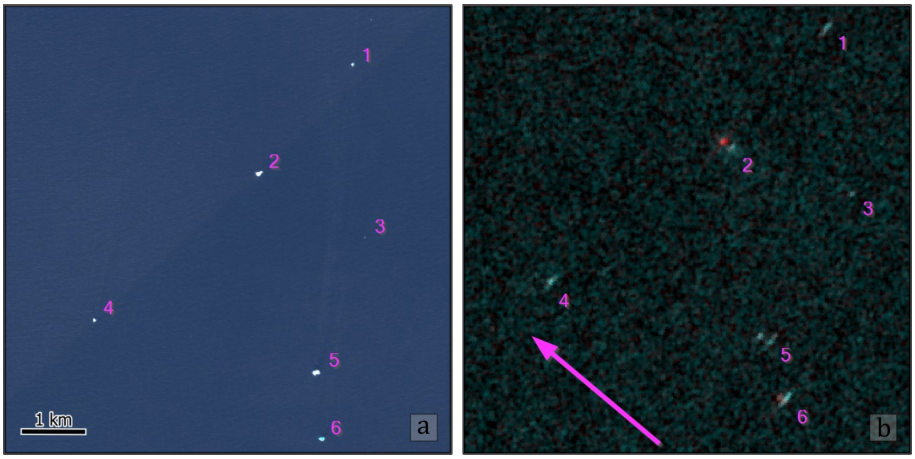

Figure 9. Example of the internal ghost reflections. Six icebergs are marked in the Sentinel-2 image **(a)**, and in the ALOS-2 image **(b)**. Iceberg numbers 2, 5, and 6 show two distinct reflections, with an initial bright reflection followed by a reflection further downrange. The secondary reflection is typically dimmer and often dominated by HV scattering (red). The look direction of the ALOS-2 satellite is marked by the arrow.

along the subswath boundaries. However, these false detections could theoretically be filtered in the post-processing. The reason we did not apply a filter like this for our study was possible complications a filter like this might add; for example, a subswath filter might remove some true positives.

Another weakness of the iDPolRAD detector is its sensitivity to melting conditions. Melting at the surface of icebergs causes a considerable decrease of the penetration depth of the SAR signal at both L- and C-band, hence reducing the volume scattering component. The presence of the latter is the major criterion for separating icebergs from the background dominated by surface scattering. Additionally, since the icebergs used in this study have drifted far from their calving areas, they may have turned over underway, causing the formation of salty ice layers on the icebergs' surface, which also leads to a decrease of volume scattering. The detector should hence only be applied under freezing conditions and close to calving sites, where rolling-over is less probable.

5.4 Sensitivity of F score to changes of PFA

The main strength of using the F score is that it reveals how changes in PFA influence the accuracy of detection. We clearly demonstrated that some detectors are quite sensitive to small changes in PFA level, whereas others are quite stable under varying PFA levels (Fig. 6). Normally, detectors are compared at similar PFA levels because it is assumed that the PFA is representative of the actual false alarm rate, but due to various implementation details or inaccurate assumptions as mentioned earlier, this might not always be the case. Our results showed that the NIS, gamma, and Wishart detectors obtain a high accuracy across a wide range of PFA levels. Similarly, the log-normal detector obtained a high F score for a wide range of PFA levels for the ALOS-2 data. But K detector (and the log-normal detector applied to C-band) obtained a high accuracy only for a narrow range of PFA values. This could indicate that these distributions are ill-suited for fitting variations of the sea surface clutter in the tail of the distribution so that small changes in PFA level result in large changes in the cut-off threshold for determining whether pixels belong to the background or iceberg class. However, more work is required to confirm this. Nevertheless, our results underline the importance of looking at a broad range of PFA levels instead of evaluating all the detection algorithms at one fixed PFA level.

6 Conclusion

In this paper, we have compared the performance of six different CFAR detectors for iceberg detection in both a C-band Sentinel-1 SAR image and a L-band ALOS-2 SAR image. Both images were acquired over the same region of the Labrador Sea and were acquired in wide-swath dual-polarization (HH, HV) mode. A total of 492 icebergs were visually identified in the study area, using an overlapping Sentinel-2 image for validation. The performance of the detectors was assessed by counting the number of false positives, true positives, and false negatives and calculating the corresponding recall, precision, and F score. Each detector was tested at varying PFA levels, making it possible to assess the performance of the detectors as a function of the PFA level. Additionally, the results for the PFA level that gave the highest F score were analyzed to investigate the detection rate for icebergs at varying sizes.

Comparing the individual detection algorithms on C- and L-band revealed no large differences, except for the iDPolRAD detector, which showed a higher F score on C-band,

and the log-normal detector, which showed a higher F score on L-band. This shows that not all detectors tested on C-band imagery can be applied to L-band imagery with the same expected results.

Overall, the highest accuracy was obtained by applying a log-normal CFAR detector to the ALOS-2 L-band image, which gave an F score of 70.4 %. In general, the gamma, NIS, and Wishart detectors all gave F scores above 62 % for both C- and L-band. Additionally, these three detectors were shown to be very stable to changes in the PFA level. The K detector resulted in F scores comparable with the other detectors but was also shown to be very sensitive to tuning of the PFA level. A similar result was obtained by the log-normal detector applied to the C-band image. A detector developed for iceberg detection in sea ice, the iDPolRAD detector, showed only moderate performance for icebergs in open water – possibly due to the high temperatures in the study area.

Three different methods were tested for merging the dual-channel HH/HV images for CFAR detection. But the methods used did not appear to give rise to any significant differences, with similar performance for the gamma, NIS, and Wishart detectors.

Only 10 %–15 % of the icebergs shorter than 60 m could be detected in the dataset, suggesting that wide-swath SAR images at both C- and L-band are insufficient for detecting small icebergs. Additionally, between 20 %–50 % of the medium icebergs (60–120 m) and 5 %–20 % of the large icebergs (>120 m) were missed by the detectors. This shows that a large part of icebergs that are 1.5–3 times size of a single pixel are not being detected, suggesting a risk of underestimating iceberg conditions by operational iceberg charting services.

Each of the detectors obtained their highest F score at different PFA levels. This suggests that comparing detectors at the same PFA level will give inaccurate results. The results also revealed that some detectors were sensitive to variations in PFA level, while others proved more stable. This suggests that the sensitive detectors should be used with care or undergo manual tuning for optimum results. We therefore recommend that the detectors with stable response to changing PFA level, namely NIS, Wishart, and gamma, are used when implementing an operational iceberg detection product.

L-bands appear to offer a slight improvement over C-bands on the dataset in this study. We expect this improvement to be even higher for cases with more wind, and we encourage further investigations of the use of L-band SAR data for detecting icebergs under varying wind conditions.

Code availability. Implementations of the different detectors are available on GitHub (https://github.com/LaustFaerch/cfar-object-detection, last access: 6 December 2023; DOI: https://doi.org/10.5281/zenodo.10254677, Færch, 2023).

Data availability. Historical weather data for Canada can be accessed here: https://climate.weather.gc.ca (Government of Canada, 2023). Historical weather data for Greenland can be accessed here: https://www.dmi.dk/vejrarkiv (Danish Meteorological Institute, 2021). Satellite images from the Sentinel-1 and Sentinel-2 satellite constellations can be accessed through the Copernicus dataspace: https://dataspace.copernicus.eu/ (Copernicus, 2023). ALOS-2 images from JAXA cannot be shared per the mutual cooperation project between ESA and JAXA.

Author contributions. The method was developed by LF and WD. The dataset was produced and analyzed by LF, who also led the manuscript writing. APD gave advice on the methodology and on the implementation and theory behind the detectors. NH offered advice on the operational aspects of iceberg detection services. WD, APD, and NH all contributed to the manuscript.

Competing interests. The contact author has declared that none of the authors has any competing interests.

Disclaimer. Publisher's note: Copernicus Publications remains neutral with regard to jurisdictional claims made in the text, published maps, institutional affiliations, or any other geographical representation in this paper. While Copernicus Publications makes every effort to include appropriate place names, the final responsibility lies with the authors.

Acknowledgements. ALOS-2/PALSAR-2 data are provided by JAXA through the 2019 to 2022 mutual cooperation project between ESA and JAXA on Using Synthetic Aperture Radar Satellites in Earth Science and Applications. We are thankful for the support received by the ESA and the Ministry of Science and Technology (MOST) of the PR China through the Dragon-5 cooperation. And we are also thankful for the discussions with our Chinese partners.

Financial support. This research has been supported by CIRFA partners and the Research Council of Norway (grant no. 237906). The publication charges for this article have been funded by a grant from the publication fund of UiT The Arctic University of Norway.

Review statement. This paper was edited by John Yackel and reviewed by two anonymous referees.

References

Akbari, V. and Brekke, C.: Iceberg Detection in Open and Ice-Infested Waters Using C-Band Polarimetric Synthetic Aperture Radar, IEEE T. Geosci. Remote, 56, 407–421, https://doi.org/10.1109/TGRS.2017.2748394, 2018.

Anfinsen, S. N., Doulgeris, A. P., and Eltoft, T.: Estimation of the Equivalent Number of Looks in Polarimetric Synthetic Aper-

ture Radar Imagery, IEEE T. Geosci. Remote, 47, 3795–3809, https://doi.org/10.1109/TGRS.2009.2019269, 2009.

Argenti, F., Lapini, A., Bianchi, T., and Alparone, L.: A Tutorial on Speckle Reduction in Synthetic Aperture Radar Images, IEEE Geosci. Remote Sens. Mag., 1, 6–35, https://doi.org/10.1109/MGRS.2013.2277512, 2013.

Bailey, J. and Marino, A.: Quad-Polarimetric Multi-Scale Analysis of Icebergs in ALOS-2 SAR Data: A Comparison between Icebergs in West and East Greenland, Remote Sensing, 12, 1864, https://doi.org/10.3390/rs12111864, 2020.

Bailey, J., Marino, A., and Akbari, V.: Comparison of Target Detectors to Identify Icebergs in Quad-Polarimetric L-Band Synthetic Aperture Radar Data, Remote Sensing, 13, 1753, https://doi.org/10.3390/rs13091753, 2021.

Barbat, M. M., Rackow, T., Hellmer, H. H., Wesche, C., and Mata, M. M.: Three Years of Near-Coastal Antarctic Iceberg Distribution From a Machine Learning Approach Applied to SAR Imagery, J. Geophys. Res.-Oceans, 124, 6658–6672, https://doi.org/10.1029/2019JC015205, 2019.

Bourbigot, M., Johnson, H., and Piantanda, R.: Sentinel-1 Product Definition, ESA, https://sentinels.copernicus.eu/web/sentinel/user-guides/sentinel-1-sar/document-library/-/asset_publisher/1dO7RF5fJMbd/content/sentinel-1-product-definition (last access: 6 December 2023), 2016.

Brekke, C.: Automatic ship detection based on satellite SAR, FFI, ISBN 978-82-464-1582-6, http://hdl.handle.net/20.500.12242/2139 (last access: 6 December 2023), 2009.

Brekke, C. and Anfinsen, S. N.: Ship Detection in Ice-Infested Waters Based on Dual-Polarization SAR Imagery, IEEE Geosci. Remote Sensing Lett., 8, 391–395, https://doi.org/10.1109/LGRS.2010.2078796, 2011.

Buus-Hinkler, J., Qvistgaard, K., and Krane, K. A. H.: Iceberg number density – Reaching a full picture of the Greenland waters, in: 2014 IEEE Geoscience and Remote Sensing Symposium, IGARSS 2014–2014 IEEE International Geoscience and Remote Sensing Symposium, Quebec City, QC, 270–273, https://doi.org/10.1109/IGARSS.2014.6946409, 2014.

Connetable, P., Conradsen, K., Nielsen, A. A., and Skriver, H.: Test Statistics for Reflection Symmetry: Applications to Quad-Polarimetric SAR Data for Detection of Man-Made Structures, IEEE J. Sel. Top. Appl., 15, 2877–2890, https://doi.org/10.1109/JSTARS.2022.3162670, 2022.

Conradsen, K., Nielsen, A. A., Schou, J., and Skriver, H.: A test statistic in the complex wishart distribution and its application to change detection in polarimetric SAR data, IEEE T. Geosci. Remote, 41, 4–19, https://doi.org/10.1109/TGRS.2002.808066, 2003.

Copernicus: Data Space Eco System, Copernicus [data set], https://dataspace.copernicus.eu/, last access: 6 December 2023.

Crisp, D. J.: The state-of-the-art in ship detection in synthetic aperture radar imagery, DSTO, Dept. Defense, Australian Government, Canberra, IC, Australia, 2004.

Danish Meteorological Institute: Verjarkiv, Danish Meteorological Institute [data set], https://www.dmi.dk/vejrarkiv/, last access: 14 September 2021.

Das, A., Kumar, R., and Rosen, P.: Nisar Mission Overview and Updates on ISRO Science Plan, in: 2021 IEEE International India Geoscience and Remote Sensing Symposium (InGARSS), 2021 IEEE International India Geoscience and Remote Sensing Symposium (InGARSS), Ahmedabad, India, 269–272, https://doi.org/10.1109/InGARSS51564.2021.9791979, 2021.

Davidson, M., Gebert, N., and Giulicchi, L.: ROSE-L – The L-band SAR Mission for Copernicus, in: EUSAR 2021; 13th European Conference on Synthetic Aperture Radar, Leipzig, Germany 29 March 2021–1 April 2021, https://ieeexplore.ieee.org/servlet/opac?punumber=9472486 (last access: 9 December 2023), 2021.

Denbina, M. and Collins, M. J.: Iceberg Detection Using Compact Polarimetric Synthetic Aperture Radar, Atmos. Ocean, 50, 437–446, https://doi.org/10.1080/07055900.2012.733307, 2012.

Denbina, M. and Collins, M. J.: Iceberg Detection Using Simulated Dual-Polarized Radarsat Constellation Data, Can. J. Remote Sens., 40, 165–178, https://doi.org/10.1080/07038992.2014.945517, 2014.

Dierking, W.: Sea Ice And Icebergs. Maritime Surveillance with Synthetic Aperture Radar, edited by: Di Martino, G. and Iodice, A., Institution of Engineering and Technology, 346 pp., ISBN 9781785616013, https://doi.org/10.1049/SBRA521E, 2020.

Dierking, W. and Davidson, M.: Enhanced Sea Ice Monitoring At L- and C-Bands using Rose-L and Sentinel-1, in: IGARSS 2020–2020 IEEE International Geoscience and Remote Sensing Symposium, IGARSS 2020–2020 IEEE International Geoscience and Remote Sensing Symposium, Waikoloa, HI, USA, 4059–4060, https://doi.org/10.1109/IGARSS39084.2020.9323886, 2020.

Dierking, W. and Wesche, C.: C-Band Radar Polarimetry – Useful for Detection of Icebergs in Sea Ice?, IEEE T. Geosci. Remote, 52, 25–37, https://doi.org/10.1109/TGRS.2012.2234756, 2014.

Doulgeris, A. P., Anfinsen, S. N., and Eltoft, T.: Automated non-gaussian clustering of polarimetric synthetic aperture radar images, IEEE T. Geosci. Remote, 49, 3665–3676, https://doi.org/10.1109/TGRS.2011.2140120, 2011.

El-Darymli, K., McGuire, P., Power, D., and Moloney, C.: Target detection in synthetic aperture radar imagery: a state-of-the-art survey, J. Appl. Remote Sens, 7, 071598, https://doi.org/10.1117/1.JRS.7.071598, 2013.

Færch, L.: CFAR Object Detection Library (Version v1), Zenodo [code], https://doi.org/10.5281/zenodo.10254677, 2023.

Gill, R. S.: Operational Detection of Sea Ice Edges and Icebergs Using SAR, Can. J. Remote Sens., 27, 411–432, https://doi.org/10.1080/07038992.2001.10854884, 2001.

Gillies, S. et al.: Rasterio: geospatial raster I/O for Python programmers, GitHub [code], https://github.com/rasterio/rasterio (last access: 17 November 2022), 2013.

Goodman, N. R.: Statistical Analysis Based on a Certain Multivariate Complex Gaussian Distribution (An Introduction), Ann. Math. Statist., 34, 152–177, https://doi.org/10.1214/aoms/1177704250, 1963.

Government of Canada: Environment and natural resources, Weather, Climate and Hazards, Past weather and climate, Historical Data, Government of Canada [data set], https://climate.weather.gc.ca, last access: 18 January 2023.

Gray, A. L. and Arsenault, L. D.: Time-delayed reflections in L-band synthetic aperture radar imagery of icebergs, IEEE T. Geosci. Remote, 29, 284–291, https://doi.org/10.1109/36.73670, 1991.

Harris, C. R., Millman, K. J., van der Walt, S. J., Gommers, R., Virtanen, P., Cournapeau, D., Wieser, E., Taylor, J., Berg, S., Smith, N. J., Kern, R., Picus, M., Hoyer, S., van Kerkwijk, M. H., Brett, M., Haldane, A., del Río, J. F., Wiebe, M., Peterson, P., Gérard-

Marchant, P., Sheppard, K., Reddy, T., Weckesser, W., Abbasi, H., Gohlke, C., and Oliphant, T. E.: Array programming with NumPy, Nature, 585, 357–362, https://doi.org/10.1038/s41586-020-2649-2, 2020.

Howell, C., Youden, J., Lane, K., Power, D., Randell, C., and Flett, D.: Iceberg and ship discrimination with ENVISAT multi-polarization ASAR, in: IGARSS 2004. 2004 IEEE International Geoscience and Remote Sensing Symposium, Anchorage, AK, USA, 2004, 113–116, https://doi.org/10.1109/IGARSS.2004.1368958, 2004.

JAXA: ALOS-2/PALSAR-2 Level 1.1/1.5/2.1/3.1 CEOS SAR Product Format Description, Rev. G, Japanese Aerospace Exploration Agency, https://www.eorc.jaxa.jp/ALOS/en/alos-2/datause/a2_format_e.htm (last access: 6 December 2023), 2012.

Karvonen, J., Gegiuc, A., Niskanen, T., Montonen, A., Buus-Hinkler, J., and Rinne, E.: Iceberg Detection in Dual-Polarized C-Band SAR Imagery by Segmentation and Nonparametric CFAR (SnP-CFAR), IEEE T. Geosci. Remote, 60, 4300812, https://doi.org/10.1109/TGRS.2021.3070312, 2022.

Kim, J.-W., Kim, D.-J., Kim, S.-H., and Hwang, B.-J.: Iceberg detection using full-polarimetric RADARSAT-2 SAR data in west antarctica, in: 3rd International Asia-Pacific Conference on Synthetic Aperture Radar (APSAR), Seoul, Korea (South), 26–30 September 2011, 1–4, 2011.

Lam, S. K., Pitrou, A., and Seibert, S.: Numba: a LLVM-based Python JIT compiler, in: Proceedings of the Second Workshop on the LLVM Compiler Infrastructure in HPC, SC15: The International Conference for High Performance Computing, Networking, Storage and Analysis, Austin Texas, 1–6, https://doi.org/10.1145/2833157.2833162, 2015.

Lee, J.-S. and Pottier, E.: Polarimetric Radar Imaging: From Basics to Applications, 1st edn., edited by: Lee, J.-S. and Pottier, E., CRC Press, https://doi.org/10.1201/9781420054989, 2009.

Liu, C.: A dual-polarization ship detection algorithm, DRDC-RDDC-2015-R109, Ottawa Research Centre, 2015.

Liu, C.: Method for Fitting K-Distributed Probability Density Function to Ocean Pixels in Dual-Polarization SAR, Can. J. Remote Sens., 44, 299–310, https://doi.org/10.1080/07038992.2018.1491789, 2018.

Marino, A.: Iceberg Detection with L-Band ALOS-2 Data Using the Dual-POL Ratio Anomaly Detector, in: IGARSS 2018–2018 IEEE International Geoscience and Remote Sensing Symposium, Valencia, Spain, 2018, 6067–6070, https://doi.org/10.1109/IGARSS.2018.8519206, 2018.

Marino, A., Dierking, W., and Wesche, C.: A Depolarization Ratio Anomaly Detector to Identify Icebergs in Sea Ice Using Dual-Polarization SAR Images, IEEE T. Geosci. Remote, 54, 5602–5615, https://doi.org/10.1109/TGRS.2016.2569450, 2016.

Novak, L. M. and Hesse, S. R.: Optimal Polarizations for Radar Detection and Recognition of Targets in Clutter, The Record of the 1993 IEEE National Radar Conference, Lynnfield, MA, USA, 79–83, https://doi.org/10.1109/NRC.1993.270489, 1993.

Oliver, C. and Quegan, S.: Understanding synthetic aperture radar images, SciTech Publishing Inc. Raleigh, NC 27613, ISBN 1-891121-31-6, 2004.

OpenStreetMap contributors: Land Polygons, https://osmdata.openstreetmap.de/data/land-polygons.html, last access: 18 January 2023, 2015.

Park, J.-W., Won, J.-S., Korosov, A. A., Babiker, M., and Miranda, N.: Textural Noise Correction for Sentinel-1 TOPSAR Cross-Polarization Channel Images, IEEE T. Geosci. Remote, 57, 4040–4049, https://doi.org/10.1109/TGRS.2018.2889381, 2019.

Power, D., Youden, J., Lane, K., Randell, C., and Flett, D.: Iceberg Detection Capabilities of RADARSAT Synthetic Aperture Radar, Can. J. Remote Sens., 27, 476–486, https://doi.org/10.1080/07038992.2001.10854888, 2001.

Salkind, N. J.: Bonferroni test, in: Encyclopedia of Measurement and Statistics, Vol. 0, Sage Publications, Inc., 104–107, https://doi.org/10.4135/9781412952644, 2007.

Sandven, S., Babiker, M., and Kloster, K.: Iceberg observations in the Barents Sea by radar and optical satellite images, in: Proceedings of the ENVISAT Symposium, Montreux, Switzerland, 23–27 April 2007, ISBN 92-9291-200-1, 2007. 2007.

Schou, J., Skriver, H., Nielsen, A. A., and Conradsen, K.: CFAR edge detector for polarimetric SAR images, IEEE T. Geosci. Remote, 41, 20–32, https://doi.org/10.1109/TGRS.2002.808063, 2003.

Soldal, I., Dierking, W., Korosov, A., and Marino, A.: Automatic Detection of Small Icebergs in Fast Ice Using Satellite Wide-Swath SAR Images, Remote Sensing, 11, 806, https://doi.org/10.3390/rs11070806, 2019.

Tao, D., Doulgeris, A. P., and Brekke, C.: A Segmentation-Based CFAR Detection Algorithm Using Truncated Statistics, IEEE T. Geosci. Remote, 54, 2887–2898, https://doi.org/10.1109/TGRS.2015.2506822, 2016a.

Tao, D., Anfinsen, S. N., and Brekke, C.: Robust CFAR Detector Based on Truncated Statistics in Multiple-Target Situations, IEEE T. Geosci. Remote, 54, 117–134, https://doi.org/10.1109/TGRS.2015.2451311, 2016b.

Tunaley, J. K. E.: K-Distribution Algorithm, LRDC Technical Report, August, 2010.

Virtanen, P., Gommers, R., Oliphant, T. E., Haberland, M., Reddy, T., Cournapeau, D., Burovski, E., Peterson, P., Weckesser, W., Bright, J., van der Walt, S. J., Brett, M., Wilson, J., Millman, K. J., Mayorov, N., Nelson, A. R. J., Jones, E., Kern, R., Larson, E., Carey, C. J., Polat, İ., Feng, Y., Moore, E. W., VanderPlas, J., Laxalde, D., Perktold, J., Cimrman, R., Henriksen, I., Quintero, E. A., Harris, C. R., Archibald, A. M., Ribeiro, A. H., Pedregosa, F., van Mulbregt, P., and SciPy 1.0 Contributors: SciPy 1.0: fundamental algorithms for scientific computing in Python, Nat. Methods, 17, 261–272, https://doi.org/10.1038/s41592-019-0686-2, 2020.

Wesche, C. and Dierking, W.: Iceberg signatures and detection in SAR images in two test regions of the Weddell Sea, Antarctica, J. Glaciol., 58, 325–339, https://doi.org/10.3189/2012J0G11J020, 2012.

Wesche, C. and Dierking, W.: Estimating iceberg paths using a wind-driven drift model, Cold Reg. Sci. Technol., 125, 31–39, https://doi.org/10.1016/j.coldregions.2016.01.008, 2016.

Willis, C. J., Macklin, J. T., Partington, K. C., Teleki, K. A., Rees, W. G., and Williams, R. G.: Iceberg detection using ERS-1 Synthetic Aperture Radar, Int. J. Remote Sens., 17, 1777–1795, https://doi.org/10.1080/01431169608948739, 1996.

Yang, W., Li, Y., Liu, W., Chen, J., Li, C., and Men, Z.: Scalloping Suppression for ScanSAR Images Based on Modified Kalman Filter With Preprocessing, IEEE T. Geosci. Remote, 59, 7535–7546, https://doi.org/10.1109/TGRS.2020.3034098, 2021.

Zakharov, I., Power, D., Howell, M., and Warren, S.: Improved detection of icebergs in sea ice with RADARSAT-2 polarimetric data, in: 2017 IEEE International Geoscience and Remote Sensing Symposium (IGARSS), Fort Worth, TX, USA, 2017, 2294–2297, https://doi.org/10.1109/IGARSS.2017.8127448, 2017.

/7

Paper II: Mapping icebergs in sea ice: An analysis of seasonal SAR backscatter at C- and L-band

Færch, L., Dierking, W., Hughes, N., and Doulgeris, A. P. Remote Sensing of Environment, Volume 304, https://doi.org/10.1016/j.rse.2024.114074, 2024.

Remote Sensing of Environment 304 (2024) 114074

Contents lists available at ScienceDirect

Remote Sensing of Environment

journal homepage: www.elsevier.com/locate/rse

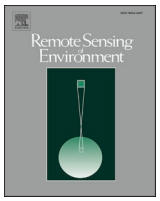

Mapping icebergs in sea ice: An analysis of seasonal SAR backscatter at C- and L-band

Laust Færch [a,*], Wolfgang Dierking [a,b], Nick Hughes [c], Anthony P. Doulgeris [a]

[a] Center for Integrated Remote Sensing and Forecasting for Arctic Operations, Department of Physics and Technology, UiT—The Arctic University of Norway, 9019 Tromsø, Norway
[b] Alfred Wegener Institute, Helmholtz Center for Polar and Marine Research, Germany
[c] Norwegian Meteorological Institute, Norway

ARTICLE INFO

Edited by Menghua Wang

Keywords:
Arctic
Belgica Bank
SAR
Icebergs
Sea ice

ABSTRACT

Icebergs in the Arctic can pose a threat to maritime traffic and offshore installations and influence the properties of the upper ocean layer. While icebergs in open water are regularly monitored using C-band SAR satellites, less attention has been paid to icebergs in regions with a high areal fraction of sea ice, where detection using traditional methods is more difficult. In this study, we compare the capability of C- and L-band SAR to detect icebergs in level and deformed fast sea ice across various seasons. To this end we use a timeseries of SAR images acquired at HH- and HV-polarization in 2019 and 2020, covering respectively 301 and 356 icebergs. As reference data for validation, we used iceberg polygons derived from Sentinel-2 images. Our results reveal that compared to C-band, L-band SAR is significantly better at separating the backscatter of icebergs and sea ice and thus is preferable for detecting icebergs in ocean regions with a high sea ice concentration. It is further shown that L-band SAR is less affected by melting conditions, suggesting that it can be used for iceberg detections in both summer and winter.

1. Introduction

The calving of icebergs is one of the main sources of mass loss from ice sheets and glaciers. For the Greenland ice sheet, it is estimated that the annual solid ice discharge is on the order of 500 Gt/year (Mankoff et al., 2020). A large fraction of this discharge takes the form of medium and large icebergs (60–220 m in length), that float out into the ocean.

Icebergs act as large freshwater reservoirs to the ocean, and melting icebergs are therefore a direct source of freshwater to the ocean, leading to a reduction of salinity and cooling of the local water column, which affects ocean circulation and facilitates the formation of sea ice (Bügelmayer et al., 2015; Marson et al., 2021). This is especially significant in areas with a high iceberg density (Bigg, 2015, Ch. 4). Icebergs also pose a major threat to maritime traffic and offshore installations in the Arctic. Detecting and mapping the location of icebergs are therefore important both for ocean models and for maritime safety.

Typically, icebergs in open water can be detected using Synthetic Aperture Radar (SAR) satellites, and this is regularly done with C-band satellites such as Sentinel-1 or RADARSAT (Gill, 2001; Power et al., 2001; Sandven et al., 2007). Normally, iceberg detection algorithms are based on the observation that icebergs exhibit higher backscatter than the surrounding open water (Willis et al., 1996), and thus appear as bright spots against the darker ocean in SAR images. This can be utilized to find clusters of pixels with a high contrast relative to the local background, e.g., using a statistical approach such as the Constant False Alarm Rate (CFAR) detector (Oliver and Quegan, 2004). CFAR detectors have been used to map regional distributions of icebergs in open water in the Arctic, e.g., in Buus-Hinkler et al. (2014), and are currently being used to create operational iceberg density products by the Copernicus Marine Service for the waters around Greenland, Labrador and Newfoundland (Copernicus Marine Service, 2023).

However, mapping icebergs in regions with sea ice is more difficult using these techniques. This is mainly because sea ice exhibits highly variable backscatter, making it more difficult to detect outliers of backscattered intensity which can be related to icebergs (Dierking, 2020). This is especially difficult for rough or deformed sea ice, which is well known to have a higher and more variable backscatter response than level ice, thus lowering the contrast between icebergs and their background (Wesche and Dierking, 2012). Further, the backscatter response of sea ice shows seasonal variations (Haas, 2001), due to the

* Corresponding author.
E-mail address: laust.farch@uit.no (L. Færch).

https://doi.org/10.1016/j.rse.2024.114074
Received 23 August 2023; Received in revised form 16 February 2024; Accepted 19 February 2024
Available online 24 February 2024

related temperature changes (Casey et al., 2016; Yackel et al., 2007), that must be considered in algorithms for detecting icebergs in sea ice. In particular, melting is known to have a large impact on iceberg backscatter (Willis et al., 1996; Ferdous et al., 2019). Thus, icebergs in sea ice and close to the ice margin are currently not included in operational monitoring products, and a recent survey by the International Ice Charting Working Group (IICWG) noted that icebergs in sea ice should be considered in future operational ice charting products (IICWG, 2019).

The radar response of icebergs and sea ice arises primarily from a combination of surface and volume scattering (Willis et al., 1996; Haas, 2001; Power et al., 2001; Wesche and Dierking, 2012), where the exact contribution of each component is heavily influenced by the presence of water or wet snow on the surface and the salinity of the ice. Under freezing (dry) conditions and at low salinity, radar signals typically penetrate deeper into snow and ice than under thawing (wet) conditions and high salinity. Thus, the ability to distinguish between icebergs and sea ice in SAR images depends on both meteorological conditions and on the type of the surrounding sea ice (Mazur et al., 2017).

Even though some studies have suggested methods to detect icebergs in sea ice using C-band SAR, e.g., in Marino et al. (2016) and Zakharov et al. (2017), these studies did not consider the seasonal aspects or the influence of different types of sea ice. Other studies focusing on the Antarctic, typically employ object- or segmentation-based methods (Kim et al., 2011; Mazur et al., 2017; Barbat et al., 2019; Koo et al., 2023; Evans et al., 2023; Braakmann-Folgmann et al., 2023), which are not suitable for the Arctic where the smaller icebergs often only cover a few pixels in the SAR image. For the Arctic, studies covering larger regions with different ice types, e.g., by Dierking and Wesche (2014), and Soldal et al. (2019) reported difficulties to reliably detecting icebergs because of a large overlap in the backscatter characteristics of icebergs and sea ice.

It is expected that L-band SAR might improve iceberg detection in sea ice considering the longer wavelength and hence larger penetration depth into wet snow and ice and lower sensitivity to small-scale surface roughness (Casey et al., 2016; Rignot et al., 2014; Dierking and Davidson, 2020). This is quite interesting considering that several recent and planned launches of L-band SAR satellites, such as SAOCOM (Giraldez, 2004), NISAR (Das et al., 2021), and ROSE-L (Davidson et al., 2021), will increase the amount of available L-band data for the Arctic in the future.

However, only a few studies of iceberg detection using L-band SAR images have been carried out to date, e.g., by Marino (2018) and Bailey et al. (2021). And direct comparisons of C- and L-band SAR data for detecting icebergs in sea ice have not been attempted before. Given how radar signatures are affected by different meteorological and sea ice conditions, studies considering different sea ice types and covering different seasons are of high interest. Further, since small variations in iceberg geometry and orientation can affect backscatter responses significantly (Ferdous et al., 2018), studies must preferably be carried out using large datasets to avoid skewing the results. The validation of detection algorithms using a large independently obtained dataset covering different ice types and seasons has to our knowledge never been attempted due to the difficulties in obtaining the necessary data.

This study compares the backscatter contrast between icebergs and sea ice in C- and L-band SAR images, under different seasonal conditions. The contrast is used as an indicator for detectability, with high backscatter contrast between iceberg and sea ice indicating high detectability. The study is carried out using a large number of icebergs that are embedded in land-fast ice and a time series of SAR images covering several months, from freezing temperatures in the spring to the melting season later in the summer. Data from two separate years (2019 and 2020) were used in the study. The land-fast ice is segmented into regions of ice classified as either *level* or *deformed* to consider conditions in two main classes of sea ice. Although our results are technically restricted to icebergs in land-fast ice, we expect that our conclusions can be extended to icebergs in high-concentration drift ice of similar sea ice types. Additionally, large areas of the Arctic are covered in seasonal or permanent fast ice (Mahoney, 2018), and many of these areas are near ice-calving glaciers and ice caps (Wolken et al., 2020).

In summary our study helps to determine the limitations and advantages of using C- and L-band SAR, respectively, for mapping icebergs in areas with a high concentration of sea ice, especially considering different sea ice, and seasonal conditions.

2. Study area and data

2.1. Study area

The study was carried out over an area of interest (AOI) covering a section of Belgica Bank in north-eastern Greenland located between 78 and 80°N and 12–16°W. Our AOI covers approximately 23.000 km^2 in total. West of the AOI, two large ocean-terminating glaciers are located, the Nioghalvfjerdsbræ, and the Zachariae Isstrøm, each calving several gigatons of solid ice each year (Mankoff, 2020). East of the AOI, the East Greenland Current (EGC) transports large amounts of sea ice from the Arctic into the North Atlantic (Hughes et al., 2011).

A large area of Belgica Bank is shallow with depths <100 m, while it is surrounded by deep troughs of 300–400 m depth (Arndt, 2015). Many of the icebergs that calved from the glaciers ground on the shallow bank. Here, they are surrounded by sea ice transported down from the Arctic Ocean with the EGC. The icebergs block and catch some of the sea ice floes, and when the fast ice starts forming from the coast to the bank, the sea ice floes are embedded within the fast ice (Hughes 2011). This means that our AOI covers a large number of icebergs of varying sizes between 30 to 40 m and larger than a kilometer, and many different types of sea ice. Towards the open water on the eastern side of the bank, the land fast ice tends to be rough or deformed, consisting of the older floes from the north, while on the western side, the sea ice is typically newly formed and less deformed (level sea ice). Since both the sea ice and icebergs remain stationary for a long period, from winter freeze to summer melt, this is one of the best places in the Arctic to investigate how the backscatter response from icebergs and sea ice develops over different seasons.

2.2. Remote sensing data

L-band SAR images are from the ALOS-2 satellite, and C-band images from Sentinel-1. A time series of ALOS-2/PALSAR-2 images was provided by JAXA. It was acquired in ScanSAR Nominal, right-looking mode on a descending orbit (Fig. 1) and was delivered in a georeferenced Level 1.5 GeoTIFF format, however without incidence angle information.

Sentinel-1 images are available from the Copernicus program through an open data policy, and therefore it is possible to get almost daily coverage for our AOI with Sentinel-1. However, since our main interest is a comparison between C- and L-band, we opted to only download Sentinel-1 images from days when an ALOS-2 image was acquired. For a few of the ALOS-2 images, no image was available from Sentinel-1 from the same day. In these cases, the image nearest in time was used instead, which was typically an acquisition from the following or previous day. However, for most of the ALOS-2 images, a Sentinel-1 acquisition could be found within a time difference of 6 h.

The Sentinel-1 images were acquired in Extra Wide-Swath (EW) mode and were retrieved from the CREOtech Data and Information Access Service (CREODIAS) and processed using the Sentinel Applications Platforms (SNAP), including thermal noise removal, calibration, and ellipsoid correction. All Sentinel-1 acquisitions were acquired in a right-looking geometry and from descending orbits.

Referring to Fig. 1, since all images from both Sentinel-1 and ALOS-2 were acquired in right-looking geometries and from descending orbits, the near-range is on the right side of the images, and the far range on the left side. Both the C- and L-band images are acquired in dual-

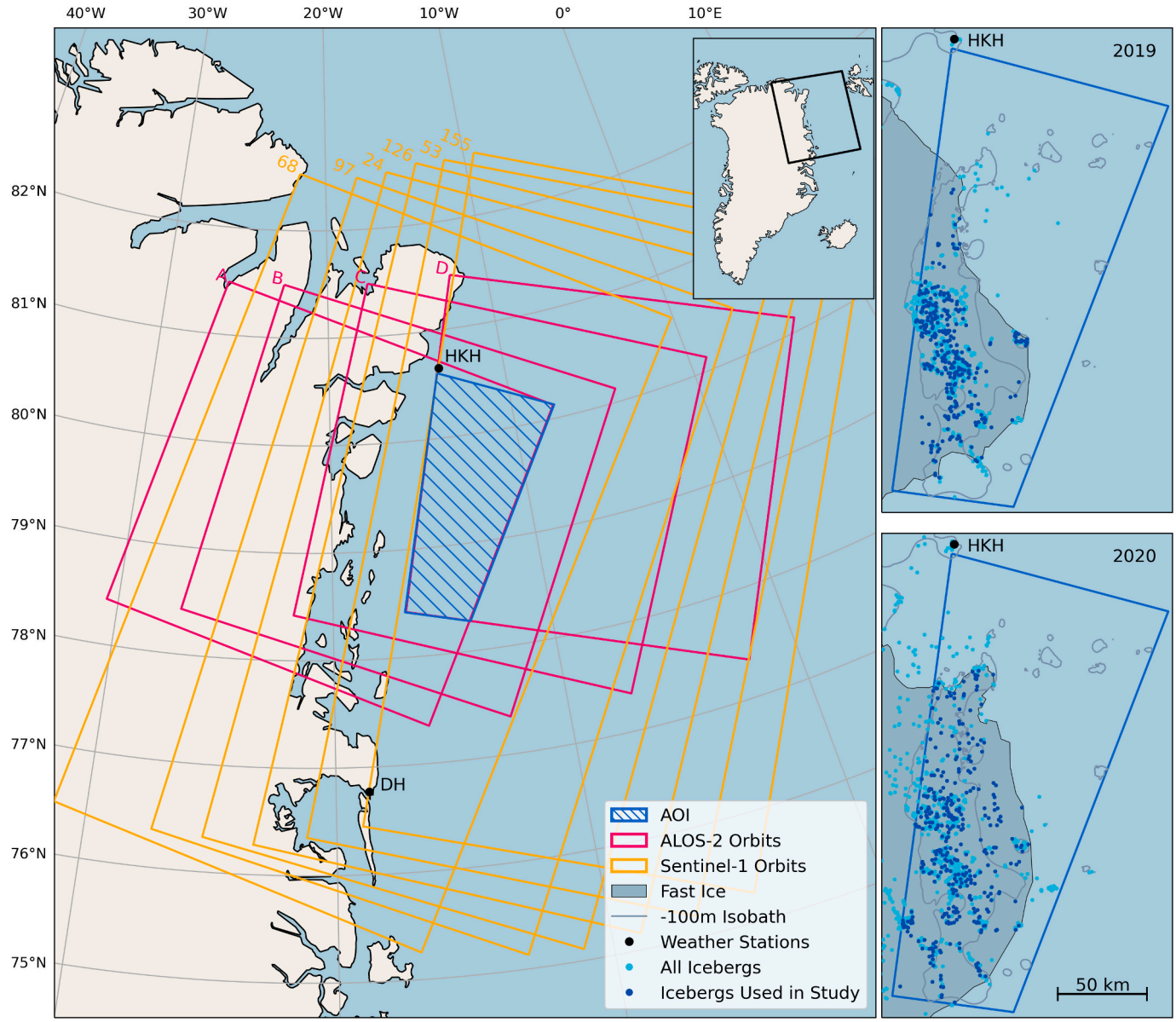

Fig. 1. Overview of the study area showing the AOI and the orbits from Sentinel-1 (orange) and ALOS-2 (red). The black dots mark the weather stations at Henrik Krøyer Holme (HKH), and Danmarkshavn (DH) respectively. On the right, the icebergs from 2019 and 2020 are shown, together with the fast-ice edge in mid-July, and the −100-m isobath from IBCAO V4.1 (Jakobsson et al., 2020). (For interpretation of the references to colour in this figure legend, the reader is referred to the web version of this article.)

polarization (HH, HV) mode, which is commonly used for sea ice mapping in the Arctic (Dierking, 2020) and hence widely available for iceberg detection in the Arctic as well.

A total of 22 ALOS-2 images were used from 2019 and 19 images from 2020, complemented by 14 Sentinel-1 images for 2019, and 17 images for 2020. All images were acquired in the period between April 1st and August 1st, covering the freezing season in the spring until the fast ice break up during summer. An overview of the image characteristics can be found in Table 1.

To complement the SAR data and for generating a validation data set, optical images from the European Sentinel-2 satellites were downloaded from CREODIAS. Here we used the RGB bands (B4, B3, and B2) at 10-m resolution.

Table 1
Overview of the SAR data used in the study. The Noise Equivalent Sigma Zero (NESZ)of Sentinel-1 varies with the incidence angle. *For ALOS-2, the NESZ is given in the mission requirements, but the actual value may be lower.

	Mode	NESZ*	Pixel Spacing	Looks (range, azimuth)	Polarization	Swath Width	Incidence Angle
Sentinel-1[a]	Extra Wide Swath (EW)	−24: −34 db	40 m	6 × 2	HH, HV	410 km	18.9–40.0
ALOS-2[b,c]	ScanSAR mode (WBD)	−26 db	25 m	2 × 3	HH, HV	360 km	22.7–45.9

[a] Bourbigot et al. (2016).
[b] JAXA (2012).
[c] Kankaku et al. (2013).

2.3. Validation data

Iceberg polygons served as validation data for the study. The polygons were drawn manually using optical Sentinel-2 images by experts from the Norwegian Meteorological Institute (MET Norway) (Amdal and Hughes, 2022). The icebergs are easily distinguishable in the optical images acquired in the spring when the sun is illuminating the icebergs from a very small grazing angle, thus generating distinct shadows.

To account for small errors in the geocoding, Sentinel-2 iceberg polygons shorter than 100 m in length were not considered in the analysis of the SAR images. Here, the length is calculated as the major axis of the minimum bounding rectangle of the iceberg polygon. Furthermore, icebergs that were within 400 m of a neighboring iceberg were also removed from the dataset to avoid mixing signals from several icebergs forming a cluster (see Section 3.3). Icebergs outside the AOI and the fast-ice edge were not considered in our analysis. Since the fast ice edge is slowly changing during the season, we used the fast ice edge from mid-July (see Fig. 1). That way, we ensure that all icebergs used for validation remain stationary for the entire study period. In total, 301 icebergs for 2019 and 356 icebergs for 2020 were used in the study. Examples of the different types of data used in the study are shown in Fig. 2.

2.4. Meteorological data

Temperature data from two weather stations close to the AOI were

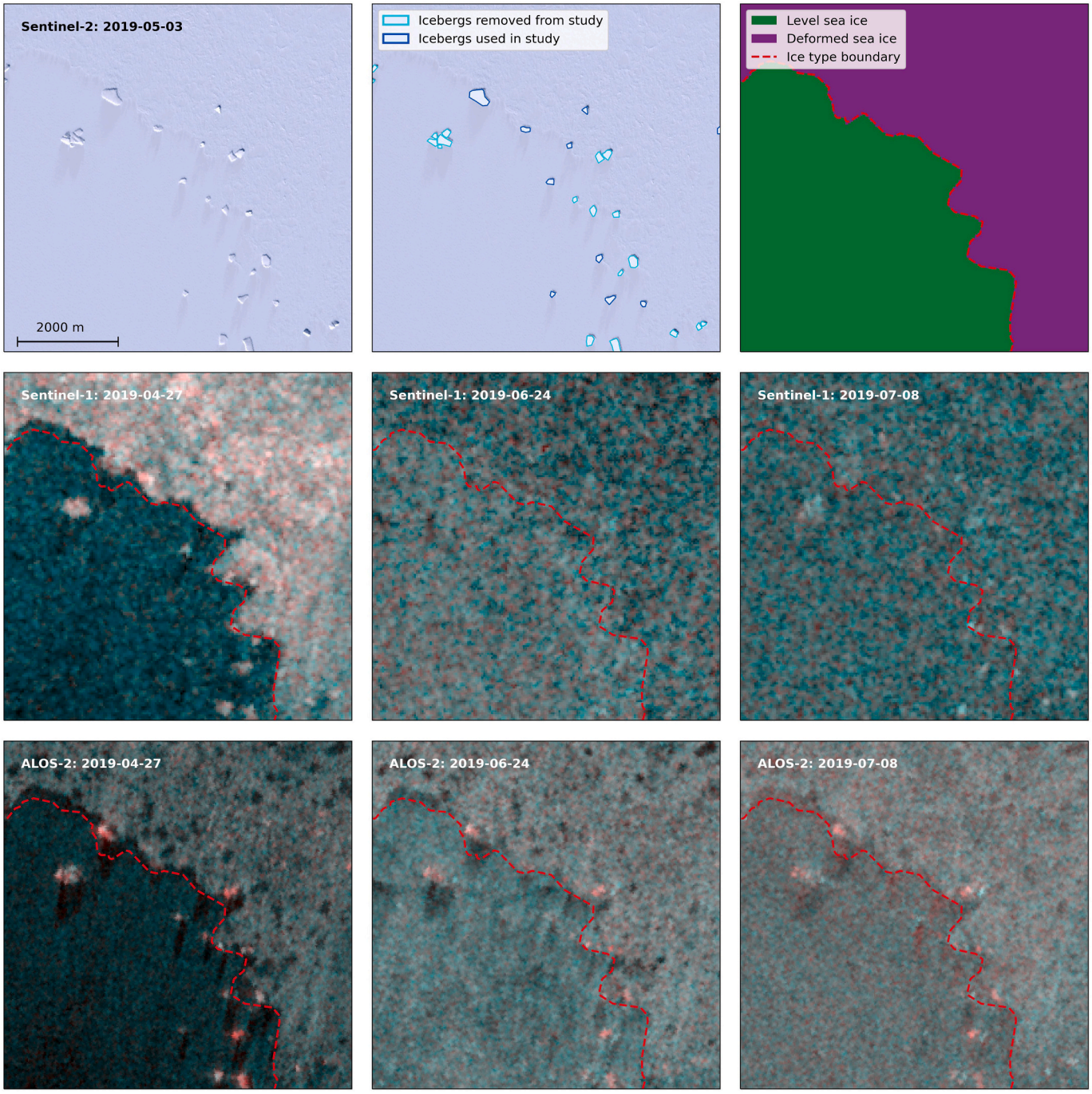

Fig. 2. Examples of the data used for the study. All images are covering the same subset of the AOI. The SAR images are colored as red: HV, green: HH, blue: HH. (For interpretation of the references to colour in this figure legend, the reader is referred to the web version of this article.)

downloaded from the Danish Meteorological Institute (Danish Meteorological Institute, 2023). The positions of the two stations are marked in Fig. 1. The southern part of the AOI has a higher iceberg density, which compensates for the larger distance of the southern weather station. Therefore, the overall temperature profile for our AOI was calculated as a daily average between the data from the two stations.

3. Methods

3.1. Method outline

As mentioned in Section 1, the main goal of this study is to compare the capability of C- and L-band SAR for detecting icebergs in level and rough sea ice under different seasonal conditions. To achieve this goal, we used the backscatter contrasts at HH- and HV-polarization between icebergs and the surrounding sea ice as a proxy for detectability. Therefore, we extracted the backscatter values for icebergs and sea ice and calculated the contrast for the entire timeseries (Sect. 3.3). Since we have to distinguish between level and deformed sea ice, a segmentation of the two types within our AOI was performed first (Sect. 3.2). A peculiarity of the radar response at L-band is the occurrence of time-delayed reflections which we discuss in Sect. 3.4.

In subsequent analyses presented in section 4 we explored whether the seasonal pattern of the backscattering contrast between icebergs and sea ice reveals any distinct seasonal patterns due to temperature variations, which is the case for sea ice backscatter (Haas, 2001; Casey et al., 2016; Yackel et al., 2007). Based on this analysis, the data were separated into freezing and melting periods. For each period, we investigated the variations of the backscattering coefficients from icebergs and sea ice for both C- and L-band to determine overlaps between the classes. This part of the study will also help to define boundaries in the backscatter at HH- and HV-polarization that might be useful for separating iceberg and sea ice signatures and improve existing detection algorithms.

3.2. Segmentation of level and deformed sea ice

A semi-automatic method was used to segment the fast ice into regions containing predominantly level and deformed sea ice. The segmentation was based on the observation that deformed ice generally exhibits higher backscatter values than level ice at both C- and L-band during winter (Dierking, 2010; Guo et al., 2022). Because we focus on fast ice, high backscattering, e.g., from pancake or brash ice or from frost-flower covered young ice in refreezing leads, can be excluded. Since the distribution of deformed and level ice does not change within the fast ice in the AOI, segmentation could be performed on images acquired before melt. For both 2019 and 2020, a single Sentinel-1 and a single ALOS-2 image were chosen for the segmentation. The images were manually selected based on appearance, showing strong visual distinction between level and deformed sea ice. The Sentinel-1 images were acquired on 2019-04-27 and 2020-04-09, and the ALOS-2 images on 2019-05-12 and 2020-04-26.

For each of the years, the two images were then stacked into a single image containing four bands (HH- and HV-polarization for both C- and L-band) and then processed by applying a Simple Linear Iterative Clustering (SLIC) segmentation algorithm (Achanta et al., 2012) using the scikit-image library (van der Walt et al., 2014) in Python. The SLIC algorithm uses a K-means approach to generate super-pixels, i.e., regions with high statistical similarity of the backscatter in the image. The SLIC algorithm used here was initialized with 1000 segments and a pre-processing Gaussian kernel of width 4 to reduce the speckle noise. Before applying the SLIC algorithm, each band of the image was truncated to the 5 and 95 quantiles decibel values, and then scaled to values between 0 and 1.

The resulting super-pixel polygons from the segmentation algorithm were then manually classified as either level or deformed sea ice. This was done by looking at the average backscatter levels within each segment and marking low-backscatter segments as *level* and high-backscatter segments as *deformed*. This manual classification was aided by optical Sentinel-2 images where in doubt. The area outside the mid-July fast-ice edge was marked as drift ice and thus not used in the study. This approach greatly eased the process of classification compared to drawing all the polygons by hand.

The resulting classified images are shown in Fig. 3. For 2019, 124 icebergs were located in level ice and 177 in deformed ice. For 2020, only 43 icebergs were found in level ice (because of a lower areal fraction of this ice type), and 313 in deformed ice.

3.3. Time-delayed reflections

A peculiarity that was observed in the ALOS-2 images was that the main backscatter return of the icebergs did not appear at the exact location of the iceberg polygons derived from the Sentinel-2 images. Rather the main reflection from the icebergs typically appeared some hundreds of meters down-range from the polygons. This shift is not caused by bad geolocation of the ALOS-2 images since the land and sea-ice boundaries are placed at the correct location, as seen in the optical images. The phenomenon was also observed in high-resolution ALOS-2 Stripmap images of the AOI (Fig. 4, top right) and have previously been observed for icebergs in open water as well (Færch et al., 2023).

Gray and Arsenault (1991) reported that icebergs could cause time-delayed reflections when imaged with L-band SAR. This was caused by the lower attenuation loss of the L-band signal in ice compared to the C-band signal, which means that radar signals penetrate the iceberg completely and are reflected from the bottom and the side walls. This means that from an L-band SAR perspective, the main and strongest reflection does not appear at the true location of the iceberg but rather a few hundred meters down range, due to the longer traveling path of the radar signal through the iceberg. Therefore, we extracted the backscatter values from the main reflection down-range which requires to consider the time delay of the signal, i.e., the spatial shift between the true location of an iceberg (from the Sentinel-2 imagery) and the backscatter maximum in the ALOS-2 image.

An exact calculation of the time delay of a single iceberg as a function of radar incidence angle is not possible, since it depends in addition on the sometimes very complex iceberg geometry (shape, height, length, width), the effective dielectric constant, the properties of potentially present snow and firn layers on the iceberg surface and any saline ice layers frozen to the iceberg.

The height of the icebergs could be inferred from the bathymetry assuming that they are all grounded. However, this assumption might not always hold for small icebergs that have broken off from larger bergs just before the consolidation of the land-fast ice. Additionally, the bathymetry data for the area also have uncertainties due to the sparse sampling in this region (Arndt et al., 2015), which necessarily adds uncertainty to the dataset.

In addition, the radar signal path in the iceberg may be variable as discussed in Gray and Arsenault (1991) and in Dierking and Wesche (2014). As multiple reflections within the iceberg (e.g., between bottom, side walls, and surface) may increase the time-delay and cause a more complex backscattering response of the iceberg, which again depends on the internal geometry of the icebergs.

Therefore, we developed a simple automatic matching method to identify the main backscatter reflection from each iceberg based on the observed backscatter intensities. This was done by iteratively shifting the iceberg polygons down-range in steps of 25 m, starting from 0 m and with a maximum distance of 350 m. Since a majority of the measured time delays were in the order of 50–200 m, a maximum distance of 350 m was chosen as an appropriate upper boundary. For each step, the average HV backscatter was calculated, and the original polygon was moved to a new location corresponding with the maximum backscatter within the (see Fig. 4). The HV backscatter was used here since it was

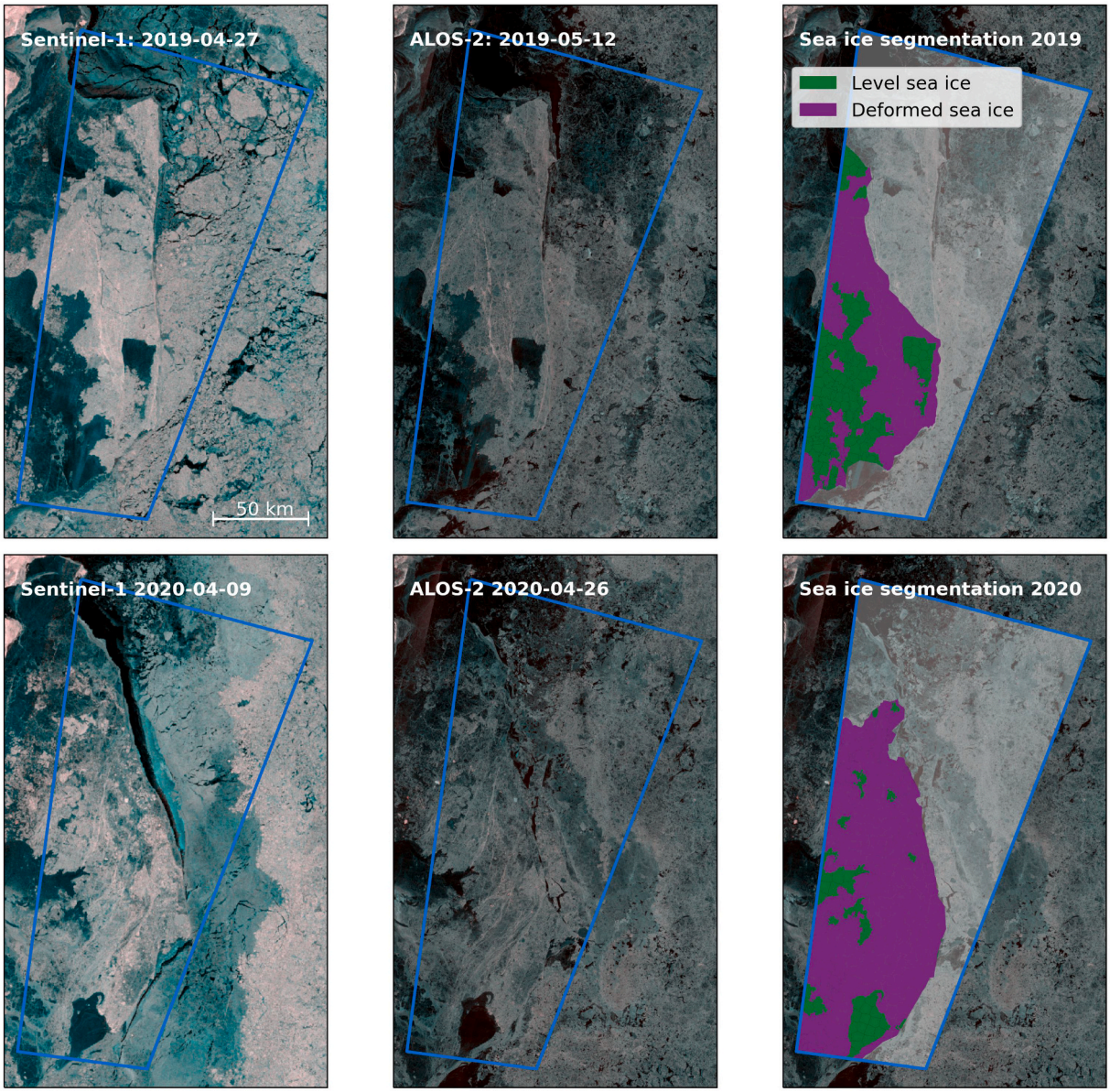

Fig. 3. Sea ice segmentation for 2019 (top) and 2020 (bottom) using the Sentinel-1 (left) and ALOS-2 images (center). The segmentation results (right) show level sea ice (green), deformed sea ice (purple), and drift ice (transparent gray). The AOI is marked with a blue polygon. The SAR images are colored as red: HV, green: HH, blue: HH. (For interpretation of the references to colour in this figure legend, the reader is referred to the web version of this article.)

observed that the contrast between icebergs and sea ice is significantly higher in the HV band compared to the HH band, this is e.g., seen in Figs. 2 and 4 where the icebergs in L-band is clearly distinguishable by their red colour. This may be explained by a recent study which reports that cold icebergs at L-band show a predominance of volume scattering (Bailey and Marino, 2020).

All time delays determined as described above were in the range between 0 and 300 m. In order to avoid mixing signals of neighboring icebergs, all icebergs with neighbors closer than 400 m were discarded from the analysis as described in Section 2.3. The process was repeated for all icebergs in all ALOS-2 images, as different orbits and meteorological conditions are also expected to affect the penetration and thus time delay.

3.4. Extraction of backscatter and contrast values

All icebergs in the dataset were classified according to the predominant sea ice type in which they were embedded (level or deformed), using the results from the segmentation in Section 3.2. Then, for each iceberg, a single backscatter value was extracted using the iceberg polygon. This was done by calculating the average backscatter (in linear intensity) of all the pixels that were touched by the polygon. The number of pixels used for calculating this average backscatter thus varies according to the size of the iceberg.

The backscatter of the surrounding sea ice (background) was also extracted for each iceberg. This was done using a window of 1600 × 1600 meters centered around the iceberg. Here, the iceberg polygons were used to mask out icebergs from the background to avoid contaminating the background backscatter with iceberg samples. In addition, if the icebergs were located close to an edge between different sea ice classes, the smallest class was also masked to avoid contamination. As such, the number of pixels used to estimate the background backscatter levels also varies depending on iceberg size, location of nearby icebergs, and variations of sea ice deformation. But generally, the average background backscatter is estimated using a larger number of pixels than the iceberg backscatter. As above, the calculation of the average sea ice

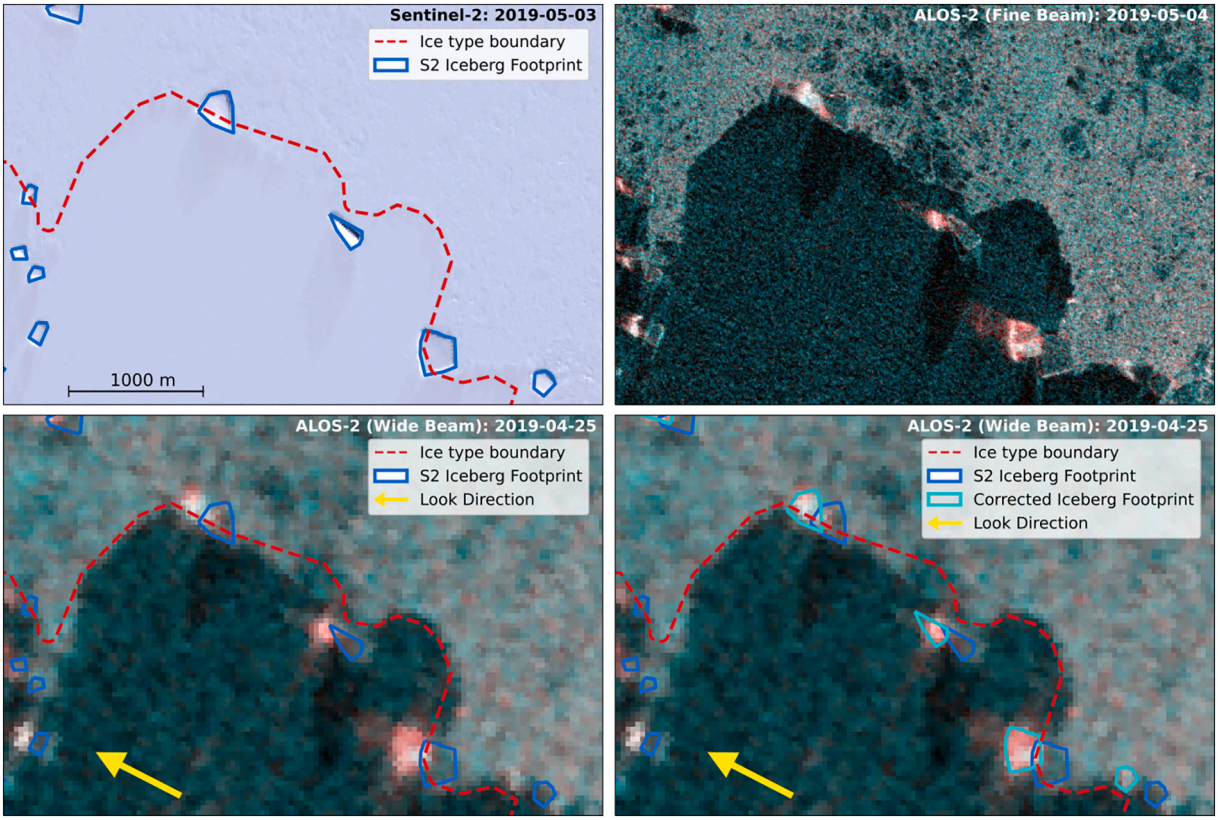

Fig. 4. Time-delayed reflection in L-band SAR images. The main reflection in the SAR image does not correspond with the location of the iceberg polygons from Sentinel-2 (blue outline). The edge between level and deformed sea ice in the SAR image, however, matches the boundary from the optical image (red dotted line). An automatic matching algorithm finds the main reflection down-range (cyan outline), by shifting the polygons downrange (yellow arrow). The SAR images are colored as red: HV, green: HH, blue: HH. (For interpretation of the references to colour in this figure legend, the reader is referred to the web version of this article.)

backscatter was also performed in the linear intensity domain.

The extraction of the average intensities was done for each iceberg in each scene. For the ALOS-2 images, the iceberg polygons were corrected as described in Section 3.3. Then, the contrast was calculated for each iceberg as the ratio between the means of iceberg and sea ice backscatter. The results were then grouped according to several parameters such as sensor, acquisition date, satellite orbit, polarization, and sea ice type. The calculations were done using Python 3.10, with the Numpy (Harris et al., 2020), GeoPandas (Jordahl, 2014), and Rasterio (Gillies et al., 2013) libraries.

3.5. Automatic iceberg detection

In addition to an analysis of the backscatter, an automatic iceberg detection algorithm was tested on selected images to compare the detection rate for icebergs in level and deformed sea ice using C- and L-band images, respectively. For this purpose, a commonly used iceberg detection algorithm of CFAR type was applied to two Sentinel-1 and two ALOS-2 images respectively. For both sensors, we chose one image from 2019 and one image from 2020. The first Sentinel-1 and ALOS-2 images were acquired on April 27th, 2019, with the ALOS-2 image from orbit D and the Sentinel-1 image from orbit 126 (see Fig. 1). Also in 2020, both images were acquired on April 27th, from orbit B (ALOS-2), and orbit 126 (Sentinel-1). Hence, the algorithm could be tested on images covering two distinct ice conditions. Since the ALOS-2 and Sentinel-1 images are in different native resolution, the ALOS-2 images were resampled to the same pixel spacing as the Sentinel-1 images using nearest neighbor interpolation.

A Normalized Intensity Sum (NIS) detector was chosen to find outliers (Liu, 2015). When applied to dual-pol data, the NIS detector works by calculating a new channel as the sum of normalized intensities of the HH and HV channels. If we assume that the individual HH and HV channels follow a gamma distribution, then the NIS channel also follows a gamma distribution. As such, a gamma based CFAR detector can then be applied to the NIS channel to delineate outliers (Færch et al., 2023).

For the CFAR detector we used a probability of false alarm rate of 1e-14. Clutter estimation was carried out in a circular window with a diameter of 17 pixels, corresponding to 680 m at 40-m pixel spacing, and with a circular guard region with a diameter of 10 pixels, corresponding to 400 m. This means that the detector is optimized for icebergs smaller than 200 m in length, while it should also be able to detect slightly larger icebergs. The detection algorithm uses a fixed clutter region, i.e., it does not adapt to icebergs within the clutter estimation window, which means that the method is not optimal in areas with a high iceberg density due to the risk of iceberg pixels being included in the clutter estimation window.

Since the algorithm marks pixel outliers, groups of connected pixels were merged into polygons for further analysis. Here, polygons of a size of 3 pixels or smaller were discarded to avoid too many false positives caused by speckle. The computed polygons were then compared with the Sentinel-2 iceberg polygons. As mentioned earlier, icebergs smaller than 100 m in length were ignored, and icebergs outside the fast-ice edge were also removed from the analysis. To account for the time-delayed reflections at L-band, all detections from ALOS-2 were moved up-range by a fixed distance corresponding to the average time-delay for all the analysed icebergs. The distances were 100 m for the image acquired on 2019-04-27, and 160 m for the image from 2020 to 04-27. Icebergs in distances $\leq$400 m from other icebergs (i.e., icebergs in clusters) that were previously removed were kept in the validation data for this test. This procedure resulted in a total of 879 icebergs for 2019

(with 587 icebergs embedded in deformed sea ice, and 292 in level sea ice) and 909 icebergs for 2020 (767 in deformed sea ice and 142 in level sea ice).

The results were then divided into three categories. 1) If an iceberg identified in the Sentinel-2 reference data was overlapped by a polygon detected by the CFAR algorithm, the iceberg was marked as a true positive (TP). 2) If a Sentinel-2 iceberg polygon was not overlapped by a CFAR polygon, then the iceberg was marked as a false negative (FN). 3) CFAR polygons that did not overlap with a Sentinel-2 polygon were marked as false positives (FP). To further evaluate the performance, we also calculated the *precision* and *recall*,

$$Recall = \frac{TP}{TP + FN}$$

$$Precision = \frac{TP}{TP + FP}$$

As such, a low recall indicates a high number of false negatives compared to the number of true positives, while a low precision indicates a high number of false positives compared to the number of true positives.

Finally, the results were separated between level and deformed ice according to the outcome of the sea ice segmentation (Section 3.2), to distinguish the performance for icebergs in level and deformed sea ice.

4. Results

4.1. Backscatter contrast timeseries

In Figs. 5 and 6, the average backscatter contrasts between icebergs and their background are plotted for Sentinel-1 and ALOS-2 for each of the image acquisition dates. In the figures, we have also plotted the average daily temperature for the region. In addition, the different orbits used for each image have been marked to consider the influence of different incidence angles on the contrast. The backscatter contrast time series for Sentinel-1 are plotted in Figs. 5 for 2019 and 2020, respectively, while Fig. 6 show the ALOS-2 backscatter contrast time series for the two years, respectively.

The figures show that both Sentinel-1 and ALOS-2 offer a high contrast between icebergs and level sea ice during the beginning of each time series when temperatures are well below zero degrees Celsius, and that this contrast is higher for the HV polarization than for HH polarization. Additionally, we observe a decrease in the contrast when temperatures are close to or exceed 0 °C. For Sentinel-1, this decrease is clearly visible for level sea ice, while for ALOS-2, the decrease is visible for both sea ice types.

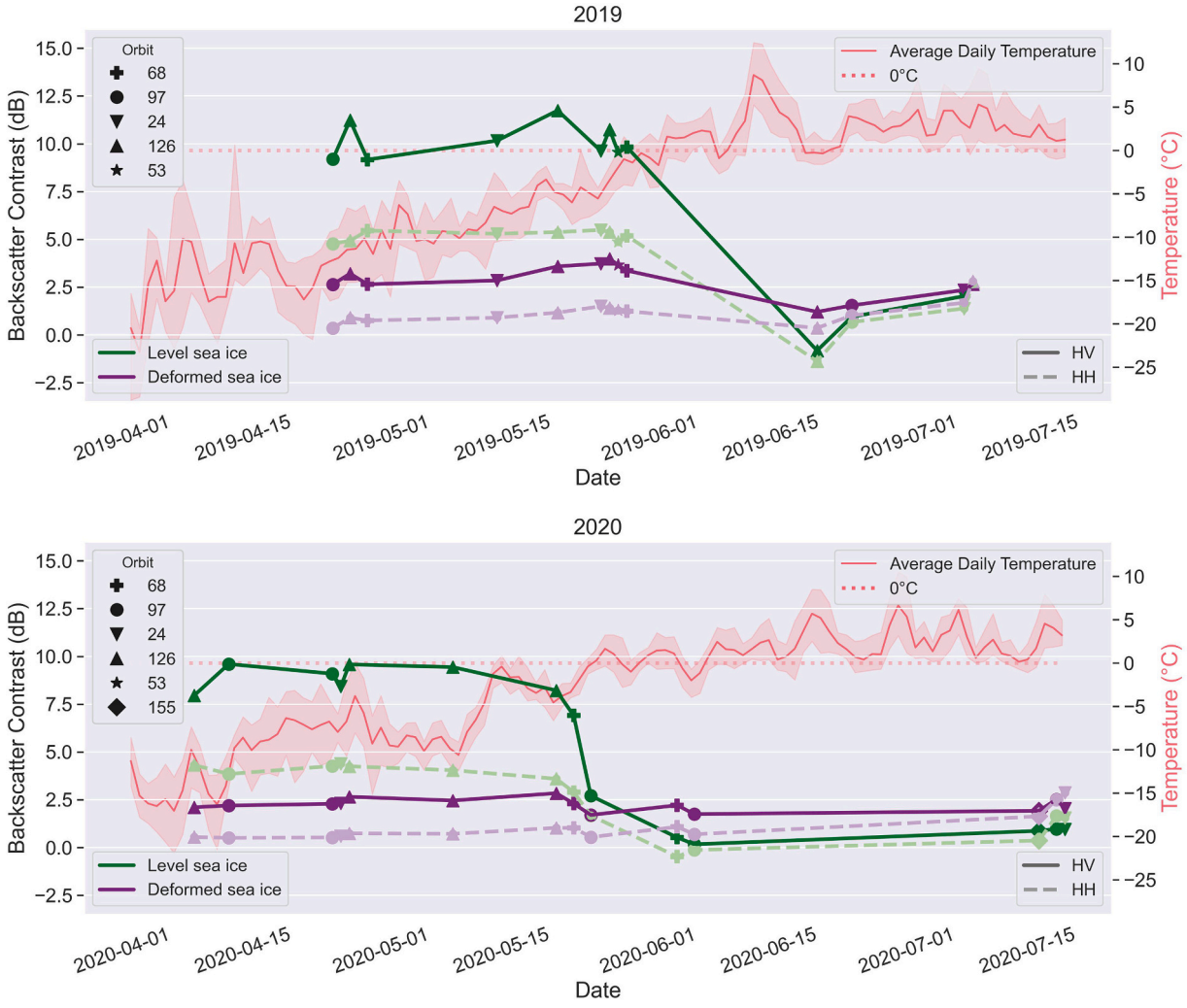

Fig. 5. Backscatter contrast for Sentinel-1 in 2019 (top) and 2020 (bottom). The contrast between level sea ice and icebergs (green) and deformed sea ice and icebergs (purple) are plotted for HV (full line) and HH (dashed line). The markers indicate the orbit numbers from Fig. 1. The daily temperature is plotted in the background (red), with shading indicating the fluctuations between daily minimum and maximum temperature. (For interpretation of the references to colour in this figure legend, the reader is referred to the web version of this article.)

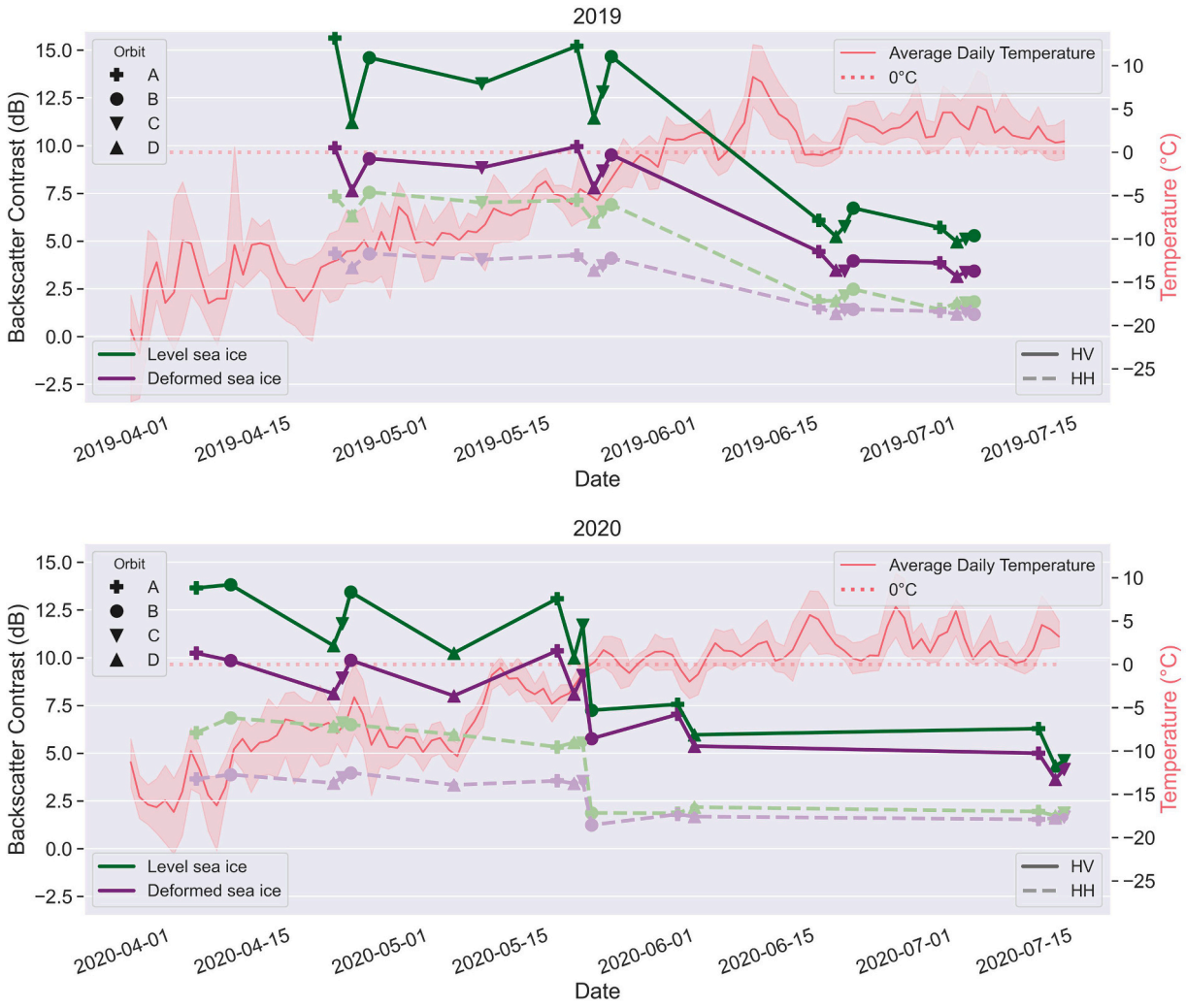

Fig. 6. Backscatter contrast for ALOS-2 in 2019 (top) and 2020 (bottom). The contrast between level sea ice and icebergs (green) and deformed sea ice and icebergs (purple) are plotted for HV (full line) and HH (dashed line). The markers indicate the orbit numbers from Fig. 1. The daily temperature is plotted in the background (red), with shading indicating the fluctuations between daily minimum and maximum temperature. (For interpretation of the references to colour in this figure legend, the reader is referred to the web version of this article.)

Figure 5 reveals a high contrast for level sea ice throughout spring (8–12 dB for HV and 4–5 dB for HH). Around the onset of melt, the contrast is sharply decreasing down to 0 ±2 dB for both HV and HH. For deformed ice, the contrast is significantly lower during the spring, with values around 2–4 dB for HV and around 0–2 dB for HH. At the onset of melt, the contrast for deformed ice decreases slightly down to around 0–2 dB. There are large similarities between 2019 and 2020, although 2019 exhibits slightly higher contrast during the spring than 2020.

Comparing ALOS-2 (Fig. 5) to Sentinel-1 (Fig. 6), an overall higher contrast is recognized during spring for both level and deformed ice at both HH- and HV-polarization. For level ice, the contrast varies between 10 and 14 dB for HV, and 6–8 dB for HH, while for deformed sea ice it varies around 8–10 dB for HV and remains stable around 4 dB for HH. Like the contrast for Sentinel-1, the contrast for ALOS-2 also shows a sharp decrease after the onset of summer melt. However, where the contrast for Sentinel-1 during the thawing season decreases to around 0 ±2 dB, the ALOS-2 contrast remains higher, with magnitudes around 6 dB for level sea ice and 4–5 dB for deformed sea ice.

The ALOS-2 contrast plot shows a large variation during the spring, especially for level sea ice which varies around 11–16 dB for 2019, and 10–14 dB in 2020 for the HV polarization. This variation correlates with the orbit numbers, with orbit D showing the lowest contrast and orbit A showing the highest. Referring to the overview plot in Fig. 1, we note that orbit A corresponds to near-range in the image (low incidence angles), and D to far-range (high incidence angles). This suggests that the contrast for ALOS-2 is highly sensitive to the incidence angle, with low incidence angles offering better detectability of icebergs.

Based on the contrast plots, our dataset can be divided into two main categories as a function of the air temperature. We denote these conditions *freezing* and *thawing*, where *thawing* has been defined as starting at the first day on the year when the average temperature for the past five days exceeds 0°, which was on June 4th, 2019, and May 28th, 2020.

4.2. Seasonal scatterplots

To investigate the relationship between backscattered intensity from icebergs and the two main sea ice types more in detail, we have plotted the intensities for Sentinel-1 and ALOS-2 in Figs. 7 and 8, respectively. The plots highlight the distributions of the backscatter and the correlation between polarizations for the three classes. This is helpful for separating the various classes and selecting the optimum detectors for finding icebergs in areas with a high sea ice concentration. The results were separated into *freezing* and *thawing* seasons depending on the average temperature as described in Section 4.1. Fig. 7 shows the results for Sentinel-1 (C-band), with the top row containing data from 2019 and the bottom row for 2020. The left column shows the data under freezing

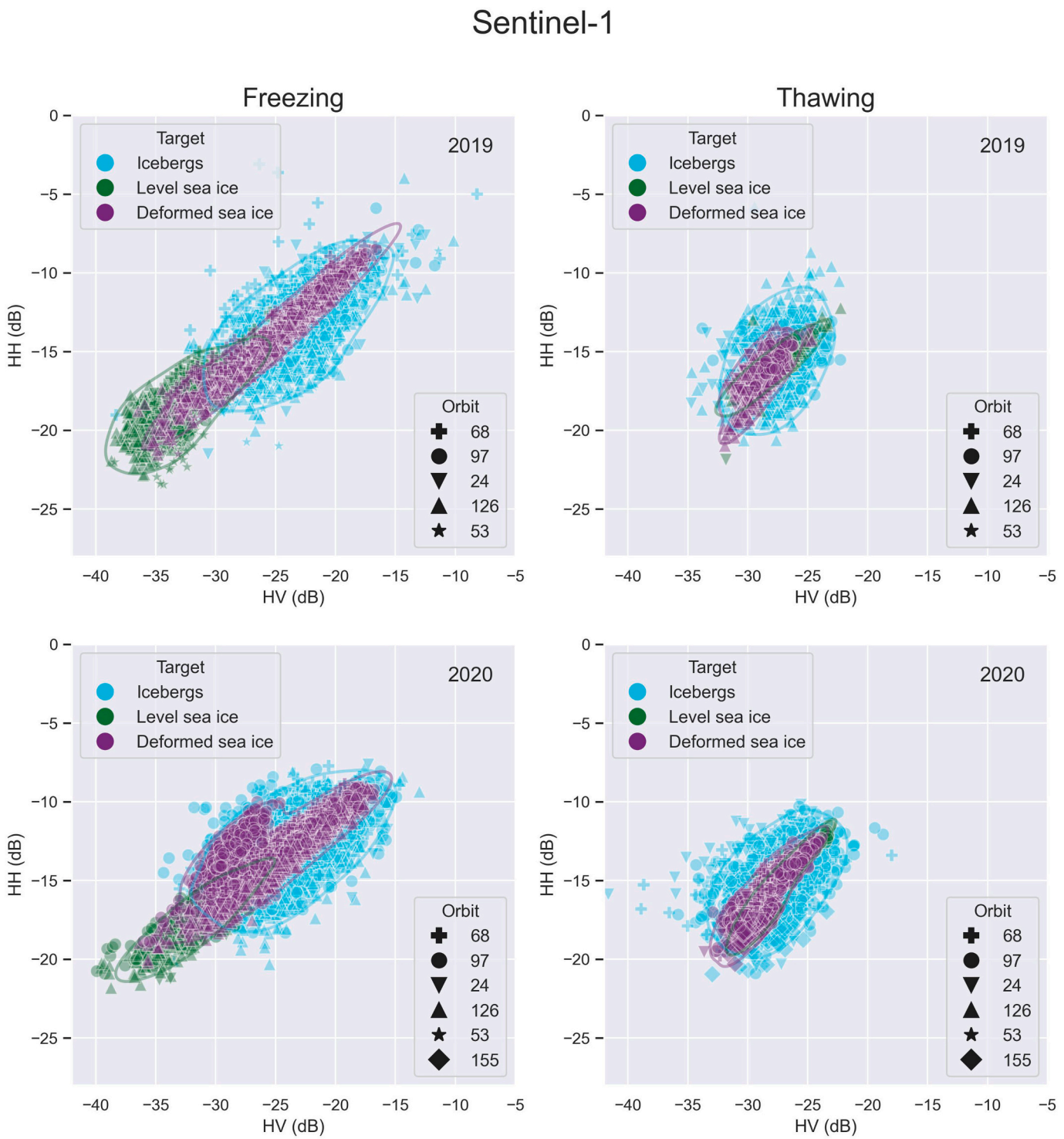

Fig. 7. Sentinel-1 backscattering intensities for all icebergs and their background of deformed or level ice for 2019 (top row), and 2020 (bottom row), and for both freezing (left) and thawing (right) conditions.

conditions, while the right column shows the data under thawing conditions. Fig. 8 is organized similarly for ALOS-2 (L-band).

It should be mentioned that since we merge data from different orbits without applying any form of incidence angle correction, we expect the scatter plots to exhibit a higher overall variance than if the data points were corrected to a common incidence angle. This is especially true for ALOS-2, which, as shown above, appears more sensitive to the incidence angle than C-band. To account for this, we have added orbit markers to the observations to make the interpretation easier.

In addition to the figures, we have also summarized the results for Sentinel-1 in Table 2 and for ALOS-2 in Table 3. Here, we show the slope (m) and Pearson correlation coefficient (ρ) of fitting a linear model to the data points, and additionally the mean (μ) and standard deviation (σ) are shown for HH and HV polarization respectively. The data have been separated into freezing and thawing seasons similarly to the figures and show the results for each of the three classes separately, i.e., icebergs (IB), level sea ice (LSI), and deformed sea ice (DSI).

Inspection of both the figures and the tables reveals that there is a

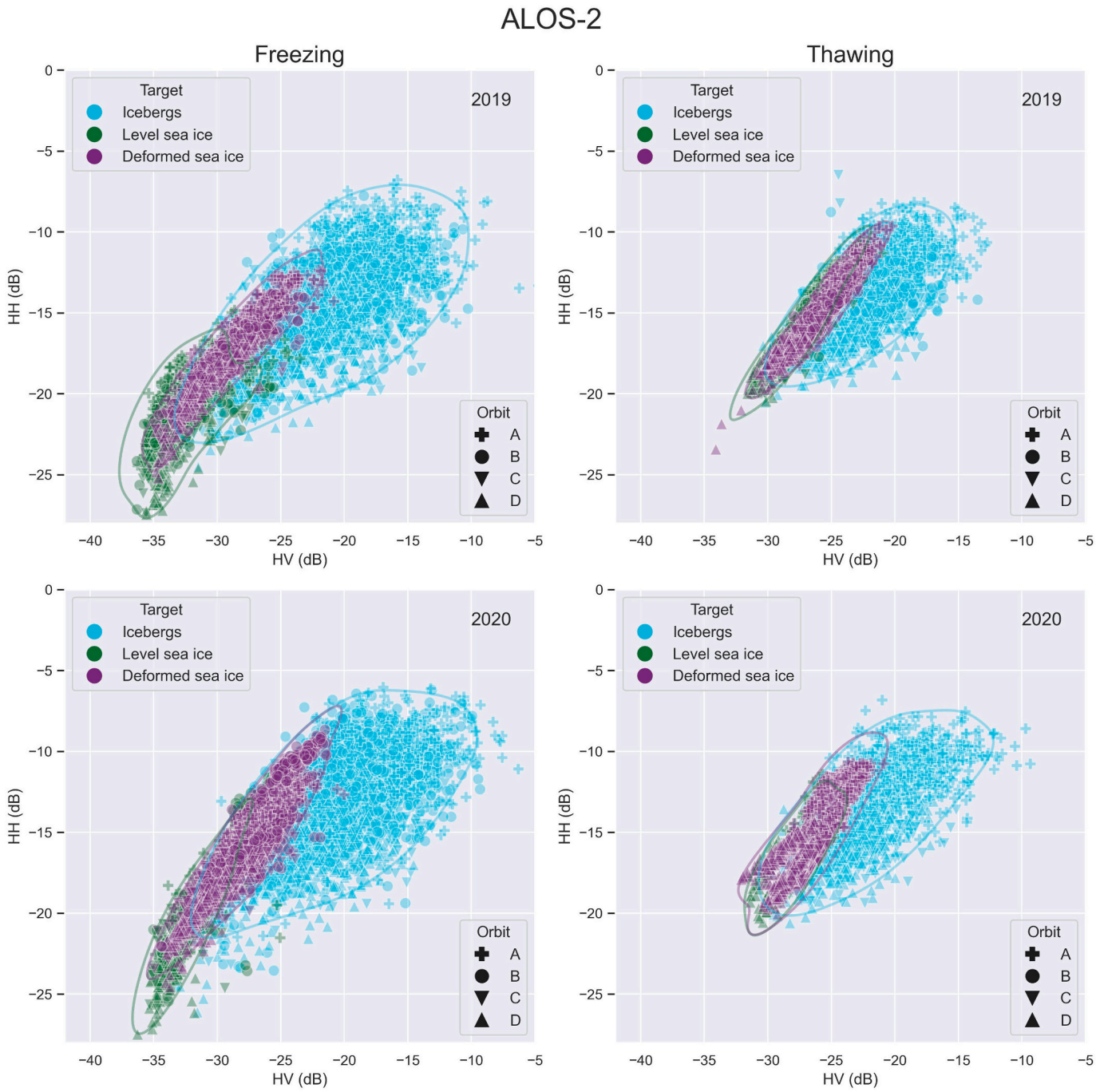

Fig. 8. ALOS-2 backscattering intensities for all icebergs and their background of deformed or level ice for 2019 (top row), and 2020 (bottom row), and for both freezing (left) and thawing (right) conditions.

high similarity between the data collected from 2019 and 2020. This is seen for both Sentinel-1 and ALOS-2, and for both freezing and thawing conditions. It is most evident for the mean backscatter (μ) and standard deviation (σ) in Tables 2 and 3. The mean backscatter typically varies around 1–2 dB for both C- and L-band, for both years, and seasons, and for all three classes. This is within a single standard deviation which is between 1 and 4 dB. These large similarities between the two years suggests that the results are of general validity in the AOI also for other years. However, inspection of the figures does reveal some minor inconsistencies. For Sentinel-1, we see a large subclass from orbit 97 in 2020 under freezing conditions, with lower HV and higher HH intensity than the average. Similarly, a subclass of higher HH scattering is seen for ALOS-2, freezing conditions for 2020, acquired from orbit B. These two cases are likely caused by precipitation, which is further detailed in Section 5.3 Other minor difference between the years can likely be attributed to the fact that the images used in the study cover slightly different periods, with different temporal gaps in the timeseries as seen in Figs. 5 and 6. In addition, it is expected that local ice conditions may vary slightly between the years, which could explain some of the differences between the years.

Both sea ice classes generally exhibit a strong correlation between HH and HV polarization. This is visible both in Figs. 7 and 8 and in Tables 2 and 3, with a correlation coefficient above 0.7 for both sea ice types and seasons for Sentinel-1, and above 0.6 for ALOS-2. The high correlation between HH and HV bands for level and deformed sea ice is consistent with results reported in the literature (Dierking, 2010;

Table 2
Main parameters characterizing the backscatter intensity for Sentinel-1. The slope (m), Pearson correlation coefficient (ρ), mean (μ) and standard deviation (σ) are calculated for each of the three classes icebergs (IB), level sea ice (LSI), and deformed sea ice (DSI), for 2019 and 2020. The results are separated according to freezing and thawing conditions.

Sentinel-1												
	2019						2020					
	Freezing			Thawing			Freezing			Thawing		
	IB	LSI	DSI	IB	LSI	DSI	IB	LSI	DSI	IB	LSI	DSI
m	0.46	0.49	0.65	0.38	0.58	0.68	0.36	0.52	0.47	0.36	0.89	0.84
ρ	0.66	0.73	0.97	0.38	0.89	0.70	0.58	0.88	0.85	0.46	0.92	0.86
μ_{hh}	−13.22	−18.65	−13.23	−15.57	−16.17	−16.79	−12.87	−17.70	−13.00	−15.06	−15.79	−16.52
μ_{hv}	−23.04	−33.25	−23.86	−27.49	−28.16	−29.21	−23.22	−32.01	−24.29	−27.46	−27.80	−29.06
σ_{hh}	1.99	1.59	2.49	1.81	1.06	1.18	1.83	1.85	1.84	1.77	2.00	1.54
σ_{hv}	2.85	2.37	3.72	1.82	1.64	1.21	2.98	3.10	3.34	2.27	2.07	1.58

Table 3
Main parameters characterizing the backscatter intensity for ALOS-2. The slope (m), Pearson correlation coefficient (ρ), mean (μ) and standard deviation (σ) are calculated for each of the three classes icebergs (IB), level sea ice (LSI), and deformed sea ice (DSI), for 2019 and 2020. The results are separated according to freezing and thawing conditions.

ALOS-2												
	2019						2020					
	Freezing			Thawing			Freezing			Thawing		
	IB	LSI	DSI	IB	LSI	DSI	IB	LSI	DSI	IB	LSI	DSI
m	0.45	0.63	0.81	0.53	1.05	0.94	0.46	1.23	1.02	0.51	0.94	0.95
ρ	0.65	0.63	0.92	0.68	0.94	0.95	0.65	0.86	0.93	0.70	0.79	0.84
μ_{hh}	−14.61	−21.58	−17.35	−14.16	−16.20	−15.10	−13.45	−20.43	−16.14	−13.81	−16.48	−15.16
μ_{hv}	−21.46	−33.29	−28.82	−22.82	−27.75	−25.97	−20.85	−32.01	−28.00	−22.40	−27.93	−26.52
σ_{hh}	2.99	1.97	2.11	2.24	2.26	1.90	3.02	3.37	2.74	2.50	2.30	2.26
σ_{hv}	4.38	1.97	2.42	2.91	2.03	1.93	4.25	2.36	2.50	3.47	1.94	2.00

Dierking and Wesche, 2014). The correlation for the iceberg class is much lower, with a correlation coefficient for Sentinel-1 between 0.58 and 0.66 for freezing conditions, and between 0.38 and 0.46 for thawing conditions. For ALOS-2, the correlation for the iceberg class is slightly higher, with values between 0.65 and 0.70 for both seasons. The lower correlation for icebergs may be explained by complex scattering mechanisms caused by the highly variable geometry at different spatial scales, which is typical for many icebergs. In our investigation, we did not separate icebergs according to their sizes and types (the latter cannot be characterized from satellite images). One has also to consider that the iceberg polygons obtained from Sentinel-2 images might not completely align with the positions of the SAR backscatter returns, causing additional variations in the results of the backscatter intensity. Another factor to consider is the varying window size used to estimate the average backscatter values. The iceberg backscatter is generally estimated in smaller windows than the sea ice backscatter as mentioned earlier, which will lead to a higher variance.

Under freezing conditions, we obtain a much higher correlation coefficient for deformed sea ice than for level sea ice. This is both evident in Figs. 7 and 8, and in Tables 2 and 3. For ALOS-2, the correlation coefficient is 0.63 for level sea ice and 0.92 for deformed sea ice for 2019, and 0.86 and 0.93 for 2020, while for Sentinel-1 the correlation coefficient is 0.73 for level sea ice and 0.97 for deformed sea ice for 2019. For 2020, the trend of higher correlation for deformed sea ice is not equally visible for Sentinel-1, with correlation coefficients of 0.88 and 0.85 for level and deformed sea ice respectively. This lower correlation for deformed sea ice in 2020 might be due to the influence of precipitation during acquisitions on orbit 97 mentioned earlier. In general, the lower correlation coefficient for level sea ice during freezing conditions might be caused by the overall lower backscatter intensity of this ice type, which is around -33 dB for both ALOS-2 and Sentinel-1 in the HV band. These low backscatter intensities are at the noise level (and below the nominal average NESZ for ALOS-2 as seen in Table 1), which decreases the linear correlation coefficient. For ALOS-2, the measurements also appear to show a cut-off of HV values around -35 dB as seen in the left row of Fig. 8 We do not know the exact reason, but the most presumable cause is that it is related to the noise level.

Regarding the influence of melt onset on the backscatter of the sea ice classes, the greatest impact for Sentinel-1 appears to be the increase in backscatter for level sea ice, with an increase of around 2 dB for the HH band and 5 dB for the HV band, and the decrease of backscatter from deformed sea ice, of around 3 dB for HH and 5 dB for HV. This means that the two sea ice classes converge towards the same average backscatter under thawing conditions, at around -16 dB for the HH band and -28 dB for the HV band, and with similar slopes and correlation coefficient as well. For Sentinel-1, the melt onset also gives rise to a lower variance of the sea ice classes. This can be attributed to an increase of scattering from larger brine-wetted snow grains on level ice and a slight decrease in backscatter from deformed (older) ice because of reduced penetration into the ice volume, all in all leading to similar backscatter from both level and deformed sea ice (Casey et al., 2016). As the stage of the melt advances later in the season, we expect that the wet ice surface gives rise to a dominance of surface scattering. The similarity of backscattering between the sea ice classes can also be seen in Fig. 2, where the two sea ice classes become indistinguishable in the two images acquired later in the season compared to the image acquired early in the season. A similar observation was reported by Yackel et al. (2007), where for melt onset, the backscatter for first-year ice (FYI) was reported as being higher than for multi-year ice (MYI) for C-band SAR. For ALOS-2, the level sea ice class shows an increase in backscatter after melt onset of around 5 dB for both HH and HV. The corresponding numbers for deformed sea ice are 1-2 dB for HH and 2-3 dB for HV. Hence the two sea ice classes become less separable also at L-band after melt onset, with similar mean backscatter, variance, and slope under melting conditions for the two sea ice types.

Looking at the iceberg class, there appears to be a smaller influence of thawing conditions on ALOS-2 imagery compared to Sentinel-1. For Sentinel-1, the mean backscatter for icebergs decreases by around 2 dB

for the HH band and 4 dB for the HV band at the onset of melting conditions, while for ALOS-2 the HH band is unaltered by the melt onset while the HV band shows a decrease around 1 dB after melt onset. The slope and correlation coefficient for ALOS-2 is also more stable for the iceberg class after the melt onset compared to Sentinel-1. This could be caused by the higher penetration depth of L-band, making ALOS-2 less influenced by wet snow or water on the iceberg's surfaces compared to C-band. For both Sentinel-1 and ALOS-2, there is a slight decrease in standard deviation after the onset of melt, which is most significant for ALOS-2.

Sentinel-1 shows a consistent large overlap between the iceberg and sea ice backscattered intensities (Fig. 7). For freezing conditions, the overlap is especially large between the iceberg and deformed sea ice class, while there is still good separation between the iceberg and level sea ice class. For thawing conditions, there is a large overlap between the iceberg class and both sea ice classes. These observations compare well with the observations from Section 4.1 and demonstrates that it is very difficult to determine intensity thresholds for separating sea ice and iceberg radar responses using C-band SAR. For ALOS-2, the intensities of the iceberg class are consistently shifted towards higher HV backscatter compared to both sea ice classes for both freezing and thawing conditions. This can also be seen in Fig. 2, where the iceberg in the subset is consistently visible as red (HV) blobs.

This enables us to separate icebergs and sea ice more easily using L-band than at C-band, suggesting that L-band is better suited for detecting icebergs in sea ice. Preferably the separation should be done using a combination of HH- and HV-polarizations. And separation is easier under freezing conditions.

4.3. CFAR results

The results of the CFAR detector outlined in Section 3.5 is shown in Tables 4 and 5 for Sentinel-1 and ALOS-2 respectively. In addition, a small subset of the results is shown in Fig. 9, giving an impression of the quality of automatic iceberg detection by separating the true positives (green), false detections (red), and missed detections (yellow).

We found that for 2019, Sentinel-1 has a decent precision (0.67) and recall (0.57) for icebergs in level sea ice, and a poor precision (0.21) and recall (0.07) for icebergs in deformed sea ice (Table 4). For 2020, the results are even worse with a precision and recall for level sea ice at 0.23 and 0.42 respectively, and 0.06 and 0.06 respectively for deformed sea ice. This is also reflected in the number of false positives and false negatives, with a very high number of false negatives in deformed sea ice for 2019, and a high number of both false positives and negatives for deformed sea ice in 2020. The results show that Sentinel-1 under some conditions performs well in detecting icebergs in level sea ice, although with a high number of false negatives in 2019 and a high number of false positives in 2020. For deformed sea ice, Sentinel-1 generally performs very poor, with a very low number of true positives compared to the number of false positives and negatives. This is also obvious from Fig. 9, where Sentinel-1 has not been able to detect any of the icebergs in deformed sea ice.

The results for ALOS-2 in Table 5 shows better results across all scores, with a precision above 0.9 for both sea ice types in 2019, and a decent recall as well. For 2020, the results are slightly worse, but still better than for Sentinel-1, with a precision above 0.75 and recall at 0.65 and 0.49 for level and deformed sea ice respectively. ALOS-2 thus shows much better performance for detecting icebergs in both level and deformed sea ice, with a much higher number of true positives, and lower number of false positives and negatives.

Table 4
Results of applying the CFAR algorithm to two Sentinel-1 (C-band) images from the spring of 2019 and 2020 respectively.

	Sentinel-1					
	2019-04-27			2020-04-27		
	Level SI	Deformed SI	Total	Level SI	Deformed SI	Total
FP	82	162	244	198	670	868
FN	126	543	669	83	721	804
TP	166	44	210	59	46	105
Precision	0.67	0.21	0.46	0.23	0.06	0.11
recall	0.57	0.07	0.24	0.42	0.06	0.12

Table 5
Results of applying the CFAR algorithm to two ALOS-2 (L-band) images from the spring of 2019 and 2020 respectively.

	ALOS-2					
	2019-04-27			2020-04-27		
	Level SI	Deformed SI	Total	Level SI	Deformed SI	Total
FP	13	26	39	20	127	147
FN	95	347	442	50	394	444
TP	196	241	437	92	373	465
Precision	0.94	0.90	0.92	0.82	0.75	0.76
recall	0.67	0.41	0.50	0.65	0.49	0.51

Although ALOS-2 shows significantly better results than Sentinel-1, a considerable number of icebergs were not detected, with the total number of false negatives being comparable with the number of true positives. Further investigation revealed that the detection accuracy increased with increasing iceberg size, and visual inspection of the results revealed that many of the missed detections were found in places where icebergs were located in clusters, as e.g., seen in the top right and right side of Fig. 9. This suggests that some of the false negatives could be due to the CFAR detector falsely interpreting spots of high areal iceberg densities as background clutter, thus lowering the probability of detection in these areas. These types of errors could be avoided in the future by truncating high intensity pixels (Tao et al., 2016). The clusters of icebergs often originate from a break-up of a single larger iceberg, where the broken pieces remain closely together because of the surrounding fast ice or because they are grounded. This will less likely occur for icebergs moving in drifting sea ice. Inspection of Fig. 9 also reveals that many of the missed detections are icebergs of medium size which means that perhaps the performance could be further increased by tuning the probability of false alarm rate or the window size of the CFAR detector. We expect that better performance can be achieved by applying the detector to the data in the original pixel spacing (25 m), instead of the down-sampled data (40 m), which we use here to match the Sentinel-1 resolution. Seen from the perspective of operational iceberg monitoring, the large number of missed detections gives cause for concern and needs to be investigated in more detail. This, however, was beyond the scope of this study.

5. Summary

Comparison of both the timeseries contrast plots (Figs. 5 and 6), and the scatterplots (Figs. 7 and 8), shows a large similarity between the data gathered from 2019 and 2020. This suggests that the results are of general validity for the investigated area, with some small inconsistencies which we attribute to the different meteorological conditions and temporal gaps in our timeseries.

Figures 5 to 8 and Tables 2 and 3 all suggest that Sentinel-1 (C-band) only offers a satisfactory separability between level sea ice and icebergs under freezing conditions and not under thawing conditions. Additionally, Sentinel-1 is not able to distinguish between icebergs and deformed sea ice at all, which also suggests that small floes of deformed sea ice embedded in level sea ice could be misinterpreted as icebergs when using C-band for iceberg detection.

ALOS-2 on the other hand, can distinguish between icebergs in both level and deformed sea ice, and although the performance is much higher under freezing conditions, the classes can still be separated under thawing conditions as well.

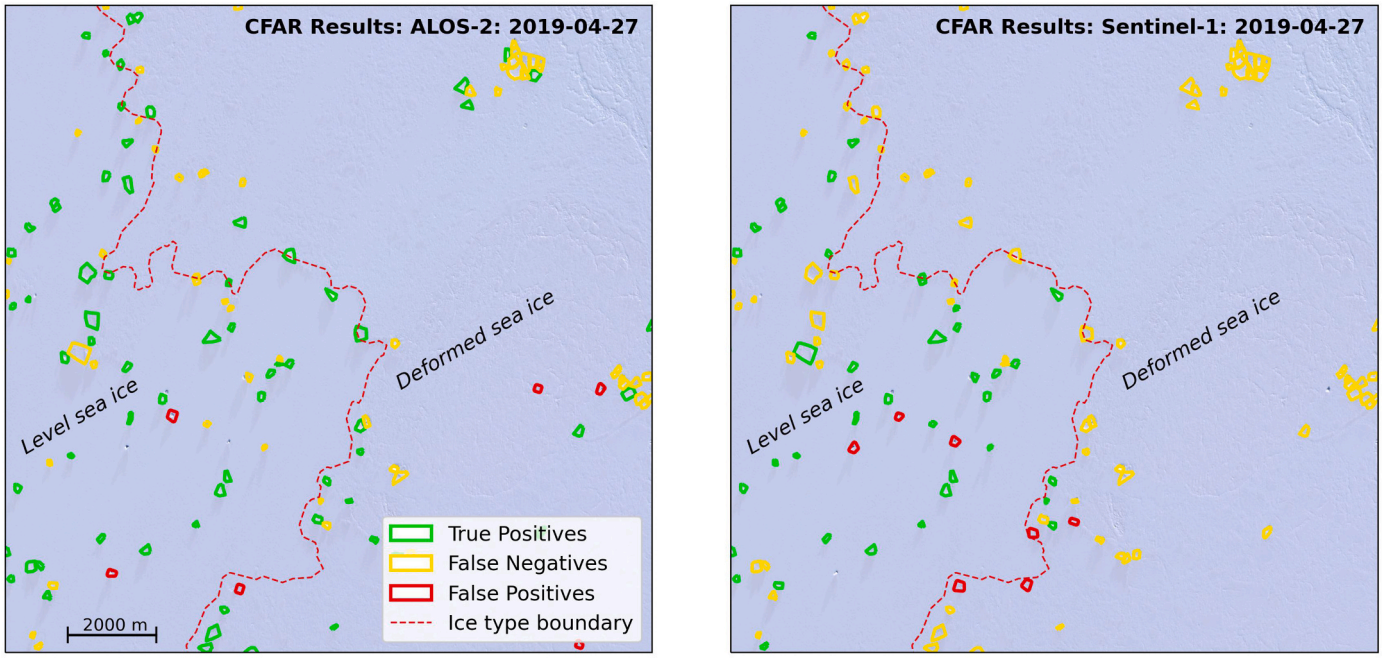

Fig. 9. Results of running the iceberg detection algorithms on the ALOS-2 L-band images (left), and the Sentinel-1C-band image (right) overlaid on a Sentinel-2 image. Detected icebergs are marked with green, false detections with red, and missed detections with yellow. (For interpretation of the references to colour in this figure legend, the reader is referred to the web version of this article.)

The results are further supported by comparing the performance of a CFAR detection algorithm run on two C-band and two L-band images all acquired during the spring. Here, we also saw that L-band offered a much better performance than C-band for detecting icebergs in sea ice. All in all, the results suggest that L-band SAR is superior for detecting icebergs in areas with sea ice if compared to C-band. Furthermore, to minimize misclassifications, a detector designed for finding icebergs in L-band SAR images should be based on a combination of HH- and HV-polarization rather than applying separate thresholds to the two polarizations.

6. Discussion

6.1. Automatic matching of the L-band time delay

Validating backscatter values from icebergs at L-band was only possible by considering time-delayed reflections. As noted in Section 3.3, the time delay depends on, e.g., geometry, dielectric properties, and internal structure of an iceberg, and the presence of water or wet snow on the surface. To account for the time delay when collecting validation data, we opted for a pragmatic approach by shifting the iceberg polygon down-range to a location that maximizes the HV backscatter return. An issue with this approach is that if iceberg radar returns are too weak to be distinguishable from the surrounding sea ice, we risk finding and including local maxima caused by sea ice scattering, and thus artificially increasing the average contrast, especially during the thawing season, when the sea ice backscatter for level sea ice is increased. This will give rise to a bias of the HV backscatter for icebergs – moving some of the ALOS-2 iceberg samples towards the right in Fig. 8, which will influence the overall contrast. To account for this, we performed a visual inspection of the SAR images with the focus on the time-delayed polygons of icebergs that were determined from the Sentinel-2 image. This inspection revealed that a majority of the corrected polygons overlapped with distinct backscatter maxima that could be distinguished from the surrounding sea ice backscatter, and therefore was interpreted as coming from the icebergs. Based on the visual inspection, we have confidence that this bias does not change the overall conclusion of the results; namely that L-band is preferable to C-band.

6.2. Variation of contrast as a function of incidence angle for L-band

From Fig. 6 it is evident that the backscatter contrast and the orbit of ALOS-2 are related, since orbits A and B exhibit a generally higher contrast than orbits C and D. This is most likely caused by the differences in incidence angles covering the AOI between the orbits (see Fig. 1) and different sensitivities (slopes) of the sea ice and the iceberg backscatter to changes in incidence angle. The fact that we do not see a similar response at C-band may indicate that the sensitivities of the backscattered intensities from sea ice and icebergs are similar, causing less variation in the contrast for varying incidence angles. As mentioned in Section 2.2, the ALOS-2 data were delivered without incidence angle information. Therefore, a thorough investigation of the influence of incidence angle on the contrast at L-band cannot be performed at this stage.

6.3. Influence of precipitation

In Fig. 7, for Sentinel-1 during freezing conditions in 2020, a cluster of deformed sea ice data from orbit 97 is recognized that reveals an increase in HH and a decrease in HV compared to the other observations. A detailed investigation showed that these outliers come from an image that was acquired on May 25th, 2020, which coincides with a precipitation event observed at the Danmarkshavn weather station (Fig. 1) on May 24th, when 24 mm of precipitation was recorded. This appears to have influenced the ALOS-2 observations as well, with an increase in both HH and HV. This can be recognized in Fig. 8 for orbit B. The corresponding image was acquired on May 25th. Based on the temperature on May 24th, 2020, the precipitation was likely in the form of rain or possibly wet snow.

The rest of the period (April–July) for both 2019 and 2020 saw very little precipitation. The monthly average for April–July 2019 was below 10 mm, and for 2020 both April and June were below 10 mm, whereas in May and July the monthly precipitation was 32 and 21 mm, respectively.

6.4. Influence of acquisition times

The Sentinel-1 overpasses covering our AOI took place in the morning (08:00–08:30 UTC) and the ALOS-2 overpasses in the early afternoon (13:45–14:30 UTC), i.e., with a 6-h time difference. The temperature variation in the area (shown as the shaded red area in Figs. 5 and 6) is at around 6oC for a 24-h period. With this relatively large temperature difference, Sentinel-1 images were most probably acquired under conditions where it is several degrees colder than during ALOS-2 data takes. In the transition period between freezing and thawing conditions, C-band images may have been acquired during freezing, and L-band during thawing conditions. However, since quick temperature changes will mainly influence the surface layer of the snow, and since L-band is less sensitive to the surface layer, we expect that this temperature difference will not significantly affect our results.

6.5. Advanced melt

There are some minor indications that the contrast for C-band increases during advanced stages of melt. This can be observed in Fig. 5, where the contrast towards the end of the time series is around 2 dB for both polarizations and for both level and deformed ice. This can also be observed in Fig. 2 (for the 2019-07-08 acquisition), where the icebergs at C-band appear to have a slightly higher backscatter level than the sea ice, although still exhibiting a lower contrast than at L-band. However, due to the break-up of the fast ice at the end of July for both 2019 and 2020, we could not investigate the development of contrast further into the more advanced stages of the melt.

6.6. Operational iceberg detection

As we saw in Section 4.1, some orbits appeared to give a higher contrast between the icebergs and sea ice classes compared to other orbits, especially for ALOS-2 (L-band). Therefore, we expect that the orbit selection influences the performance of the CFAR detector. Due to the lack of incidence angle data for the ALOS-2 images we could not investigate this effect in depth. For our CFAR detection results, the first ALOS-2 image was acquired from orbit D, and the second from orbit B. Here, orbit D results in a relatively low contrast between icebergs and sea ice, while B gives a high contrast. For comparison, both Sentinel-1 images were acquired from orbit 126, which were shown to give a relatively high contrast, although the influence of the acquisition orbit is not so pronounced at C-band compared to L-band. Since the performance of L-band was much higher than C-band for both orbits, we do not expect that the conclusions change significant for acquisitions from different orbits.

It should, however, be mentioned that the equivalent number of looks (ENL) is different for the two sensors, which might affect the results. The ENL of Sentinel-1 in EW mode is around 10.7 (Bourbigot et al., 2016), whereas the ENL for ALOS-2 is not provided but probably smaller than the multi-look value of 6 (Table 1). This will likely affect the results as the ALOS-2 images are expected to have a slightly higher level of speckle noise. Nevertheless, the L-band image is proving to be clearly superior to C-band, so we do not expect that an ENL similar for both sensors change the results significantly.

6.7. Extending the results for detecting icebergs in drift ice

To accurately validate our results and consider temporal variations of radar backscattering, we were restricted to using a dataset consisting of stationary icebergs in land-fast sea ice because optical and radar images over a given area were only available with considerable time gaps. Nevertheless, we expect that our conclusions are also valid for detecting icebergs in drifting sea ice – at least for the sea ice types that we have focused on in this study. However, special cases may require additional analyses, such as icebergs embedded in brash ice, pancake ice, or in ice covered with frost flowers.

7. Conclusion

In this study, we have compared a time series of dual-pol L- and C-band SAR images acquired over the fast-ice at Belgica Bank, North-Eastern Greenland, during 2019 and 2020 with the objective to assess the detectability of medium and large icebergs under different seasonal conditions. Using Sentinel-2 as an independent reference, backscattering intensities from several hundred stationary icebergs, as well as from the sea ice surrounding them, were extracted, and the intensity contrast between level and deformed sea ice, on one hand, and icebergs, on the other hand, was calculated for the freezing and thawing seasons.

The results showed that at both freezing and thawing conditions, C-band cannot differentiate between deformed sea ice and icebergs. Icebergs in level ice can mostly be detected in C-band images acquired under freezing conditions; however, small, deformed floes in level sea ice might be misinterpreted as icebergs. The usefulness of Sentinel-1 for mapping icebergs in icy waters is therefore limited, and we expect similar results for other C-band satellites such as RADARSAT.

L-band, on the other hand, reveals a considerable better separation of icebergs in both deformed and level sea ice under freezing conditions. Under thawing conditions, the L-band contrast generally decreases, but a high number of icebergs still exhibit a sufficiently high contrast for a successful detection. Furthermore, we observed a significant incidence angle dependency of the iceberg and sea ice contrast at L-band which suggests that icebergs should be mapped at low incidence angles. Overall, L-band SAR offers a large advantage over C-band for mapping medium and large icebergs in sea ice.

Our findings were verified by applying a simple CFAR detection algorithm to two pairs of C- and L-band images for which 879 and 909 icebergs for the first and second pair, respectively, were identified in a corresponding Sentinel-2 image for validation. Using C-band, we found that around 24% of the icebergs were accurately detected, against 50% detected icebergs using L-band for the first image pair, while the second image pair showed only 11% detected icebergs for C-band and 51% for L-band. Additionally, C-band showed around six times as many false detections compared to L-band. However, we also noted a large number of missed icebergs at both frequencies, especially at locations of iceberg clusters This, however, may be largely attributed to the simplicity of the test, with a fixed clutter geometry. We expect that more advanced methods may solve this problem.

By using a large number of icebergs as validation data, and a time series of images covering the freezing/thawing seasons for two separate years, we expect that the results can be generalized for most Arctic conditions. The results shown here demonstrate that icebergs in regions with sea ice should be preferably detected using L-band SAR at low incidence angles. Further, an iceberg detector should be designed to use both HH and HV polarization for achieving best results. Our findings will help advancing the monitoring of icebergs in sea ice using SAR, which is beneficial to both maritime safety and for evaluating the impact of ice discharge on the oceans.

Funding

This research was funded by CIRFA partners and the Research Council of Norway (grant number 237906).

CRediT authorship contribution statement

Laust Færch: Writing – original draft, Visualization, Software, Methodology, Formal analysis. **Wolfgang Dierking:** Writing – review & editing, Supervision, Methodology, Conceptualization. **Nick Hughes:** Writing – review & editing, Supervision, Resources. **Anthony P. Doulgeris:** Writing – review & editing, Supervision, Methodology.

Declaration of competing interest

The authors declare that they have no known competing financial interests or personal relationships that could have appeared to influence the work reported in this paper.

Data availability

Data will be made available on request.

Acknowledgement

ALOS-2/PALSAR-2 data are provided by JAXA through the 2019 to 2022 mutual cooperation project between ESA and JAXA on Using Synthetic Aperture Radar Satellites in Earth Science and Applications. We are also thankful for the support received by the ESA and the Ministry of Science and Technology (MOST) of the P.R. China through the Dragon-5 cooperation. And we are also thankful for the discussions with our Chinese partners.

References

Achanta, R., Shaji, A., Smith, K., Lucchi, A., Fua, P., Süsstrunk, S., 2012. SLIC Superpixels compared to state-of-the-art Superpixel methods. IEEE Trans. Pattern Anal. Mach. Intell. 34 (11), 2274–2282. https://doi.org/10.1109/TPAMI.2012.120.

Amdal, F., Hughes, N., 2022. Multi-Sensor Ice Analysis Data: Analysis for Belgica Bank, North East Greenland 2019-20 (1.0.0) [Data set]. Zenodo. https://doi.org/10.5281/zenodo.7053975.

Arndt, E.J., Jokat, W., Dorschel, B., Myklebust, R., Dowdeswell, J.A., Evans, J., 2015. A new bathymetry of the Northeast Greenland continental shelf: constraints on glacial and other processes. Geochem. Geophys. Geosyst. 18, 1541–1576. https://doi.org/10.1002/2015GC005931.Received.

Bailey, J., Marino, A., 2020. Quad-polarimetric multi-scale analysis of icebergs in ALOS-2 SAR data: a comparison between icebergs in west and East Greenland. Remote Sens. 12 https://doi.org/10.3390/rs12111864.

Bailey, J., Marino, A., Akbari, V., 2021. Comparison of target detectors to identify icebergs in quad-Polarimetric L-band synthetic aperture radar data. Remote Sens. 13.

Barbat, M.M., Rackow, T., Hellmer, H.H., Wesche, C., Mata, M.M., 2019. Three years of near-coastal Antarctic iceberg distribution from a machine learning approach applied to SAR imagery. J. Geophys. Res. Ocean. 124, 6658–6672. https://doi.org/10.1029/2019JC015205.

Bigg, G., 2015. Icebergs: Their Science and Links to Global Change. Cambridge University Press, Cambridge. https://doi.org/10.1017/CBO9781107589278.

Bourbigot, M., Johnson, H., Piantanda, R., 2016. Sentinel-1 Product Definition. ESA. https://sentinels.copernicus.eu/web/sentinel/user-guides/sentinel-1-sar/document-library/-/asset_publisher/1dO7RF5fJMbd/content/sentinel-1-product-definition (last access: 6 December 2023).

Braakmann-Folgmann, A., Shepherd, A., Hogg, D., Redmond, E., 2023. Mapping the extent of giant Antarctic icebergs with deep learning. Cryosph. 17, 4675–4690. https://doi.org/10.5194/tc-17-4675-2023.

Bügelmayer, M., Roche, D.M., Renssen, H., 2015. How do icebergs affect the Greenland ice sheet under pre-industrial conditions? - a model study with a fully coupled ice-sheet-climate model. Cryosphere 9, 821–835. https://doi.org/10.5194/tc-9-821-2015.

Buus-Hinkler, J., Qvistgaard, K., Krane, K.A.H., 2014. Iceberg number density - reaching a full picture of the Greenland waters. Int. Geosci. Remote Sens. Symp. 270–273. https://doi.org/10.1109/IGARSS.2014.6946409.

Casey, J.A., Howell, S.E.L., Tivy, A., Haas, C., 2016. Separability of sea ice types from wide swath C- and L-band synthetic aperture radar imagery acquired during the melt season. Remote Sens. Environ. 174, 314–328. https://doi.org/10.1016/j.rse.2015.12.021.

Copernicus Marine Service, 2023. SAR Sea Ice Berg Concentration and Individual Icebergs Observed with Sentinel-1. 10.48670/moi-00129.

Danish Meteorological Institute, 2023. Vejrarkiv. https://www.dmi.dk/vejrarkiv/ (Accessed 2023-08-10).

Das, A., Kumar, R., Rosen, P., 2021. Nisar mission overview and updates on ISRO science plan. In: 2021 IEEE India Geosci. Remote Sens. Symp. InGARSS 2021 - Proc, pp. 269–272. https://doi.org/10.1109/InGARSS51564.2021.9791979.

Davidson, M., Gebert, N., Giulicchi, L., 2021. ROSE-L – the L-band SAR mission for copernicus. In: Proc. Eur. Conf. Synth. Aperture Radar, EUSAR 2021-March, pp. 236–237.

Dierking, W., 2010. Mapping of different sea ice regimes using images from sentinel-1 and ALOS synthetic aperture radar. IEEE Trans. Geosci. Remote Sens. 48, 1045–1058. https://doi.org/10.1109/TGRS.2009.2031806.

Dierking, W., 2020. In: Di Martino, G., Iodice, A. (Eds.), Sea Ice And Icebergs. Maritime Surveillance with Synthetic Aperture Radar. Institution of Engineering and Technology, p. 346. ISBN 9781785616013. https://doi.org/10.1049/SBRA521E.

Dierking, W., Davidson, M., 2020. Enhanced Sea ICE monitoring at L- and C-bands using Rose-L and Sentinel-1. Int. Geosci. Remote Sens. Symp. 4059–4060 https://doi.org/10.1109/IGARSS39084.2020.9323886.

Dierking, W., Wesche, C., 2014. C-band radar polarimetry - useful for detection of icebergs in sea ice? IEEE Trans. Geosci. Remote Sens. 52, 25–37. https://doi.org/10.1109/TGRS.2012.2234756.

Evans, B., Faul, A., Fleming, A., Vaughan, D.G., Hosking, J.S., 2023. Unsupervised machine learning detection of iceberg populations within sea ice from dual-polarisation SAR imagery. Remote Sens. Environ. 297, 113780 https://doi.org/10.1016/j.rse.2023.113780.

Færch, L., Dierking, W., Hughes, N., Doulgeris, A.P., 2023. A comparison of CFAR object detection algorithms for iceberg identification in L-and C-band SAR imagery of the Labrador Sea. Cryosph. 17, 5335–5355.

Ferdous, M.S., McGuire, P., Power, D., Johnson, T., Collins, M.J., 2018. A comparison of numerically modelled iceberg backscatter signatures with Sentinel-1 C-band synthetic aperture radar acquisitions. Can. J. Remote. Sens. 44, 232–242. https://doi.org/10.1080/07038992.2018.1495554.

Ferdous, M.S., Himi, U.H., McGuire, P., Power, D., Johnson, T., Collins, M.J., 2019. C-band simulations of melting icebergs using GRECOSAR and an em model: varying wind conditions at lower beam mode. IEEE J. Sel. Top. Appl. Earth Obs. Remote Sens. 12, 5134–5146. https://doi.org/10.1109/JSTARS.2019.2954847.

Gill, R.S., 2001. Operational detection of sea ice edges and icebergs using SAR. Can. J. Remote. Sens. 27, 411–432. https://doi.org/10.1080/07038992.2001.10854884.

Gillies, S., et al., 2013. Rasterio: geospatial raster I/O for Python programmers. URL. https://github.com/rasterio/rasterio. Giraldez, 2004.

Giraldez, Alberto E., 2004. SAOCOM-1 Argentina L-band SAR mission overview. ESA Special Publication 565, 27.

Gray, A.L., Arsenault, L.D., 1991. Time-delayed reflections in L-band synthetic aperture radar imagery of icebergs. IEEE Trans. Geosci. Remote Sens. 29, 284–291. https://doi.org/10.1109/36.73670.

Guo, W., Itkin, P., Lohse, J., Johansson, M., Doulgeris, A.P., 2022. Cross-platform classification of level and deformed sea ice considering per-class incident angle dependency of backscatter intensity. Cryosphere 16, 237–257. https://doi.org/10.5194/tc-16-237-2022.

Haas, C., 2001. The seasonal cycle of ERS scatterometer signatures over perennial Antartic Sea ice and associated surface ice properties and processes. Ann. Glaciol. 33, 69–73. https://doi.org/10.3189/172756401781818301.

Harris, C.R., Millman, K.J., van der Walt, S.J., Gommers, R., Virtanen, P., Cournapeau, D., Wieser, E., Taylor, J., Berg, S., Smith, N.J., Kern, R., Picus, M., Hoyer, S., van Kerkwijk, M.H., Brett, M., Haldane, A., del Río, J.F., Wiebe, M., Peterson, P., Gérard-Marchant, P., Sheppard, K., Reddy, T., Weckesser, W., Abbasi, H., Gohlke, C., Oliphant, T.E., 2020. Array programming with NumPy. Nature 585, 357–362. https://doi.org/10.1038/s41586-020-2649-2.

Hughes, N.E., Wilkinson, J.P., Wadhams, P., 2011. Multi-satellite sensor analysis of fast-ice development in the Norske Øer ice barrier, Northeast Greenland. Ann. Glaciol. 52, 151–160. https://doi.org/10.3189/172756411795931633.

International Ice charting Working Group, 2019. Task Team 8: Mariner Training Requirement. Technical Report. https://nsidc.org/sites/nsidc.org/files/files/noaa/iicwg/2019/IICWG_Mariner_Survey_Intermediate_Report.pdf (Accessed 2023-08-10).

Jakobsson, M., Mayer, L.A., Bringensparr, C., et al., 2020. The international bathymetric chart of the Arctic Ocean version 4.0. Sci Data 7, 176. https://doi.org/10.1038/s41597-020-0520-9.

JAXA, 2012. ALOS-2/PALSAR-2 Level 1.1/1.5/2.1/3.1 CEOS SAR Product Format Description. Technical Report. https://www.eorc.jaxa.jp/ALOS-2/en/doc/fdata/PALSAR-2_xx_Format_CEOS_E_r.pdf (Accessed 2023-08-10).

Jordahl, K., 2014. GeoPandas: Python Tools for Geographic Data. URL. https://github.com/geopandas/geopandas.

Kankaku, Y., Suzuki, S., Osawa, Y., 2013. ALOS-2 mission and development status. Int. Geosci. Remote Sens. Symp. 2396–2399 https://doi.org/10.1109/IGARSS.2013.6723302.

Kim, J., Kim, D., Kim, S., 2011. Iceberg Detection using full-polarimetric RADARSAT-2 SAR Data in West Antarctica Jin-Woo, 2011. In: 3rd International Asia-Pacific Conference on Synthetic Aperture Radar (APSAR). IEEE, pp. 236–239.

Koo, Y., Xie, H., Mahmoud, H., Iqrah, J.M., Ackley, S.F., 2023. Automated detection and tracking of medium-large icebergs from Sentinel-1 imagery using Google Earth Engine. Remote Sens. Environ. 296, 113731 https://doi.org/10.1016/j.rse.2023.113731.

Liu, C., 2015. A Dual-Polarization Ship Detection Algorithm. Defence Research and Development Canada. Ottawa, ON, Canada, Ottawa Research Centre.

Mahoney, A.R., 2018. Landfast Sea Ice in a Changing Arctic. Arctic report card, 99. https://arctic.noaa.gov/report-card/report-card-2018/landfast-sea-ice-in-a-changing-arctic/ (Accessed 2023-08-10).

Mankoff, K.D., Solgaard, A., Colgan, W., Ahlstrøm, A.P., Abbas Khan, S., Fausto, R.S., 2020. Greenland ice sheet solid ice discharge from 1986 through March 2020. Earth Syst. Sci. Data 12, 1367–1383. https://doi.org/10.5194/essd-12-1367-2020.

Marino, A., 2018. Iceberg detection with L-band ALOS-2 data using the Dual-Pol Ratio Anomaly Detector. In: Int. Geosci. Remote Sens. Symp. 2018-July, pp. 6067–6070. https://doi.org/10.1109/IGARSS.2018.8519206.

Marino, A., Dierking, W., Wesche, C., 2016. A depolarization ratio anomaly detector to identify icebergs in sea ice using dual-polarization SAR images. IEEE Trans. Geosci. Remote Sens. 54, 5602–5615. https://doi.org/10.1109/TGRS.2016.2569450.

Marson, J.M., Gillard, L.C., Myers, P.G., 2021. Distinct Ocean responses to Greenland's liquid runoff and iceberg melt. J. Geophys. Res. Ocean. 126, 1–18. https://doi.org/10.1029/2021JC017542.

Mazur, A.K., Wåhlin, A.K., Krężel, A., 2017. An object-based SAR image iceberg detection algorithm applied to the Amundsen Sea. Remote Sens. Environ. 189, 67–83. https://doi.org/10.1016/j.rse.2016.11.013.

Oliver, C., Quegan, S., 2004. Understanding Synthetic Aperture Radar Images. SciTech Publishing Inc., Raleigh, NC 27613 (ISBN 1-891121-31-6.).

Power, D., Youden, J., Lane, K., Randell, C., Flett, C.R.D., 2001. Iceberg detection capabilities of radarsat synthetic aperture radar. Can. J. Remote. Sens. 27, 476–486. https://doi.org/10.1080/07038992.2001.10854888.

Rignot, E., Echelmeyer, K., Krabill, W., 2014. Penetration Depth of Interferometric Synthetic-aperture Radar Signal in Snow and Ice Penetration Depth of Interferometric Synthetic-aperture Radar signals in SNOW and Ice. https://doi.org/10.1029/2000GL012484.

Sandven, S., Babiker, M., Kloster, K., 2007, April. Iceberg observations in the Barents Sea by radar and optical satellite images. In: Proceedings of the ENVISAT Symposium, Montreux, Switzerland (pp. 23-27).

Soldal, I.H., Dierking, W., Korosov, A.A., Marino, A., 2019. Automatic detection of small icebergs in fast ice using satellite wide-swath SAR images. Remote Sens. 11, 1–24. https://doi.org/10.3390/rs11070806.

Tao, D., Doulgeris, A.P., Brekke, C., 2016. A segmentation-based CFAR detection algorithm using truncated statistics. IEEE Trans. Geosci. Remote Sens. 54, 2887–2898. https://doi.org/10.1109/TGRS.2015.2506822.

van der Walt, Stéfan, Schönberger, Johannes L., Nunez-Iglesias, Juan, Boulogne, François, Warner, Joshua D., Yager, Neil, Gouillart, Emmanuelle, Yu, Tony, the scikit-image contributors, 2014. scikit-image: Image processing in Python. https://doi.org/10.7717/peerj.453.

Wesche, C., Dierking, W., 2012. Iceberg signatures and detection in SAR images in two test regions of the Weddell Sea, Antarctica. J. Glaciol. 58, 325–339. https://doi.org/10.3189/2012J0G11J020.

Wesche, C., Dierking, W., 2012. Iceberg signatures and detection in SAR images in two test regions of the Weddell Sea, Antarctica. J. Glaciol. 58, 325–339. https://doi.org/10.3189/2012J0G11J020.

Willis, C.J., Macklin, J.T., Partington, K.C., Teleki, K.A., Rees, W.G., Rees, W.G., 1996. Iceberg detection using ers-1 synthetic aperture radar. Int. J. Remote Sens. 17, 1777–1795. https://doi.org/10.1080/01431169608948739.

Wolken, G.J., et al., 2020. Glaciers and Ice Caps Outside Greenland. Arctic Report Card. https://arctic.noaa.gov/report-card/report-card-2020/glaciers-and-ice-caps-outside-greenland/.

Yackel, J.J., Barber, D.G., Papakyriakou, T.N., Breneman, C., 2007. First-Year Sea ice spring melt transitions in the Canadian Arctic archipelago from time-series synthetic aperture radar data, 1992–2002. Hydrol. Process. 21 https://doi.org/10.1002/hyp.

Zakharov, I., Power, D., Howell, M., Warren, S., 2017. Improved detection of icebergs in sea ice with RADARSAT-2 polarimetric data. In: Int. Geosci. Remote Sens. Symp. 2017-July, pp. 2294–2297. https://doi.org/10.1109/IGARSS.2017.8127448.

/8

Paper III: Detecting Icebergs in Sea Ice using a Multiscale CFAR Algorithm

Færch, L., Dierking, W., Hughes, N., and Doulgeris, A. P. Submitted to IEEE Journal of Selected Topics in Applied Earth Observations and Remote Sensing on June 20th, 2024.

Detecting Arctic Icebergs in Sea Ice in L-band SAR Images Using a Multiscale CFAR Algorithm

Laust Færch, Wolfgang Dierking, Nick Hughes, Anthony P. Doulgeris, *Senior Member*

***Abstract*—This study introduces a multiscale extension of the well-known Constant False Alarm-Rate outlier detection method and shows its application to iceberg detection using Synthetic Aperture Radar images. The suggested approach offers the possibility to accurately detect single objects or clusters of icebergs embedded in sea ice. The approach was tested on 8 L-band dual-pol Synthetic Aperture Radar images acquired at various incidence angles and compared against a conventional single-scale CFAR approach. The test area contained several hundred icebergs, with ground-truth iceberg locations derived from optical satellite images serving as validation. The results reveal that the multiscale approach in general improves the detection performance for icebergs of all sizes with an increase in both recall and precision. In addition, the suggested multiscale method improves the estimation of the total iceberg area compared to a single-scale method. The results demonstrate the feasibility of using a multiscale outlier detection method on L-band SAR images for the operational detection of icebergs in sea ice using earth observation.**

***Index Terms*—Arctic, Iceberg Detection, SAR, L-band, CFAR.**

I. Introduction

DETECTION and mapping of icebergs in the Arctic is an important application within earth observation. Icebergs can pose a risk to maritime traffic and offshore infrastructure and can impact the oceanography of their local environment when melting. To carry out operational iceberg detection, remote sensing using Synthetic Aperture Radar (SAR) is needed to cover the large and remote region of the Arctic. In open water, detection is normally carried out using C-band SAR sensors such as from the RADARSAT or Sentinel-1 missions. Arctic icebergs, which are normally a few hundred meters in length, are typically detected using local adaptive outlier methods such as the constant false alarm rate (CFAR) approach, in particular for operational purposes. CFAR detectors generally work well for icebergs in open water since icebergs tend to exhibit a higher backscattering intensity than the ocean, and can therefore be recognized as bright spots against a darker background [1], [2]. However, earlier work [3]–[5] has suggested that using C-band sensors for the detection of icebergs in areas with a high sea ice concentration might be problematic, as there is a large overlap in backscattering coefficients of icebergs and sea ice, making separation difficult. L-band SAR is expected to provide an improved separation between sea ice and icebergs, given its larger penetration depth [6], [7]. Although L-band SAR data have been very sparse in the past, new missions such as the Argentinian SAOCOM-1 satellite, and the NASA/ISRO NISAR satellite will increase the data availability. In addition, a future ESA mission called Radar Observation System for Europe at L-band (ROSE-L) will offer daily images of the Arctic at a resolution better than what is currently available from operationally used imaging modes of recent C-band systems [8]. These L-band missions are expected to enable the operational detection of icebergs in areas with a high sea ice concentration, benefitting both maritime safety and environmental applications in the Arctic.

One issue with the classical CFAR approach is that the algorithm needs pre-defined window sizes. These are typically tailored according to the expected sizes and areal densities of icebergs in the region where they are applied. For current operational systems, defining these window sizes is mainly limited by the variation of the background clutter and the distance between neighboring icebergs. In the Arctic, the iceberg sizes are typically not a limitation, as large icebergs only take up a few pixels in the SAR image. Small icebergs below the resolution limit and with low backscattering levels are often undetectable. However, the increasing resolution of upcoming missions offers the possibility of more detail, and thus larger variation between the smallest and largest icebergs in an image. Further, this size difference will potentially be larger closer to the calving sites, which can contain a higher number of very large icebergs ($>$ 220 meters) that would otherwise break up in the open ocean.

In this study, we introduce a simple multiscale extension to the well-known CFAR approach. Here, a CFAR detector is applied to multiple down-scaled versions of the original image, thereby being able to detect icebergs of varying sizes. The multiscale extension is tested on 8 different dual-band L-band scenes acquired over an area of interest (AOI) in North-Eastern Greenland consisting of hundreds of icebergs embedded in landfast ice. The images are acquired at varying incidence angles and ice conditions to test the detection performance in different situations.

This paper is organized as follows. Section II presents the study area and data used, as well as outlining the background of CFAR detection, and presenting the implementation details of the methods used. Section III presents the results and a short discussion, and Section IV the conclusion.

Manuscript received April 19, 2021; revised August 16, 2021.

0000–0000/00$00.00 © 2021 IEEE

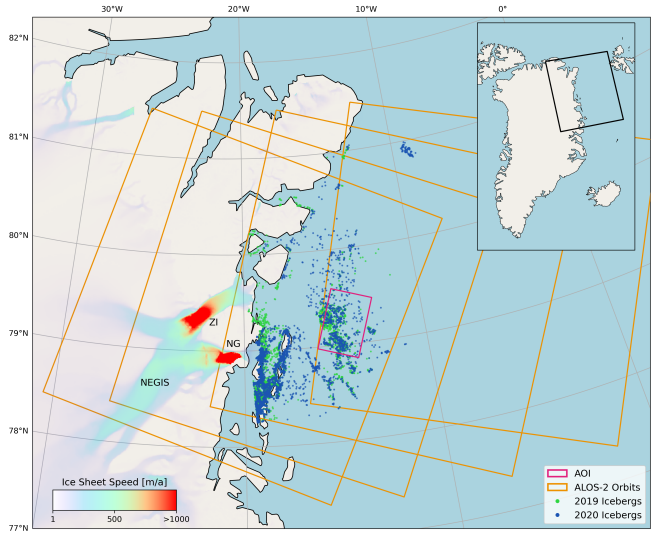

Fig. 1. Overview of the study area. Only icebergs within the AOI were used for this study. The ice sheet speed is taken from [9]. The Northeast Greenland Ice Stream (NIGIS), Zachariae Isstrøm (ZI), and the Nioghalvfjerdsfjord Gletcher (NG) are marked on the map.

II. Data and Methods

A. Study Area

Our study area covers a section (approximately 3500 km^2) of Belgica Bank, North-Eastern Greenland, see Figure 1. The AOI is located east of the Northeast Greenland Ice Stream (NIGIS), which ends in two marine-terminating glaciers, the Zachariae Isstrøm (ZI), and the Nioghalvfjerdsfjord Gletcher (NG), combined this is one of the largest single sources of solid mass loss from the Greenland ice sheet [10]. The area is characterized by a large number of icebergs of various sizes, and in addition, by varying sea ice conditions. From winter to late spring, the area is completely covered by land-fast ice, meaning the icebergs do not change position. This makes our AOI a suitable study area for iceberg detection purposes [5].

B. SAR Images

A series of 8 L-band SAR images from the PALSAR-2 sensor onboard the ALOS-2 satellite are used in this study, with 4 images from 2019 and 4 images from 2020 (see Table I). All images were acquired in wide-beam, dual-polarization mode (HH and HV), with a pixel spacing of 25 meters. All images were acquired during the spring when the temperature in the region is below $-5°C$ on average and represent varying incidence angles and sea ice conditions [5]. Since all images were acquired before the break-up of the fast ice, sea ice conditions were similar in all images from the same year, differences are hence mainly related to the changes in incidence angle.

Data were provided by JAXA through the 2019 to 2022 mutual cooperation project between ESA and JAXA on using Synthetic Aperture Radar satellites in earth science and applications. The images were delivered in GRD format, and processed to normalized σ^0 before being geocoded to a polar stereographic coordinate system [1].

TABLE I
Image acquisitions used in the study. Images from two different orbits were used. The incidence angle (IA) is the average over the AOI.

Image ID	Date	IA
I-1	2019-04-25	19.5
I-2	2019-04-27	32.5
I-3	2019-04-29	22.7
I-4	2019-05-12	27.8
I-5	2020-04-09	19.6
I-6	2020-04-13	22.7
I-7	2020-04-25	32.4
I-8	2020-04-26	27.8

C. CFAR

Constant False Alarm Rate (CFAR) detection is an adaptive thresholding algorithm for finding outliers, in our case radar signatures of icebergs in SAR images. In this algorithm, each pixel under test (PUT) is compared against the local background clutter, and if the pixel exceeds a certain threshold, it is marked as an outlier. The threshold is determined using the local neighborhood statistics, thereby adapting to local conditions. Specifically, the local neighborhood is used to estimate the probability density function (PDF) of the background clutter intensity $P(I)$. Then, a threshold, t, can be determined by specifying a suitable probability of false alarm rate P_{fa} [11],

$$P_{fa} = \int_t^\infty P(I)dx = 1 - \int_0^t P(I)dx \tag{1}$$

That is if the local background clutter can be accurately estimated, the maximum backscatter intensity observed in the background will only exceed the threshold at a controlled level - a constant false alarm rate. So selecting a small PFA will ensure that most detections are unlikely to belong to the background clutter, and hence likely to be icebergs.

For many distributed targets, such as open water or agriculture, it is normally assumed that the clutter can be described using the product model [12], i.e., that the clutter arises from the product of two independent processes, namely the noise (speckle) and the texture [13]. Normally, for multi-looked intensity data, both the noise and the texture are assumed to follow a gamma distribution, which using the product model yields the K-distribution [13].

$$P(I) = \frac{2}{\Gamma(L)\Gamma(\nu)} \left(\frac{L\nu}{\mu}\right)^{\frac{L+\nu}{2}} I^{\frac{L+\nu-1}{2}} K_{\nu-L}\left[2\sqrt{\frac{\nu L I}{\mu}}\right] \tag{2}$$

Here, L is the equivalent number of looks, μ is the average clutter intensity, ν is the order parameter, Γ denotes the gamma function, and K_n is the Bessel function of the second kind and order n. The order parameter can be estimated, e.g., as [3]:

[1]EPSG:5938

$$\nu = \frac{\mu^2(L+1)}{\mathrm{var}(x)L - \mu^2} \tag{3}$$

Even though CFAR detectors are widely used for ship and iceberg detection in SAR images, some minor challenges exist. Firstly, for accurate estimation of the background clutter, a large number of samples are needed - meaning a large clutter estimation window is needed. However, due to variations in the local background clutter conditions, covering a large local neighborhood increases the risk of including samples belonging to different clutter distributions, thus skewing the estimation and degrading performance [14]. Secondly, to prevent backscatter contributions of an iceberg which is located in the center of the clutter estimation window, from interfering with the clutter estimation, a guard window is normally added around the center pixel [15]. The size of this guard window has to be chosen such that large icebergs do not extend into the clutter estimation region. Hence, when designing a CFAR detector, the size of the clutter estimation window, and the guard region, must be adapted to the local conditions in a way that maximizes the number of samples that can be used for clutter estimation while minimizing the risk of including heterogeneous areas in the estimation.

In practice, this is done by making some assumptions about the typical iceberg size within the region under observation and setting the size of the guard window accordingly. The size of the clutter estimation window can then be determined based on the required number of samples (pixels). However, if the sizes of icebergs within an AOI are highly variable, it becomes difficult to design a guard window to accommodate all iceberg sizes. If the guard window is too small, larger icebergs will spill over into the clutter estimation window which will degrade detection performance. If the guard window is too large, the clutter estimation window also needs to be larger so that enough samples are available for clutter estimation, which in turn, increases the risk of including adjacent icebergs in the clutter estimation window, which also degrades the performance.

D. Multiscale CFAR

The multiscale CFAR algorithm aims to keep some of the strengths of the normal CFAR, i.e., finding local statistical outliers, while solving some of the challenges, i.e., difficulties with large size differences. Multiscale processing is a well-known tool within signal and image processing and deep learning. A multiscale CFAR approach, using a small-scale and a large-scale window was suggested by Ao et al., [16]. In this study, the authors used a global thresholding technique, two CFAR detectors, and eigenellipse discrimination, to detect ships in complex coastal environments.

In our study, we are suggesting a general approach using down-scaling, CFAR detection, and upscaling, see Figure 2. The algorithm works by applying a normal CFAR algorithm in N steps, on different resolutions of the image. In the first step ($n = 1$), the CFAR algorithm is applied to the original image, and in subsequent steps, downsampled versions of the image are used. Here, we downsample with 2^{n-1}, for $n = [1, N]$. In each step, the results of the CFAR algorithms are upsampled so they match the resolution of the $n = 1$ step. Finally, after N steps, all the detections are added together to a single image. A threshold can now be applied to this image depending on how many times a detection should be made before accepting it as an outlier.

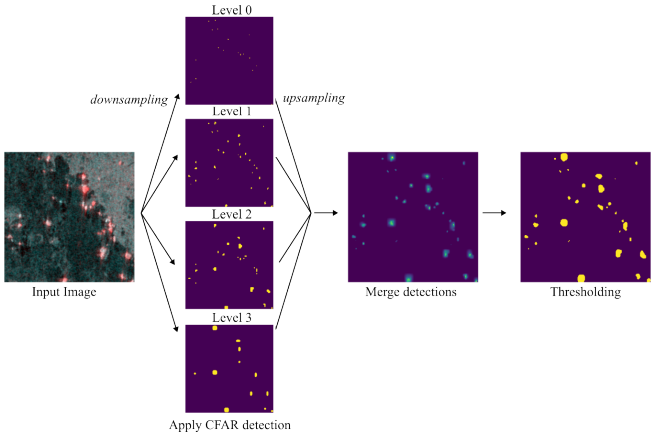

Fig. 2. Muliscale CFAR detection. CFAR detection is applied to several downsampled versions of the original image before the results are upsampled and merged. The final results are found by thresholding the merged detections.

As such, the algorithm will detect smaller icebergs at the lower levels, and larger icebergs at the larger levels, without the need to design the window sizes based on assumptions regarding the expected iceberg sizes in an AOI.

E. Implementation Details

As the CFAR algorithm needs to adapt to the local variation of the background clutter, a new threshold has to be found for each pixel in an image. However, since there is no analytical way to invert the probability density function of Equation 2 and get the threshold in Equation 1, the threshold has to be found numerically. This is a major disadvantage of using the K-distribution for CFAR detection, as the computation times are greatly increased. In practice, this can be solved by creating a look-up table (LUT) of thresholds [17]. The order parameter ν can then be calculated for each pixel based on the mean and variance of the clutter estimation window using Equation 3, and a suitable threshold can be determined by finding the nearest entry in the LUT. Then, each pixel can be compared against a relative multiplicative threshold $t\mu$, and if the pixel exceeds the value it is marked as an outlier [17], [18].

The traditional single-scale CFAR detector was implemented with a circular clutter estimation window with a diameter of 24 pixels, corresponding to 600 meters in the SAR images, and with a circular guard window diameter of 18 pixels corresponding to 450 meters. This configuration left a total of 192 pixels for the estimation of the clutter statistics. The CFAR detector is thereby designed to capture icebergs up to 225 meters in length.

For the multiscale CFAR detector, a clutter estimation window diameter of 16 pixels (400 meters) was used for level 1, with a guard window diameter of 6 pixels (150 meters) this corresponds to 172 pixels used for clutter estimation. Four

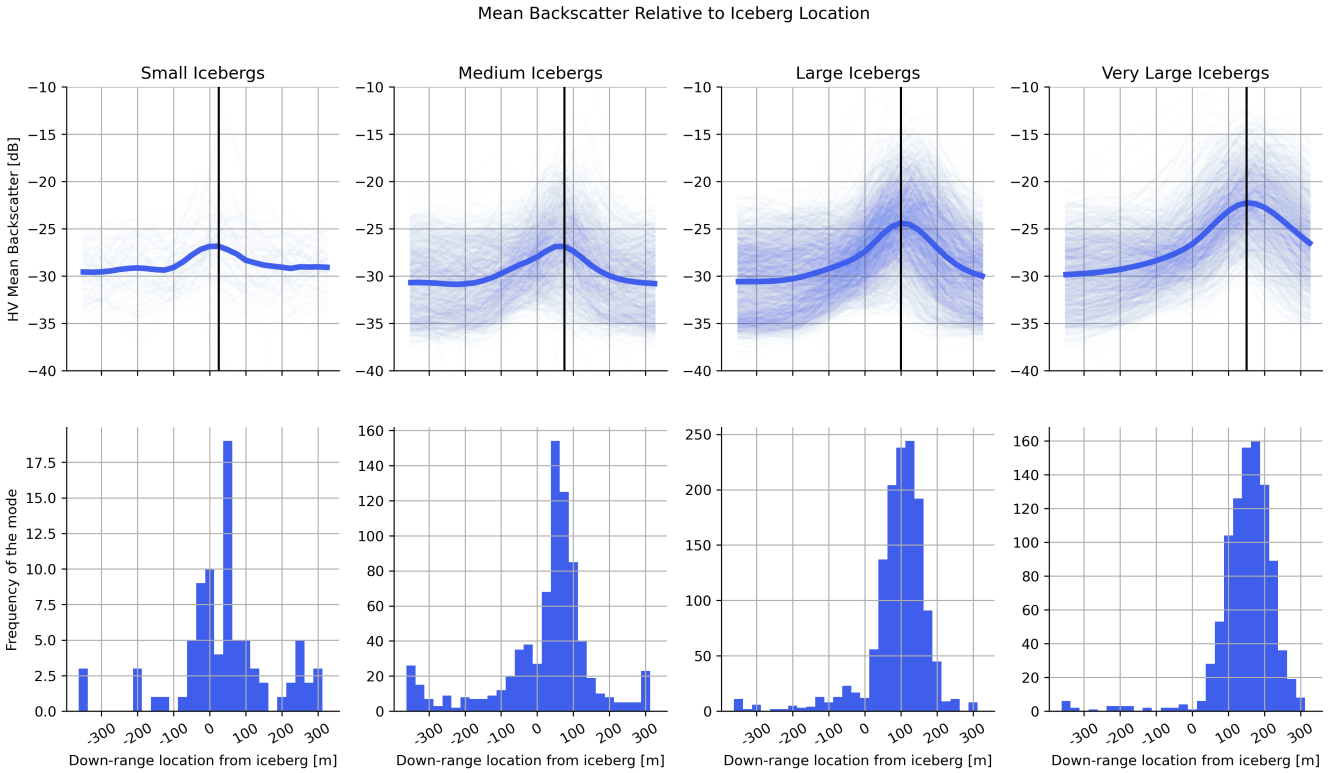

Fig. 3. Measured time-delay for small, medium, large, and very large icebergs. The figure shows the average of all 8 images. The thin blue lines indicate the signals from individual icebergs, with the thick blue line indicating the average of all signals. The black vertical line represents the value used for correcting the time delay. A histogram of the modes is plotted below. It is seen that the measured time delay increases with iceberg size.

levels were used for the implementation, which means that the multiscale detector is designed for icebergs with lengths up to 75 meters at level one, doubling at each level up to 600 meters at level 4.

As the SAR images contain both HH and HV polarization, the detectors were applied to both channels independently, and the results were combined using a boolean OR operator [15]. This approach was based on earlier observations which showed that icebergs in sea ice generally exhibit higher backscatter than sea ice at both HH and HV polarization for L-band SAR [5]. A PFA of 1×10^{-3} was used for both detectors. The equivalent number of looks, L was assumed to be identical to the multilook value of the ALOS-2 Wide-Beam ScanSAR mode which was 6. The implementation of the CFAR algorithms can be found at Github [19].

F. Validation

Iceberg polygons were used to validate the detections of the CFAR algorithms. The polygons were created manually using optical Sentinel-2 images as a reference [20]. In 2019 our study area covered 697 icebergs, with an average length of 182 meters, and 75% of the icebergs being shorter than 223 meters. Here, the length is defined as the major axis of the iceberg. For 2020, 635 icebergs were identified in our AOI, with an average length of 178 meters, and 75% of the icebergs were shorter than 217 meters. The median value of the 10 largest icebergs was 502 meters in 2019 and 667 in 2020, highlighting the large size difference in icebergs for the AOI.

Icebergs at L-band have previously been shown to exhibit time-delayed reflections [21]. As the CFAR algorithms will identify the location of the highest intensity, this time delay needs to be corrected. To solve this issue, the time delay for icebergs of different sizes was estimated (see Figure 3). This was achieved by shifting the polygons from their locations in the Sentinel-2 images up-range and down-range in the SAR image respectively, and calculating the mean backscatter intensity for the new positions [5]. To avoid mixing signals from several icebergs, only isolated icebergs without any neighboring icebergs within a 400-meter distance were used for this analysis. The analysis was carried out using the HV polarization since a previous study showed that icebergs and sea ice exhibit a larger separation in the HV polarization [5]. The results show that the peak backscatter intensity is located down-range of the true iceberg location, with a larger time delay for larger icebergs. The misplacements due to the time delay were 25, 75, 100, and 150 respectively for small, medium, large, and very large icebergs. Here, the definition of iceberg sizes from WMO was used, with small, medium, large, and very large icebergs being < 60, $60-120$, $120-220$, and > 220 meters in length respectively [22]. Based on these results, all icebergs in the validation data were moved down-range according to their size.

Detections made by the CFAR algorithms were merged

into objects of connected pixels, with objects smaller than 3 pixels being discarded to limit the influence of speckle noise. These detected objects were validated against the time delay corrected iceberg polygons. If a detected object overlapped an iceberg polygon, the iceberg was marked as a true positive (TP). Iceberg polygons not overlapped by a detected object are marked as a false negative (FN). Detected objects not overlapping an iceberg polygon were marked as false positives (FP). This means that if a detected object overlaps several iceberg polygons, e.g., an iceberg cluster, these will be marked as multiple TPs. This object-based approach to the validation ensures that slight discrepancies between the detected objects and true iceberg locations and shapes do not result in false positives as long as the objects overlap.

Based on the number of TP, FP, and FN, the recall, precision, and F1-score were calculated for each of the detectors [15]. The recall and precision are related to the number of FNs and FPs respectively, while the F1 score combines the two. All three performance scores can achieve values between 0 (worst) to 1 (best). In addition, the total area of detected icebergs (both TPs and FPs) was calculated as a fraction relative to the total iceberg areas (including FNs) in the reference data.

III. Results and Discussion

The results of applying the single-scale CFAR and the multiscale CFAR algorithms to the 8 images are shown in Tables II and III respectively. The results reveal that the multiscale CFAR achieves a higher F1-score for all images compared to the single-scale CFAR approach, with an average increase of 0.05. The tables show that this is driven by both a higher precision and recall, with a higher number of TP, and a lower number of FP and FN on average for the multiscale approach. For both detectors, the results appear consistent across all 8 test images, with no major differences due to the different incidence angles at which the images were recorded. In general, both detectors achieved better results on the 2019 images than on the 2020 images. This can likely be attributed to the fact that the AOI covered a larger fraction of deformed sea ice in the scenes from 2020 compared to 2019 [15]. When looking at the area estimation, the single-scale CFAR approach generally strongly underestimates the total iceberg area with an average across all images of 0.53 compared to a slight overestimation by the multiscale CFAR approach of 1.05 on average, however with two images getting overestimations above 1.2. Comparing the results in Tables II and III against the incidence angles in Table I reveals that the results appear to be slightly influenced by changes in incidence angle. This is best recognized in the results of the multi-scale CFAR detector. The highest F1 scores are obtained for the lowest incidence angle (2019: 19.5 deg with F1=0.71, 2020: 19.6 deg with F1=0.61), and the lowest for the largest incidence angle (2019: 32.5 deg with F1=0.63, 2020: 32.4 deg with F1=0.55). This corresponds with previously published results which showed a better separation between sea ice and icebergs at low incidence angles [5].

The aggregated recall, precision, F1-score, and fractional area estimation of all 8 images separated according to iceberg size is shown in Figure 4. Here, the error bars indicate the standard error. The results reveal that both detectors in general show increasing performance with increasing iceberg sizes. The main exception here is the precision, which for the multiscale CFAR is high for all icebergs except medium-sizes, and which the single-scale CFAR shows a small precision for both small and medium icebergs. In general, the multiscale approach shows a higher performance than the single-scale approach with the exceptions being the recall, where similar results are obtained for small icebergs, and the precision, where similar results are obtained for very large icebergs. This means that both methods reveal similar (high) numbers of FNs for small icebergs and that the two methods show a similar (low) number of FPs for very large icebergs. Nevertheless, when looking at the F-score, which combines both precision and recall, the multiscale approach outperforms the single-scale CFAR, showing a larger number of FPs for small icebergs (lower precision), and a larger number of FNs (lower recall) for very large icebergs. As for the area estimation, the plot reveals that the single-scale CFAR tends to overestimate the total area of small and medium icebergs while underestimating the total area of large and very large icebergs. The multiscale CFAR on the other hand, overestimates the total area made up of medium and very large icebergs while underestimating small and large icebergs.

TABLE II
Single-scale CFAR Results

Image ID	I-1	I-2	I-3	I-4	I-5	I-6	I-7	I-8
TP	404	328	404	392	322	331	282	314
FN	293	369	293	305	313	304	353	321
FP	133	103	119	130	233	269	182	231
precision	0.75	0.76	0.77	0.75	0.58	0.55	0.61	0.58
recall	0.58	0.47	0.58	0.56	0.51	0.52	0.44	0.49
F1	0.65	0.58	0.66	0.64	0.54	0.54	0.51	0.53
Area	0.63	0.40	0.58	0.53	0.61	0.61	0.40	0.50

TABLE III
Multiscale CFAR Results

Image ID	I-1	I-2	I-3	I-4	I-5	I-6	I-7	I-8
TP	450	353	436	410	352	363	309	350
FN	247	344	261	287	283	272	326	285
FP	127	66	107	95	174	247	178	233
precision	0.78	0.84	0.80	0.81	0.67	0.60	0.63	0.60
recall	0.65	0.51	0.63	0.59	0.55	0.57	0.49	0.55
F1	0.71	0.63	0.70	0.68	0.61	0.58	0.55	0.57
area	1.32	0.72	1.15	0.98	1.24	1.20	0.79	0.97

Examples of the detector outputs are shown in Figures 5 and 6. Here, the iceberg locations derived from the Sentinel-2 image (left) have been time-delay corrected and plotted on top of an ALOS-2 image (center and right). The outputs of the single-scale CFAR algorithm are marked with red (center), and the outputs of the multiscale CFAR with blue (right). The results from the individual levels have also been marked on the right side. Figure 5 reveals that the single-scale CFAR has a few more missed detections compared to the multiscale CFAR. In addition, both detectors have missed several of the

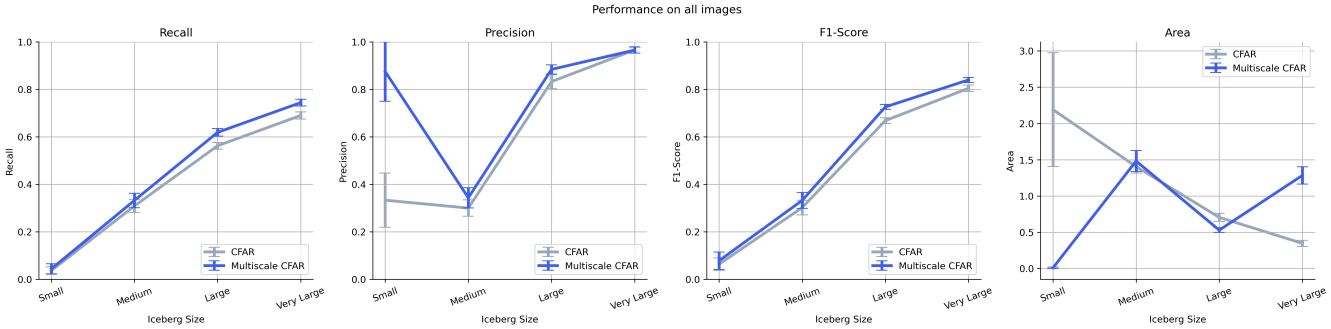

Fig. 4. Aggregated results for all 8 images, separated according to iceberg size.

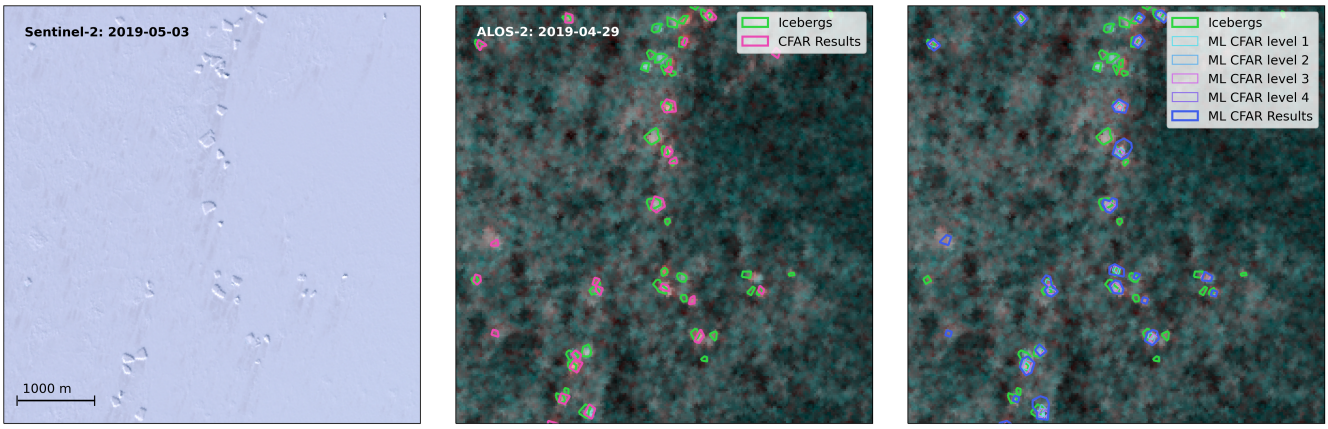

Fig. 5. Performance of the CFAR (middle) and multilevel CFAR (right) on a subset containing a large number of small and medium icebergs. The Sentinel-2 image is shown as a reference on the left. The true iceberg locations (green) are plotted together with the CFAR (red) and multiscale CFAR (blue) detections.

icebergs in the cluster on top of the image, and show two false detections on the left likely caused by deformed sea ice areas. The multiscale detector has detected most of the icebergs at levels 1-3, with a few of the smallest icebergs being detected exclusively at level 1. Also, from Figure 6 it can be concluded that the multiscale CFAR exhibits a slightly higher number of true detections, although both detectors still show a moderate number of missed detections. The multiscale CFAR in general appears better at estimating the full extent of the larger icebergs compared to the CFAR approach. At the lower levels, the multiscale approach generally detects the icebergs as individual objects, but we found that for some clusters, the multiscale detecter interprets clusters of small and medium icebergs as very large icebergs.

Comparing Figure 4 with the results from Tables II and III reveals some aspects regarding the area estimation. Although both detectors show a higher number of FNs than FPs, which would suggest a slight underestimation of the total area covered by icebergs, only the single-scale CFAR approach shows a consistent underestimation. Separation of the results according to iceberg sizes in Figure 4 shows that although the single-scale CFAR generally overestimates the total area made up of small and medium icebergs, the underestimation of the area made up of large and very large icebergs leads to a general iceberg area underestimation. The large overestimation of small and medium iceberg areas could be caused by a high number of false positives of medium and small icebergs, as seen by the low precision. The underestimation of the total area of large and very large icebergs could be because the single-scale CFAR detector tends to only detect a small fraction of the larger icebergs, hence falsely interpreting their area as being too small (see Figure 6). The multiscale CFAR vastly underestimates the area of small icebergs. This is likely caused by small icebergs being interpreted as larger ones, and in addition due to a lack of small false positives (see precision in Figure 4). For medium, large, and very large icebergs, the area estimation varies between 0.5-1.5. The total area of very large icebergs is overestimated, possibly due to clusters of icebergs being interpreted as very large icebergs.

As explained above, the results are validated considering the time delay of the iceberg radar response at L-band. However, since the actual time-delay for the individual icebergs might be slightly different than the value used for correction (see the widths of the histograms in Figure 3), the correction might in some cases lead to errors, i.e., if the detected location is not overlapping the location found in the validation data. Small and medium icebergs should be more sensitive to this issue. However, visual inspection of Figures 5 and 6 show matching locations for the majority of the icebergs.

In summary, both detectors show a small number of FPs, mainly caused by areas of deformed sea ice. Both detectors show a moderate number of FNs, with most missed detections

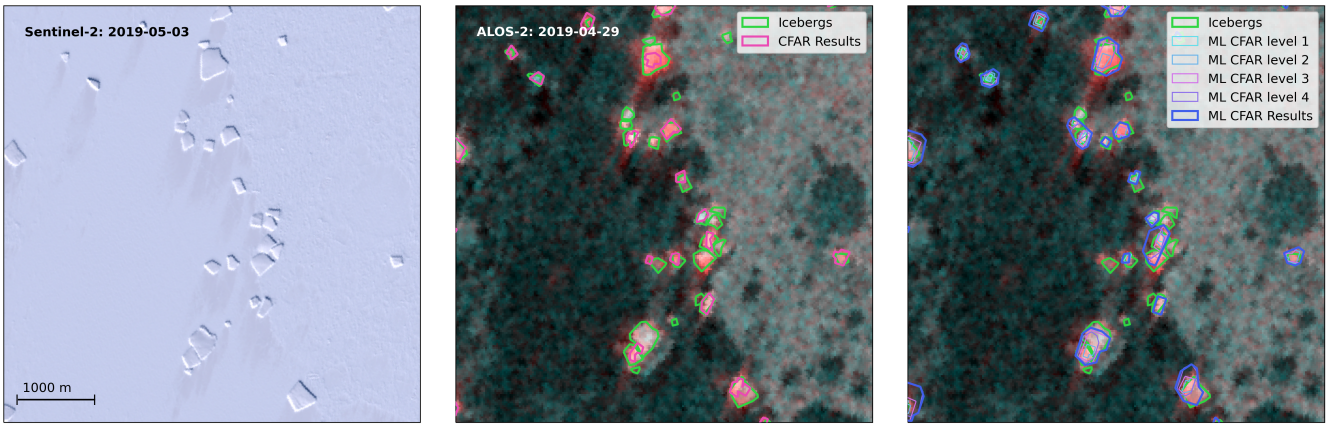

Fig. 6. Performance of the CFAR (middle) and multilevel CFAR (right) on a subset containing a few very large icebergs, as well as several large and medium icebergs. The Sentinel-2 image is shown as a reference on the left. The true iceberg locations (green) are plotted together with the CFAR (red) and multiscale CFAR (blue) detections.

occurring for icebergs showing a low backscatter intensity. Although the performance is quite similar for the two detectors, the suggested multiscale CFAR approach shows a consistent advantage across all images and performance scores, with only a few examples of icebergs being detected by the single-scale CFAR approach but not the multiscale approach. The multiscale approach excels especially for iceberg clusters or larger icebergs, although the high performance for iceberg clusters generally comes at the cost of merging several smaller objects. The area estimation results show that the different methods might introduce some problems when estimating areas. Hence, more work is encouraged to obtain more accurate results.

Both detectors show degrading performance for the 2020 images compared to the 2019 images, suggesting general challenges when performing iceberg detection in deformed sea ice conditions. In addition, the best results appear to be obtained at low incidence angles.

IV. Conclusion

In this study, a simple multiscale extension to the well-known single-scale CFAR approach has been introduced, to improve iceberg detections for areas with a high variation in iceberg sizes. The new method was compared to a classical single-scale CFAR algorithm utilizing the K-distribution to detect icebergs embedded in sea ice. By testing the new method on 8 different L-band SAR images acquired at different incidence angles, this study quantifies the improvement of iceberg detection when using a multi-scale approach. This is achieved by comparing the detections in the SAR images to iceberg positions in optical Sentinel-2 images. We found that the F1-score increases over the investigated incidence angle range and for different iceberg sizes. In addition, the study highlights the feasibility of detecting icebergs in fast ice using L-band SAR when considering the spatial shift of the iceberg responses. The multi-scale approach can easily be applied to images acquired at different radar frequencies or other imaging sensors.

References

[1] R. S. Gill, "Operational detection of sea ice edges and icebergs using SAR," *Canadian Journal of Remote Sensing*, vol. 27, no. 5, pp. 411–432, 2001.

[2] D. Power, J. Youden, K. Lane, C. Randell, and C. R. D. Flett, "Iceberg detection capabilities of radarsat synthetic aperture radar," *Canadian Journal of Remote Sensing*, vol. 27, no. 5, pp. 476–486, 2001.

[3] C. Wesche and W. Dierking, "Iceberg signatures and detection in SAR images in two test regions of the Weddell Sea, Antarctica," *Journal of Glaciology*, vol. 58, no. 208, pp. 325–339, 2012.

[4] I. H. Soldal, W. Dierking, A. A. Korosov, and A. Marino, "Automatic detection of small icebergs in fast ice using satellite Wide-Swath SAR images," *Remote Sensing*, vol. 11, no. 7, pp. 1–24, 2019.

[5] L. Færch, W. Dierking, N. Hughes, and A. P. Doulgeris, "Mapping icebergs in sea ice: An analysis of seasonal SAR backscatter at C- and L-band," *Remote Sensing of Environment*, vol. 304, no. February, p. 114074, 2024. [Online]. Available: https://doi.org/10.1016/j.rse.2024.114074

[6] W. Dierking and M. Davidson, "Enhanced Sea ICE Monitoring at L- and C-Bands using Rose-L and Sentinel-1," *International Geoscience and Remote Sensing Symposium (IGARSS)*, pp. 4059–4060, 2020.

[7] J. A. Casey, S. E. Howell, A. Tivy, and C. Haas, "Separability of sea ice types from wide swath C- and L-band synthetic aperture radar imagery acquired during the melt season," *Remote Sensing of Environment*, vol. 174, pp. 314–328, 2016. [Online]. Available: http://dx.doi.org/10.1016/j.rse.2015.12.021

[8] ESA, "Copernicus L-band SAR Mission Requirements Document," ESA Applications, 3 December 2020, Tech. Rep., 2018.

[9] I. Joughin, B. Smith, I. Howat, and T. Scambos, "MEaSUREs Multi-year Greenland Ice Sheet Velocity Mosaic, Version 1." 2016.

[10] K. D. Mankoff, A. Solgaard, W. Colgan, A. P. Ahlstrøm, S. Abbas Khan, and R. S. Fausto, "Greenland Ice Sheet solid ice discharge from 1986 through March 2020," *Earth System Science Data*, vol. 12, no. 2, pp. 1367–1383, 2020.

[11] C. Brekke and S. N. Anfinsen, "Ship detection in ice-infested waters based on dual-polarization SAR imagery," *IEEE Geoscience and Remote Sensing Letters*, vol. 8, no. 3, pp. 391–395, 2011.

[12] X. Deng, C. López-martínez, J. Chen, and P. Han, "Statistical Modeling of Polarimetric SAR Data : A Survey and Challenges," *Remote Sensing*, pp. 1–34, 2017.

[13] C. Oliver and S. Quegan, *Understanding synthetic aperture radar images*, 1997, vol. 53, no. 9.

[14] D. Tao, S. N. Anfinsen, and C. Brekke, "Robust CFAR Detector Based on Truncated Statistics in Multiple-Target Situations," *IEEE Transactions on Geoscience and Remote Sensing*, vol. 54, no. 1, pp. 117–134, 2016.

[15] L. Færch, W. Dierking, N. Hughes, and A. P. Doulgeris, "A Comparison of CFAR Object Detection Algorithms for Iceberg Identification in L-and C-band SAR Imagery of the Labrador Sea," *The Cryosphere*, vol. 17, pp. 5335–5355, 2023. [Online]. Available: https://doi.org/10.5194/tc-2023-17

[16] W. Ao, F. Xu, Y. Li, and H. Wang, "Detection and Discrimination of Ship Targets in Complex Background from Spaceborne ALOS-2 SAR Images," *IEEE Journal of Selected Topics in Applied Earth Observations and Remote Sensing*, vol. 11, no. 2, pp. 536–550, 2018.
[17] C. Brekke, "Automatic ship detection based on satellite SAR," Norwegian Defence Research Establishment (FFI), Tech. Rep. May, 2009.
[18] J. K. Tunaley, "K-distribution algorithms," *Automation and Remote Control*, vol. 67, no. 8, pp. 1251–1264, 2010.
[19] L. Færch, "CFAR Object Detection." [Online]. Available: https://github.com/LaustFaerch/cfar-object-detection
[20] F. Amdal and N. Hughes, "Multi-Sensor Ice Analysis Data: Analysis for Belgica Bank, North East Greenland 2019-20," https://henry.ub.uit.no/Record/ftzenodo:oai:zenodo.org:7053975, 2022.
[21] A. L. Gray and L. D. Arsenault, "Time-Delayed Reflections in L-Band Synthetic Aperture Radar Imagery of Icebergs," *IEEE Transactions on Geoscience and Remote Sensing*, vol. 29, no. 2, pp. 284–291, 1991.
[22] JCOMM Expert Team on Sea Ice, "Sea-Ice Nomenclature: snapshot of the WMO Sea Ice Nomenclature WMO No. 259, volume 1 – Terminology and Codes; Volume II – Illustrated Glossary and III – International System of Sea-Ice Symbols," WMO-JCOMM, Geneva, Switzerland, Tech. Rep. 259, 2014.

9

Conclusions and Outlook

The focus of this thesis is on the comparison of C- and L-band SAR for the accurate detection and mapping of Arctic icebergs. To this end, three scientific objectives were summarized in Chapter 1, and to help accomplish these objectives, three papers were prepared for publication, and are found in Chapters 6-8. Below, we will outline a conclusion to each of the three research objectives based on the results in these papers. We will also provide an outlook based on the findings, and suggest a short list of possible future important work.

9.1 Research Conclusions

Explore how the use of L-band SAR data can complement current C-band data for the detection of icebergs in open water
Paper I provides a comparison between C- and L-band SAR for detecting icebergs in open water. Here, a large dataset of independent iceberg observations was used to compare the performance of several CFAR detection algorithms. The results reveal that although the best performance is obtained using a Log-Normal PDF CFAR on the L-band image, the performance of the two frequencies is very similar on average.

The results suggest that L-band offers no large improvement over C-band for iceberg detection under low-wind conditions. However, as the performance of the two frequencies was similar, L-band still offers the potential to be used together with C-band for operational iceberg detection.

Determine whether L-band SAR data can improve the detection of icebergs in sea ice compared to C-band data
Paper II provides a comparison between C- and L-band SAR for detecting icebergs in sea ice. This comparison was carried out by utilizing a time series of

C- and L-band images acquired over an area with a large number of stationary icebergs. The results reveal that L-band is superior to C-band for the detection of icebergs in sea ice, as C-band SAR cannot be used to distinguish icebergs from deformed sea ice. The results also show a clear relationship between the iceberg to sea ice backscatter contrast and the temperature, with rapidly decreasing contrast under melting conditions.

Overall, the results show that L-band SAR offers a great improvement over C-band SAR for detecting icebergs in sea ice. The results also suggest that the best performance is obtained under freezing conditions and for smaller incidence angles.

Evaluate the performance of iceberg detection algorithms applied to SAR images using independent iceberg observations
All three journal papers produced as part of this dissertation are based on large-scale independent iceberg observations to assess the results. This enabled us to determine several important factors related to iceberg detection.

Firstly, in *paper I* the performance relative to iceberg sizes shows that $20-30\%$ of medium (length $1.5-3$ times the pixel spacing) and 4% of large (length $3-5$ times the pixel spacing) icebergs in open water were not detected. *Paper III* also reveals a clear relationship between iceberg sizes and detection accuracy, with an F1-score of $0.3-0.35$ for medium icebergs (length $2.4-4.8$ times the pixel spacing), and $0.67-0.73$ for large icebergs (length $4.8-8$ times the pixel spacing). These results suggest that the required spatial resolution needs to be several times larger than the iceberg size for robust detection, and larger for the detection of icebergs in sea ice compared to open water, likely due to the highly varying characteristics of sea ice backscatter.

Secondly, in *paper I* the results from both C- and L-band reveal that most of the different CFAR detectors can obtain similar performance, but at different PFA levels. These findings suggest that when choosing a CFAR detector for operational iceberg detection, the choice of the PDF only has minor implications on performance compared to the tuning of the PFA level.

Lastly, based on the findings of *paper II*, *paper III* suggests improved methods for detecting icebergs in sea ice, especially considering the large size variations of icebergs in the study area and the presence of clusters of icebergs. To this end, a multiscale approach to CFAR detection is suggested, which consistently outperforms the traditional single-scale CFAR approach. Furthermore, it is shown in *paper II* and *paper III*, that the performance of iceberg detection of L-band SAR is influenced by the incidence angle.

In addition to evaluating the iceberg detection performance, the comparison

between optical and SAR data shows that icebergs in L-band are influenced by time-delayed reflections. This has implications for iceberg detection evaluation, as the main backscatter signal from the icebergs are located down-range from the actual location in the L-band image. This poses a challenge for validating iceberg detections, and to overcome this challenge a correction method is suggested in *paper II*. In *paper III* we used this correction method to show that the time delay increases with increasing iceberg sizes.

9.2 On the validation data

As discussed in Chapter 4, the backscatter signatures of icebergs are highly variable, making it hard to gather reliable information from a small number of observations. Therefore, this Ph.D. project focused on a more thorough comparison of well-known detection methods applied to SAR images, using validation data from optical sensors. As such, the results of *paper 1* are based on 492 iceberg observations from Sentinel-2, which were compared to detections in both Sentinel-1 (C-band) and ALOS-2 (L-band) data. For *paper II* 657 independent iceberg observations across a time series of L- and C-band images are used, covering 2 years and varying seasonal conditions. This results in a total of 13.386 unique iceberg observations using L-band SAR, and 10.266 unique iceberg observations at C-band SAR. In *paper III*, 1.332 icebergs were identified across two years, giving rise to 5.328 unique iceberg observations.

This large dataset helps to increase the overall confidence in the results, and as such, the work carried out in this dissertation provides a significant examination of icebergs using SAR. This comprehensive approach goes beyond what most existing studies on iceberg detection offer.

9.3 Outlook and Future Work

Outlook

Broadly, our results suggest that L-band SAR offers a complement for C-band SAR for detecting icebergs in open water. As L-band offers a similar performance to C-band, new L-band missions can help decrease the time gap between iceberg observations, providing a denser time series for operational monitoring. This increases the timeliness of iceberg observations and helps reduce the uncertainties in drift forecasting thus reducing the risk for individuals and organizations operating in the Arctic.

L-band data are beneficial for detecting icebergs in sea ice. Consequently, new L-band missions have the potential to vastly improve the scale of iceberg monitoring in the Arctic, from currently being limited to open water, to being expanded into areas containing sea ice. This can e.g, be done using the multiscale CFAR approach suggested in *paper III*.

Our results show that the detection accuracy depends on the size of the icebergs. Even icebergs many times larger than the SAR pixel spacing have the risk of being missed by automatic detection algorithms. This suggests that independent warning measures should be in place to protect ships and critical infrastructure against iceberg collisions.

Future Work

Despite the work carried out here, additional research efforts are required to further improve our ability to detect and map iceberg occurrences. As such, based on our work, a short list of potential future research topics is suggested below.

- **Large scale detection of icebergs in open water for the Barents Sea**
  As mentioned in Chapter 1, a long time series of C-band Sentinel-1 data is currently available for the Arctic, enabling long-term iceberg detections in the Barents Sea. Based on the findings in *paper I*, one or several of the CFAR detection algorithms could be applied to a time series of data to provide estimates of iceberg occurrences. Given that the results in *paper I* were obtained under low wind conditions, a challenge here is the varying wind conditions and if the optimum PFA level might change under different wind states. This could potentially be solved by tuning the PFA level of the detection algorithms using the quality-assured iceberg maps from DMI or IIP before applying them to the Barents Sea. The quality of the product could be further improved by utilizing the high revisit frequency of Sentinel-1 for developing time series filtering techniques, or by introducing auxiliary datasets such as including meteorological conditions, to remove false detections.

- **Investigating the performance of iceberg detection in open water under different wind conditions.**
  Although we have managed to characterize the performance for C- and L-band SAR for iceberg detection in open water (*paper I*), some challenges lie ahead. Specifically, the question of performance under different wind conditions remains. As mentioned in Chapter 4, L-band might prove superior to C-band under rough sea states due to the longer wavelength. However, confirming this requires better and larger sets of validation data,

acquired under different wind conditions. Expanding the dataset used in *paper I* to include several new acquisitions of L- and C-band SAR images, acquired under different wind conditions, could help characterize the influence of wind on the detection performance. A challenge here is the use of optical data as validation due to the frequently occurring cloud cover in the Arctic.

- **Investigating the performance of L-band for detection of icebergs in drift ice**
  In *paper I* we showed the opportunity of using L-band SAR for detecting icebergs in open water, and in *paper II* and *paper III* we showed the opportunities of using L-band SAR for iceberg detection in land-fast sea ice. However, the question of the transferability of the results to icebergs in drift ice remains. Drifting ice at varying concentrations is a more complex challenge for iceberg detection than either open water or land-fast ice, and CFAR detection might have problems due to the highly heterogeneous clutter. A study confirming the feasibility of detecting icebergs in drift ice using L-band is therefore valuable. However, a major challenge is how to obtain validation data for icebergs drifting in sea ice. A solution could be to collect in-situ data, however, this is a logistically challenging undertaking.

- **Evaluate the use of commercial X-band SAR as a source of validation data**
  Within the last few years, constellations of small SAR satellites from several commercial companies have emerged, e.g., ICEYE (Finland), Synspective (Japan), Capella Space, and Umbra Space (USA). Common for these companies is that they plan to operate a large fleet of X-band SAR satellites, offering high-resolution images, with highly flexible scheduling. Potentially, these X-band images can be acquired simultaneously to L- and C-band SAR overpasses, with resolutions down to less than 1 meter, removing the need to perform work-extensive drift correction as used in *paper I*. Since SAR images can be used for the identification of icebergs regardless of cloud cover and sunlight conditions, they offer an interesting source of complementary validation data, with the potential to be used in several of the future research efforts suggested here. However, a major challenge here is the fact that X-band SAR is highly sensitive to the small-scale surface roughness of water and snow, which might make it challenging to detect the icebergs using the X-band data in the first place. Nevertheless, this data source offers an interesting potential, and as such investigations into the advantages and disadvantages are encouraged.

- **Investigations on the time-delayed reflections**
  Icebergs in L-band SAR are affected by time-delayed signals, likely due

to internal reflections, causing the icebergs to be seen in the L-band image down-range from their original positions. With the future growth in available L-band data, investigations into this phenomenon have some interesting research potential. If the time delay is caused by reflections from the bottom of the icebergs, the time delay together with the SAR viewing geometry, has the potential to be used to derive the iceberg height. This could be used to estimate the volume and thus the mass of icebergs located in the fast-ice in North Eastern Greenland, something that could be of great benefit to glaciological applications. The Belgica Bank study site which we used in *paper II* and *paper III* provides an interesting study area given the large number of stationary tabular icebergs. Investigations could be conducted by combining LIDAR measurements from CryoSat-2, with external bathymetry data to obtain ground truth estimates of iceberg heights. Additionally, fully polarimetric high-resolution SAR at C- and L-band could be used to investigate the exact scattering mechanisms.

Despite such need for further research we conclude that there is a true advantage of L-band over C-band for the detection of icebergs in sea ice. This opens up a whole new area for monitoring, allowing for a more complete mapping of icebergs, and greatly improving the possibilities of Arctic-wide iceberg surveillance.

Bibliography

[1] JCOMM Expert Team on Sea Ice. *Sea-Ice Nomenclature: snapshot of the WMO Sea Ice Nomenclature WMO No. 259, volume 1 – Terminology and Codes; Volume II – Illustrated Glossary and III – International System of Sea-Ice Symbols*. Tech. rep. 259. Geneva, Switzerland: WMO-JCOMM, 2014. DOI: https://doi.org/10.25607/OBP-1515.

[2] N. Einarsson et al. *Arctic Human Development Report*. Stefansson Arctic Institute, 2004. ISBN: 9979834455.

[3] G. R. Bigg. *Icebergs: Their Science and Links to Global Change*. Cambridge: Cambridge University Press, 2015. ISBN: 9781107675803.

[4] R. Marsh et al. "NEMO-ICB (v1.0): Interactive icebergs in the NEMO ocean model globally configured at eddy-permitting resolution." In: *Geoscientific Model Development* 8.5 (2015), pp. 1547–1562. ISSN: 19919603. DOI: 10.5194/gmd-8-1547-2015.

[5] Kenneth D. Mankoff et al. "Greenland Ice Sheet solid ice discharge from 1986 through March 2020." In: *Earth System Science Data* 12.2 (2020), pp. 1367–1383. ISSN: 18663516. DOI: 10.5194/essd-12-1367-2020.

[6] William Kochtitzky et al. "The unquantified mass loss of Northern Hemisphere marine-terminating glaciers from 2000–2020." In: *Nature Communications* 13.1 (2022), pp. 1–10. ISSN: 20411723. DOI: 10.1038/s41467-022-33231-x.

[7] Ellyn M. Enderlin et al. "Iceberg meltwater fluxes dominate the freshwater budget in Greenland's iceberg-congested glacial fjords." In: *Geophysical Research Letters* 43.21 (2016), pp. 11, 287–11, 294. ISSN: 19448007. DOI: 10.1002/2016GL070718.

[8] M. Meredith et al. "Polar regions." In: *IPCC Special Report on the Ocean and Cryosphere in a Changing Climate*. 2019, pp. 203–320. DOI: https://doi.org/10.1017/9781009157964.005.

[9] Chad A Greene et al. "Ubiquitous acceleration in Greenland Ice Sheet calving from 1985 to 2022." In: *Nature* 625.January (2024), pp. 523–528. DOI: 10.1038/s41586-023-06863-2.

[10] Ian M. Howat, Ian Joughin, and Ted A. Scambos. "Rapid changes in ice discharge from Greenland outlet glaciers." In: *Science* 315.5818 (2007), pp. 1559–1561. ISSN: 00368075. DOI: 10.1126/science.1138478.

[11] T. R. Chudley et al. “Atlantic water intrusion triggers rapid retreat and regime change at previously stable Greenland glacier.” In: *Nature Communications* 14.1 (2023), pp. 1–10. DOI: 10.1038/s41467-023-37764-7.

[12] Josefino C. Comiso. “Large decadal decline of the arctic multiyear ice cover.” In: *Journal of Climate* 25.4 (2012), pp. 1176–1193. ISSN: 08948755. DOI: 10.1175/JCLI-D-11-00113.1.

[13] Hiroshi Sumata et al. “Unprecedented decline of Arctic sea ice outflow.” In: *Nature Communications* 13 (2022). DOI: 10.1038/s41467-022-29470-7.

[14] Y. Aksenov et al. “On the future navigability of Arctic sea routes: High-resolution projections of the Arctic Ocean and sea ice.” In: *Marine Policy* 75 (2017), pp. 300–317. ISSN: 0308597X. DOI: 10.1016/j.marpol.2015.12.027. URL: http://dx.doi.org/10.1016/j.marpol.2015.12.027.

[15] Björn Gunnarsson. “Recent ship traffic and developing shipping trends on the Northern Sea Route—Policy implications for future arctic shipping.” In: *Marine Policy* 124.November 2020 (2021), p. 104369. ISSN: 0308597X. DOI: 10.1016/j.marpol.2020.104369.

[16] Laurence C. Smith and Scott R. Stephenson. “New Trans-Arctic shipping routes navigable by midcentury.” In: *Proceedings of the National Academy of Sciences of the United States of America* 110.13 (2013), pp. 6–10. ISSN: 00278424. DOI: 10.1073/pnas.1214212110.

[17] Arctic Council. “Arctic Marine Shipping Assessment 2009 Report.” In: *Arctic* (2009), pp. 39–55.

[18] NASA National Snow and Ice Data Center Distributed Active Archive Center. *Polar Pathfinder Daily 25 km EASE-Grid Sea Ice Motion Vectors, Version 4*. Accessed: 2024-02-05. DOI: 10.5067/INAWUWO7QH7B.

[19] Irina Mahlstein and Reto Knutti. “September Arctic sea ice predicted to disappear near 2°C global warming above present.” In: *Journal of Geophysical Research Atmospheres* 117.6 (2012), pp. 1–11. ISSN: 01480227. DOI: 10.1029/2011JD016709.

[20] I. Keghouche, F. Counillon, and L. Bertino. “Modeling dynamics and thermodynamics of icebergs in the Barents Sea from 1987 to 2005.” In: *Journal of Geophysical Research: Oceans* 115.12 (2010), pp. 1–14. ISSN: 21699291. DOI: 10.1029/2010JC006165.

[21] G. R. Bigg et al. “Modelling the dynamics and thermodynamics of icebergs.” In: *Cold Regions Science and Technology* 26 (1997), pp. 113–135. ISSN: 02588900. DOI: 10.1007/s004450050234.

[22] Dennis Monteban et al. “Enhanced iceberg drift modelling in the Barents Sea with estimates of the release rates and size characteristics at the major glacial sources using Sentinel-1 and Sentinel-2.” In: *Cold Regions Science and Technology* 175.April (2020), p. 103084. ISSN: 0165232X. DOI: 10.1016/j.coldregions.2020.103084. URL: https://doi.org/10.1016/j.coldregions.2020.103084.

[23] Valentin A. Abramov. "Russian iceberg observations in the Barents Sea, 1933– 1990." In: *Polar Research* 11.2 (1992), pp. 93–97. DOI: 10.3402/polar.v11i2.6720.

[24] The international Ice Patrol. *International Ice Patrol History*. URL: https://www.navcen.uscg.gov/international-ice-patrol-history (visited on 06/05/2024).

[25] Alberto Moreira et al. "A tutorial on synthetic aperture radar." In: *IEEE Geoscience and Remote Sensing Magazine* 1.1 (2013), pp. 6–43. ISSN: 21686831. DOI: 10.1109/MGRS.2013.2248301.

[26] Ramón. Torres, Malcolm. Davidson, and Dirk Geudtner. "Copernicus Sentinel Mission at C-and L-Band: Current Status and Future Perspectives." In: *IGARSS 2020-2020 IEEE International Geoscience and Remote Sensing Symposium*. 2020, pp. 4055–4058. ISBN: 9781728163741. DOI: 10.1109/IGARSS39084.2020.9323149.

[27] Copernicus Marine Service. *SAR Sea Ice Berg Concentration and Individual Icebergs Observed with Sentinel-1, Quality Information Document*. Accessed: 2024-06-10. URL: %5Curl%7Bhttps://catalogue.marine.copernicus.eu/documents/QUID/CMEMS-SEAICE-QUID-011-007.pdf%7D.

[28] International Ice Patrol. *International Ice Patrol (IIP) Iceberg Sightings Database, Version 1, User Guide*. Accessed: 2024-06-10. URL: %5Curl%7Bhttps://nsidc.org/sites/default/files/g00807-v001-userguide_1_1.pdf%7D.

[29] International Ice charting Working Group. *TASK TEAM 8: Mariner Training Requirement, Intermediate report to Ice Service Heads*. Accessed: 2024-06-10. 2019. URL: %5Curl%7Bhttps://nsidc.org/sites/nsidc.org/files/files/noaa/iicwg/2019/IICWG_Mariner_Survey_Intermediate_Report.pdf%7D.

[30] John Houghton. *Mass Balance of the Cryosphere*. 2004. ISBN: 9780521808958. DOI: 10.1017/cbo9780511535659.

[31] "Calving processes and the dynamics of calving glaciers." In: *Earth-Science Reviews* 82.3-4 (2007), pp. 143–179. ISSN: 00128252. DOI: 10.1016/j.earscirev.2007.02.002.

[32] Jacob Bendle. *Calving of freshwater glaciers*. 2020. URL: https://www.antarcticglaciers.org/glacier-processes/glacial-lakes/calving-of-freshwater-glaciers/ (visited on 11/30/2023).

[33] David N Thomas. *Sea Ice*. 3rd Editio. John Wiley & Sons, 2017. ISBN: 978-1-118-77838-8.

[34] Sveinung Løset et al. *Actions from ice on Arctic offshore and coastal structures*. 2006, p. 272. ISBN: 5811407033.

[35] Ian D Turnbull et al. "Operational iceberg drift forecasting in Northwest Greenland." In: *Cold Regions Science and Technology* 110 (2015), pp. 1–18. ISSN: 0165-232X. DOI: 10.1016/j.coldregions.2014.10.006. URL: https://doi.org/10.1016/j.coldregions.2014.10.006.

[36] Dan Fequet. *MANICE - Manual of Standard Procedures for Observing and Reporting Ice Conditions*. Tech. rep. 2005.

[37] Christine Wesche and Wolfgang Dierking. "Near-coastal circum-Antarctic iceberg size distributions determined from Synthetic Aperture Radar images." In: *Remote Sensing of Environment* 156 (2015), pp. 561–569. ISSN: 00344257. DOI: 10.1016/j.rse.2014.10.025. URL: http://dx.doi.org/10.1016/j.rse.2014.10.025.

[38] Daniel J. Sulak et al. "Iceberg properties and distributions in three Greenlandic fjords using satellite imagery." In: *Annals of Glaciology* 58.74 (2017), pp. 92–106. ISSN: 02603055. DOI: 10.1017/aog.2017.5.

[39] Connor J Shiggins, James M Lea, and Stephen Brough. "Automated ArcticDEM iceberg detection tool : insights into area and volume distributions , and their potential application to satellite imagery and modelling of glacier-iceberg-ocean systems." In: *The Cryosphere Discussions* di.August (2022), pp. 1–24.

[40] Jan Åström et al. "Fragmentation theory reveals processes controlling iceberg size distributions." In: *Journal of Glaciology* (2021), pp. 1–10.

[41] Mauro M. Barbat et al. "Three Years of Near-Coastal Antarctic Iceberg Distribution From a Machine Learning Approach Applied to SAR Imagery." In: *Journal of Geophysical Research: Oceans* 124.9 (2019), pp. 6658–6672. ISSN: 21699291. DOI: 10.1029/2019JC015205.

[42] Kurt M Cuffey and William Stanley Bryce Paterson. *The physics of glaciers*. Academic Press, 2010.

[43] P.F.; Scholander and D. C. Nutt. "Bubble Pressure in Greenland Icebergs." In: *Journal of Glaciology* 3.28 (1960), pp. 671–678. DOI: 10.3189/S0022143000017950.

[44] R. E. Gagnon and P. H. Gammon. "Characterization and flexural strength of iceberg and glacier ice." In: *Journal of Glaciology* 41.137 (1995), pp. 103–111. ISSN: 00221430. DOI: 10.1017/S0022143000017809.

[45] Deborah Diemand. "Iceberg Temperatures in the North Atlantic - Theoretical and Measured." In: *Cold Regions Science and Technology* 9 (1984), pp. 171–178.

[46] Mauro M. Barbat et al. "Automated iceberg tracking with a machine learning approach applied to SAR imagery: A Weddell sea case study." In: *ISPRS Journal of Photogrammetry and Remote Sensing* 172.December 2020 (2021), pp. 189–206. ISSN: 09242716. DOI: 10.1016/j.isprsjprs.2020.12.006. URL: https://doi.org/10.1016/j.isprsjprs.2020.12.006.

[47] Jamie Morison and Dan Goldberg. "A brief study of the force balance between a small iceberg, the ocean, sea ice, and atmosphere in the Weddell Sea." In: *Cold Regions Science and Technology* 76-77 (2012), pp. 69–76. ISSN: 0165232X. DOI: 10.1016/j.coldregions.2011.10.014. URL: http://dx.doi.org/10.1016/j.coldregions.2011.10.014.

[48] Sveinung Løset and Torkild Carstens. "Sea ice and iceberg observations in the western Barents Sea in 1987." In: *Cold Regions Science and Technology* 24.4 (1996), pp. 323–340. ISSN: 0165232X. DOI: 10.1016/0165-232X(95)00029-B.

[49] John E. Walsh. "Climate of the arctic marine environment." In: *Ecological Applications* 18.2 (2008), pp. 3–22.

[50] Justin E Stopa, Fabrice Ardhuin, and Fanny Girard-ardhuin. "Wave climate in the Arctic 1992 – 2014 : seasonality and trends." In: (2016), pp. 1605–1629. DOI: 10.5194/tc-10-1605-2016.

[51] Africa I. Flores-Anderson et al. *The SAR Handbook*. 2019. DOI: 10.25966/nr2c-s697. URL: http://www.servirglobal.net.

[52] Johannes Lohse et al. "Mapping sea-ice types from Sentinel-1 considering the surface-type dependent effect of incidence angle." In: *Annals of Glaciology* (2020), pp. 1–11. ISSN: 02603055. DOI: 10.1017/aog.2020.45.

[53] George W Stimson, M Endham, and N E W J Ersey. *Introduction to Airborne Radar*. 1998. ISBN: 1891121014.

[54] F K Li and W T K Johnson. "Ambiguities in Spaceborne Synthetic Aperture Radar Systems." In: 3 (1983), pp. 389–397.

[55] Francesco De Zan and Andrea Monti Guarnieri. "TOPSAR: Terrain Observation by Progressive Scans." In: 44.9 (2006), pp. 2352–2360.

[56] "IEEE Standard Letter Designations for Radar-Frequency Bands." In: *IEEE Std 521-2002 (Revision of IEEE Std 521-1984)* (2003), pp. 1–10. DOI: 10.1109/IEEESTD.2003.94224.

[57] A. John Richards. *Remote Sensing with imaging radar*. Springer, 2009. ISBN: 9783642020193. DOI: 10.1016/0016-7185(70)90029-1.

[58] Fabrizio Argenti et al. "A tutorial on speckle reduction in synthetic aperture radar images." In: *IEEE Geoscience and Remote Sensing Magazine* 1.3 (2013), pp. 6–35. ISSN: 21686831. DOI: 10.1109/MGRS.2013.2277512.

[59] Peter Q. Lee, Linlin Xu, and David A. Clausi. "Sentinel-1 additive noise removal from cross-polarization extra-wide TOPSAR with dynamic least-squares." In: *Remote Sensing of Environment* 248.October 2019 (2020), p. 111982. ISSN: 00344257. DOI: 10.1016/j.rse.2020.111982. URL: https://doi.org/10.1016/j.rse.2020.111982.

[60] Desmond Power et al. "Iceberg detection capabilities of radarsat synthetic aperture radar." In: *Canadian Journal of Remote Sensing* 27.5 (2001), pp. 476–486. ISSN: 17127971. DOI: 10.1080/07038992.2001.10854888.

[61] Jin-woo Kim, Duk-jin Kim, and Seung-hee Kim. "Iceberg Detection using full-polarimetric RADARSAT-2 SAR Data in West Antarctica." In: *2011 3rd International Asia-Pacific Conference on Synthetic Aperture Radar (APSAR)*. IEEE, 2011, pp. 236–239.

[62] Wolfgang Dierking and Christine Wesche. "C-band radar polarimetry - Useful for detection of icebergs in sea ice?" In: *IEEE Transactions on*

Geoscience and Remote Sensing 52.1 (2014), pp. 25–37. ISSN: 01962892. DOI: 10.1109/TGRS.2012.2234756.

[63] Umma H. Himi et al. "Statistical Comparison of Melting Iceberg Backscatter Embedded in Sea Ice and Open Water Using RADARSAT-2 Images of the Newfoundland Sea." In: *IEEE Transactions on Geoscience and Remote Sensing* 60 (2022). ISSN: 15580644. DOI: 10.1109/TGRS.2021.3104626.

[64] Md S. Ferdous et al. "C-Band Simulations of Melting Icebergs Using GRECOSAR and an em Model: Varying Wind Conditions at Lower Beam Mode." In: *IEEE Journal of Selected Topics in Applied Earth Observations and Remote Sensing* 12.12 (2019), pp. 5134–5146. ISSN: 21511535. DOI: 10.1109/JSTARS.2019.2954847.

[65] Johnson Bailey and Armando Marino. "Quad-polarimetric multi-scale analysis of icebergs in ALOS-2 SAR data: A comparison between icebergs in West and East Greenland." In: *Remote Sensing* 12.11 (2020). ISSN: 20724292. DOI: 10.3390/rs12111864.

[66] Wolfgang Dierking. "Sea ice and icebergs." In: *Maritime surveillance with synthetic aperture radar*. Institution of Engineering and Technology, 2020, pp. 173–225.

[67] J. J. Yackel et al. "First-year sea ice spring melt transitions in the Canadian Arctic Archipelago from time-series synthetic aperture radar data, 1992–2002." In: *HYDROLOGICAL PROCESSES* 21 (2007). ISSN: 08856087. DOI: 10.1002/hyp.

[68] J. Alec Casey et al. "Separability of sea ice types from wide swath C- and L-band synthetic aperture radar imagery acquired during the melt season." In: *Remote Sensing of Environment* 174 (2016), pp. 314–328. ISSN: 00344257. DOI: 10.1016/j.rse.2015.12.021. URL: http://dx.doi.org/10.1016/j.rse.2015.12.021.

[69] Wenkai Guo et al. "Cross-platform classification of level and deformed sea ice considering per-class incident angle dependency of backscatter intensity." In: *Cryosphere* 16.1 (2022), pp. 237–257. ISSN: 19940424. DOI: 10.5194/tc-16-237-2022.

[70] Christopher R Jackson and John R Apel. "Synthetic aperture radar: marine user's manual." In: (2004).

[71] Knut Frode Dagestad et al. "WIND RETRIEVAL FROM SYNTHETIC APERTURE RADAR - AN OVERVIEW WIND RETRIEVAL FROM SYNTHETIC APERTURE RADAR – AN OVERVIEW." In: June (2012).

[72] Vahid Akbari and Camilla Brekke. "Iceberg detection in open and ice-infested waters using C-Band polarimetric synthetic aperture radar." In: *IEEE Transactions on Geoscience and Remote Sensing* 56.1 (2018), pp. 407–421. ISSN: 01962892. DOI: 10.1109/TGRS.2017.2748394.

[73] Mauro M. Barbat et al. "An adaptive machine learning approach to improve automatic iceberg detection from SAR images." In: *ISPRS Journal of Photogrammetry and Remote Sensing* 156.March (2019), pp. 247–

259. ISSN: 09242716. DOI: 10.1016/j.isprsjprs.2019.08.015. URL: https://doi.org/10.1016/j.isprsjprs.2019.08.015.

[74] Ben Evans et al. "Unsupervised machine learning detection of iceberg populations within sea ice from dual-polarisation SAR imagery." In: *Remote Sensing of Environment* 297.January (2023), p. 113780. ISSN: 00344257. DOI: 10.1016/j.rse.2023.113780. URL: https://doi.org/10.1016/j.rse.2023.113780.

[75] A. Braakmann-Folgmann et al. "Mapping the extent of giant Antarctic icebergs with deep learning." In: *The Cryosphere* 17.11 (2023), pp. 4675–4690. ISSN: 19940424. DOI: 10.5194/tc-17-4675-2023.

[76] C Oliver and S Quegan. *Understanding synthetic aperture radar images*. Vol. 53. 9. Norwood, MA: Artech House, 1997., 1997, pp. 1689–1699. ISBN: 1891121316.

[77] R. S. Gill. "Operational detection of sea ice edges and icebergs using SAR." In: *Canadian Journal of Remote Sensing* 27.5 (2001), pp. 411–432. ISSN: 17127971. DOI: 10.1080/07038992.2001.10854884.

[78] Anja Frost, Rudolf Ressel, and Susanne Lehner. "Automated Iceberg Detection Using High-Resolution X-Band SAR Images." In: *Canadian Journal of Remote Sensing* 42.4 (2016), pp. 354–366. ISSN: 17127971. DOI: 10.1080/07038992.2016.1177451.

[79] Armando Marino. "Iceberg detection with L-band ALOS-2 data using the Dual-Pol Ratio Anomaly Detector." In: *International Geoscience and Remote Sensing Symposium (IGARSS)* 2018-July.2 (2018), pp. 6067–6070. DOI: 10.1109/IGARSS.2018.8519206.

[80] Johnson Bailey, Armando Marino, and Vahid Akbari. "Comparison of Target Detectors to Identify Icebergs in Quad-Polarimetric L-Band Synthetic Aperture Radar Data." In: *Remote Sensing* 13.1753 (2021).

[81] Armando Marino, Wolfgang Dierking, and Christine Wesche. "A Depolarization Ratio Anomaly Detector to Identify Icebergs in Sea Ice Using Dual-Polarization SAR Images." In: *IEEE Transactions on Geoscience and Remote Sensing* 54.9 (2016), pp. 5602–5615. ISSN: 01962892. DOI: 10.1109/TGRS.2016.2569450.

[82] Igor Zakharov et al. "Improved detection of icebergs in sea ice with RADARSAT-2 polarimetric data." In: *International Geoscience and Remote Sensing Symposium (IGARSS)* 2017-July (2017), pp. 2294–2297. DOI: 10.1109/IGARSS.2017.8127448.

[83] Ingri Halland Soldal et al. "Automatic detection of small icebergs in fast ice using satellite Wide-Swath SAR images." In: *Remote Sensing* 11.7 (2019), pp. 1–24. ISSN: 20724292. DOI: 10.3390/rs11070806.

[84] Kelley Lane et al. "Validation of synthetic aperture radar for iceberg detection in sea ice." In: *International Geoscience and Remote Sensing Symposium (IGARSS)* 1.C (2004), pp. 125–128. DOI: 10.1109/igarss.2004.1368961.

[85] Xinping Deng et al. “Statistical Modeling of Polarimetric SAR Data : A Survey and Challenges.” In: *Remote Sensing* (2017), pp. 1–34. DOI: 10.3390/rs9040348.

[86] D. J. Crisp. *The State-of-the-Art in Ship detection in Synthetic Aperture Radar Imagery*. Tech. rep. DEFENCE SCIENCE and TECHNOLOGY ORGANISATION SALISBURY (AUSTRALIA) INFO SCIENCES LAB, 2004.

[87] J. Buus-Hinkler, Keld Qvistgaard, and Klaus A.Harnvig Krane. “Iceberg number density - Reaching a full picture of the Greenland waters.” In: *International Geoscience and Remote Sensing Symposium (IGARSS)* Dmi (2014), pp. 270–273. DOI: 10.1109/IGARSS.2014.6946409.

[88] Camilla Brekke and Stian N. Anfinsen. “Ship detection in ice-infested waters based on dual-polarization SAR imagery.” In: *IEEE Geoscience and Remote Sensing Letters* 8.3 (2011), pp. 391–395. ISSN: 1545598X. DOI: 10.1109/LGRS.2010.2078796.

[89] Christine Wesche and Wolfgang Dierking. “Iceberg signatures and detection in SAR images in two test regions of the Weddell Sea, Antarctica.” In: *Journal of Glaciology* 58.208 (2012), pp. 325–339. ISSN: 00221430. DOI: 10.3189/2012J0G11J020.

[90] Chen Liu. “Method for Fitting K-Distributed Probability Density Function to Ocean Pixels in Dual-Polarization SAR.” In: *Canadian Journal of Remote Sensing* 44.4 (2018), pp. 299–310. ISSN: 17127971. DOI: 10.1080/07038992.2018.1491789. URL: https://doi.org/10.1080/07038992.2018.1491789.

[91] Khalid El-Darymli et al. “Target detection in synthetic aperture radar imagery: a state-of-the-art survey.” In: *Journal of Applied Remote Sensing* 7.1 (2013), p. 071598. ISSN: 1931-3195. DOI: 10.1117/1.jrs.7.071598.

[92] Chen Liu. *A Dual-Polarization Ship Detection Algorithm*. Tech. rep. November. 2015.

[93] Michael Denbina and Michael J. Collins. “Iceberg detection using compact polarimetric synthetic aperture radar.” In: *Atmosphere - Ocean* 50.4 (2012), pp. 437–446. ISSN: 07055900. DOI: 10.1080/07055900.2012.733307.

[94] Michael Denbina and Michael J. Collins. “Iceberg detection using simulated dual-polarized Radarsat Constellation data.” In: *Canadian Journal of Remote Sensing* 40.3 (2014), pp. 165–178. ISSN: 17127971. DOI: 10.1080/07038992.2014.945517.

[95] Johnson Bailey et al. “Iceberg detection with RADARSAT-2 quad-polarimetric (quad-pol) C-band SAR in Kongsfjorden, Svalbard - comparison with a ground-based radar.” In: *IEEE Journal of Selected Topics in Applied Earth Observations and Remote Sensing* 17 (2024), pp. 5790–5803. ISSN: 21511535. DOI: 10.1109/JSTARS.2024.3369392.

[96] T. Šmejkalová et al. “Iceberg detection capabilities in Sentinel-1 imagery in the Baffin Bay.” In: *European Space Agency, (Special Publication) ESA SP* SP-740.May (2016). ISSN: 03796566.

[97] Tom Fawcett. “An introduction to ROC analysis.” In: 27 (2006), pp. 861–874. DOI: 10.1016/j.patrec.2005.10.010.

[98] James K.E. Tunaley. “K-distribution algorithms.” In: *Automation and Remote Control* 67.8 (2010), pp. 1251–1264. ISSN: 00051179. DOI: 10.1134/S0005117906080054.

[99] R. D. Ketchum and L. D. Farmer. *Eastern Arctic SURSAR SAR ice experiment: Radar signatures of sea ice features*. Tech. rep. NORDA Tech. Note 68, 1980.

[100] A. Laurence Gray and Lyn D. Arsenault. “Time-Delayed Reflections in L-Band Synthetic Aperture Radar Imagery of Icebergs.” In: *IEEE Transactions on Geoscience and Remote Sensing* 29.2 (1991), pp. 284–291. ISSN: 15580644. DOI: 10.1109/36.73670.